# Electronic quantum transport in graphene

Sergey Kopylov

PhD Thesis

Submitted for the degree of Doctor of Philosophy

October 28, 2013

**LANCASTER**
UNIVERSITY

ProQuest Number: 11003434

ProQuest 11003434

# Declaration

This thesis is a result of the author's original work and has not been submitted in whole or in part for the award of a higher degree elsewhere. This thesis documents the work carried out between December 2009 and August 2013 at Lancaster University, UK, under the supervision of Prof. V. I. Fal'ko and V. Cheianov.

The list of author's publications:

1. S. Kopylov, A. Tzalenchuk, S. Kubatkin, V. I. Fal'ko, "Charge transfer between epitaxial graphene and silicon carbide", Appl. Phys. Lett. **97**, 112109 (2010).

2. T. J. B. M. Janssen, A. Tzalenchuk, R. Yakimova, S. Kubatkin, S. Lara-Avila, S. Kopylov, V. I. Fal'ko, "Anomalously strong pinning of the filling factor $\nu = 2$ in epitaxial graphene", Phys. Rev. B **83**, 233402 (2010).

3. S. Kopylov, V. Cheianov, B. L. Altshuler, V. I. Fal'ko, "Transport anomaly at the ordering transition for adatoms on graphene", Phys. Rev. B **83**, 201401 (2011).

4. A. Tzalenchuk, S. Lara-Avila, K. Cedergren, M. Syvajarvi, R. Yakimova, O. Kazakova, T.J.B.M. Janssen, K. Moth-Poulsen, Th. Bjornholm, S. Kopylov, V. I. Fal'ko, S. Kubatkin, "Engineering and metrology of epitaxial graphene", Solid State Comm. **151**, 1094 (2011).

5. S. Kopylov, V. I. Fal'ko, T. Seyller, "Doping of epitaxial graphene on SiC intercalated with hydrogen and its magneto-oscillations", arXiv:1107.4769 (2011).

6. C. J. Chua, M. R. Connolly, A. Lartsev, R. Pearce, S. Kopylov, R. Yakimova, V. I. Falko, S. Kubatkin, T. J. B. M. Janssen, A. Ya. Tzalenchuk, C. G.

Smith, "Effect of local morphology on charge scattering in the quantum Hall regime on silicon carbide epitaxial graphene", in preparation (2013).

Sergey Kopylov

October 28, 2013

# Acknowledgements

# Abstract

Graphene is a new two-dimensional material with interesting electronic properties and a wide range of applications. Graphene epitaxially grown on the Si-terminated surface of SiC is a good candidate to replace semiconductors in field-effect transistors. In this work we investigate the properties of epitaxial monolayer and bilayer graphene and develop a theoretical model used to describe the charge transfer between graphene and donors in SiC substrate. This model is then used to describe the behaviour of an epitaxial graphene-based transistor and the conditions for its operation. We also apply our model to understand the successful application of epitaxial graphene in quantum resistance metrology and to describe the effect of bilayer patches on the resistance quantization. Finally, we study how the ordering of adatoms on top of mechanically exfoliated graphene due to RKKY interaction affects the transport properties of graphene.

# Contents

# List of Figures

10

# Chapter 1

# Introduction

Graphene [1] is a monolayer of carbon atoms arranged in a honeycomb lattice. Even though graphene was theoretically studied many years ago [2], it was thought to be unstable with respect to scrolling and has only been discovered experimentally in 2004 [3]. Since then it became a subject of intensive research with many promising applications. Graphene belongs to the family of carbon materials which were studied in details long before the discovery of graphene and share a number of common properties: graphite (3D), carbon nanotubes (1D), fullerenes (0D) [4].

The nature of many interesting properties of graphene lies in the electronic structure of the low-energy exitations, whose behaviour resembles massless Dirac fermions [3]. This fact presents graphene as a platform for investigating the solid state physics effects in the context of quantum electrodynamics (QED). One of the most interesting effects attributed to Dirac fermions in graphene is the anomalous quantum Hall effect, which reveals an unusual resistance quantization and is robust at room temperatures [5]. The high electron mobility in graphene and the effective control of its doping make graphene a promising material for the manufacturing of field-effect transistors (FET) [6]. It has been demonstrated that graphene-based FET can operate at very high frequencies [7], indicating a potential to replace the semiconductor-based electronics in the future. However, the absence of the spectral gap in graphene and the unimpeded electron transport through potential barriers (Klein tunneling [8]) substantially limit the achievable on-off switching

ratio of transistor [9, 10].

Since the discovery of graphene many methods of its fabrication have been found. Each of them has its own benefits and drawbacks and suits only a specific range of applications. The most commonly used method to produce graphene is the mechanical exfoliation from the bulk graphite [11]. It is based on the use of adhesive tape to separate thin layers of carbon from the graphite crystal. As a result, a lot of thin graphite flakes of different thickness, which are later deposited on a semiconductor substrate, are attached to the tape and some of them have the 1 atom thickness. This method usually produces large samples ($\sim 1$ mm$^2$) of high-mobility graphene, but it is hard to scale the production of such samples.

Another promising approach for graphene manufacturing is the epitaxial growth on silicon carbide. In this method graphene is grown on a SiC surface heated to high temperatures ($> 1000°$C) at low atmosphere pressure [12]. Epitaxial graphene samples often have smaller size ($\sim 100$ $\mu$m$^2$), but the growth process can be well controlled. This method of graphene production is discussed in detail in section 2.1.

In this thesis we will investigate these two types of graphene. Even though the environment around graphene depends on its method of fabrication, the band structure of graphene depends only on a few external parameters and can be studied independently of the type of graphene. In the following sections we investigate the band structure of monolayer and bilayer graphene.

## 1.1    Band structure of monolayer graphene

Monolayer graphene is a single layer of carbon atoms arranged in a honeycomb lattice, shown in Fig. 1.1. The crystal structure of graphene consists of two identical Bravais lattices (A and B) shifted relative to each other. The translational properties of the lattice are defined by the lattice vectors

$$\mathbf{a}_1 = \frac{a}{2}(3, \sqrt{3}), \quad \mathbf{a}_2 = \frac{a}{2}(3, -\sqrt{3}), \tag{1.1}$$

where $a = 1.42\mathring{A}$ is the distance between carbon atoms. The reciprocal lattice vectors are

$$\mathbf{b}_1 = \frac{2\pi}{3a}(1, \sqrt{3}), \quad \mathbf{b}_2 = \frac{2\pi}{3a}(1, -\sqrt{3}). \tag{1.2}$$

The Brillouin zone has the form of the hexagon the six corners of which are projected on the two inequivalent points $K$ and $K'$.
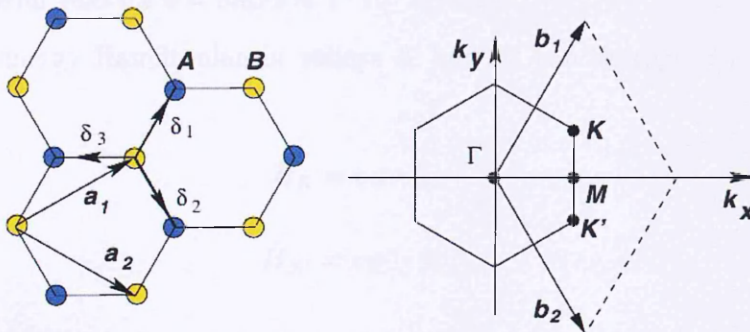


Figure 1.1: Graphene honeycomb lattice and Brillouin zone. Adapted from [13].

We describe the band structure of graphene within the tight-binding approximation, that describes the formation of a $\pi$-band due to covalent bonding between the $p$ orbitals of the neighboring carbon atoms, which are perpendicular to the graphene plane. The Hamiltonian of electrons in graphene can be written as

$$\hat{H} = -t \sum_{\langle i,j \rangle} (\hat{a}_i^\dagger \hat{b}_j + \hat{b}_j^\dagger \hat{a}_i), \tag{1.3}$$

where $t = 2.8$ eV is the nearest-neighbor hopping energy, $\hat{a}_i$, $\hat{b}_j$ ($\hat{a}_i^\dagger$, $\hat{b}_j^\dagger$) are electron annihilation (creation) operators on carbon atoms $i$, $j$ of A and B sublattices correspondingly. The sum in Eq. (1.3) is taken over the pairs of nearest neighbors $i$ and $j$. The spectrum of the Hamiltonian (1.3), shown in Fig. 1.2, can be written as

$$\epsilon(\mathbf{k}) = \pm t \sqrt{3 + 2\cos\sqrt{3}k_y a + 4\cos\left(\frac{\sqrt{3}}{2}k_y a\right)\cos\left(\frac{3}{2}k_x a\right)}. \tag{1.4}$$

The touching points of upper and lower bands, corresponding to the energy $E = 0$, are called Dirac points.

14

In practical applications we are often interested in the low-energy spectrum of graphene ($\epsilon \lesssim 0.4$ eV). Thus the dispersion Eq. (1.4) can be linearized in the vicinities of $K$ and $K'$ points called valleys:

$$\epsilon(\mathbf{p}) = \pm v|\mathbf{p}|, \quad \mathbf{k} = \mathbf{K}(\mathbf{K}') + \mathbf{p}, |\mathbf{p}| \ll |\mathbf{K}|, \tag{1.5}$$

where the Fermi velocity $v = 3ta/2 \approx 1 \cdot 10^6$ m/s [2].

The low-energy Hamiltonian in valleys $K$ and $K'$ can be represented in the form [14]

$$\hat{H}_K = v\boldsymbol{\sigma} \cdot \hat{\mathbf{p}}, \tag{1.6}$$

$$\hat{H}_{K'} = v\boldsymbol{\sigma}^* \cdot \hat{\mathbf{p}}, \tag{1.7}$$

where $\hat{\mathbf{p}} = -i\hbar\nabla$ is the momentum operator, $\boldsymbol{\sigma} = (\sigma_x, \sigma_y)$ and $\boldsymbol{\sigma}^* = (\sigma_x, -\sigma_y)$ are Pauli matrices in the sublattice space. These equations define the Dirac nature of the quasiparticles in graphene.

The wavefunctions corresponding to momentum $\mathbf{p}$ in each valley are

$$\psi_{\pm,K,\mathbf{p}} = \frac{e^{i\mathbf{p}\mathbf{r}/\hbar}}{\sqrt{2S}}\begin{pmatrix} e^{-i\varphi_{\mathbf{p}}/2} \\ \pm e^{i\varphi_{\mathbf{p}}/2} \end{pmatrix}, \quad \psi_{\pm,K',\mathbf{p}} = \frac{e^{i\mathbf{p}\mathbf{r}/\hbar}}{\sqrt{2S}}\begin{pmatrix} e^{i\varphi_{\mathbf{p}}/2} \\ \pm e^{-i\varphi_{\mathbf{p}}/2} \end{pmatrix}, \tag{1.8}$$

where $S$ is the area of the graphene sheet, $\pm$ corresponds to the upper and lower bands, and $\mathbf{p} = (p\cos\varphi_{\mathbf{p}}, p\sin\varphi_{\mathbf{p}})$.

The electron density in monolayer graphene has a quadratic dependence on the Fermi momentum (taking into account the valley and spin degeneracy)

$$n = \frac{p_F^2}{\pi\hbar^2}. \tag{1.9}$$
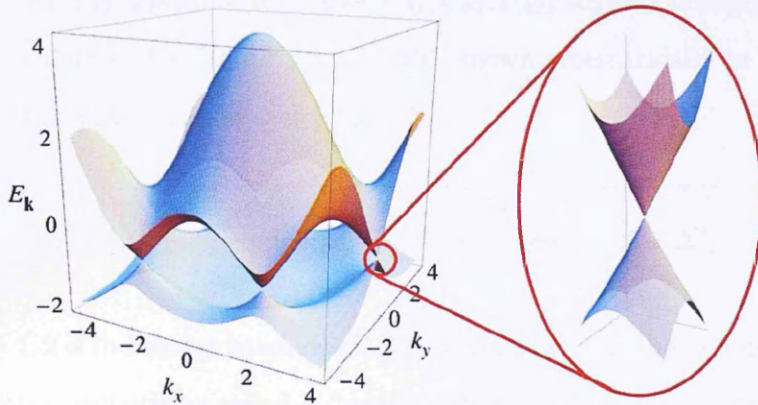
Figure 1.2: Electronic dispersion of monolayer graphene. Right: zoom in of the energy bands close to one of the Dirac points. Adapted from [13].

## 1.2 Band structure of bilayer graphene

Bilayer graphene (BLG) consists of two coupled honeycomb lattices, arranged according to Bernal stacking, which is illustrated in Fig. 1.3(a). The two layers are shifted along the A1-B1 direction, so that A2 sites are always located above B1 sites. The band structure of BLG can be described using the tight-binding model [15]. The main contributions to it are coming from the in-plane coupling, characterized by the velocity $v$ and the inter-layer coupling $\epsilon_1 = 0.39$ eV between A2 and B1 sites. Here we neglect the effect of trigonal warping produced by a weaker A1-B2 coupling [16]. Thus the low-energy Hamiltonian of BLG in the vicinity of $K$ and $K'$ points can be represented as

$$
\hat{H} = \xi \begin{pmatrix} -\Delta/2 & 0 & 0 & v\pi^\dagger \\ 0 & \Delta/2 & v\pi & 0 \\ 0 & v\pi^\dagger & \Delta/2 & \xi\epsilon_1 \\ v\pi & 0 & \xi\epsilon_1 & -\Delta/2 \end{pmatrix},
\tag{1.10}
$$

where $\pi = p_x + ip_y$, $\pi^\dagger = p_x - ip_y$, $\xi = +1$ $(-1)$ specifies the valley $K$ $(K')$, $\Delta$ is the difference between on-site energies in the layers due to an external perpendicular electric field. The wave function bases in $K$ and $K'$ valleys are

$\psi = (\psi_{A1}, \psi_{B2}, \psi_{A2}, \psi_{B1})$ and $\psi = (\psi_{B2}, \psi_{A1}, \psi_{B1}, \psi_{A2})$ correspondingly.

The spectrum of the Hamiltonian (1.10), shown schematically in Fig. 1.3(b), consists of 4 energy bands in each valley [15]

$$\epsilon^{(\beta)}(p) = \pm\sqrt{\frac{\epsilon_1^2}{2} + \frac{\Delta^2}{4} + v^2 p^2 + (-1)^\beta \sqrt{\frac{\epsilon_1^4}{4} + v^2 p^2 (\epsilon_1^2 + \Delta^2)}}, \qquad (1.11)$$

where $\beta = 1, 2$ is the energy band index. The low-energy band has a non-monotonic form, which is sometimes called a "mexican hat". The bottom of this band is achieved at a non-zero value of momentum $p$, however we will approximate the bottom part by the value $\epsilon^{(1)}(0) = \pm\Delta/2$. Thus, the difference between on-site energies in the layers $\Delta$ also happens to be the spectral gap. The bottom of the high-energy band corresponds to a much higher energy $\sqrt{\epsilon_1^2 + \Delta^2/4}$.

In the absence of an external electric field the spectral gap of BLG $\Delta = 0$ and the spectrum of bilayer graphene in the vicinity of the Brillouin zone corners is [16]

$$\epsilon^{(\beta)}(p) = \pm\left(\sqrt{\frac{\epsilon_1^2}{4} + v^2 p^2} + (-1)^\beta \frac{\epsilon_1}{2}\right). \qquad (1.12)$$

This limit applies to exfoliated bilayer graphene with no electric gates.

The spectral gap $\Delta$ can be represented as the electrostatic energy difference between the layers. In the presence of an external gate with carrier density $n_g$ on the top of graphene

$$\Delta = -\frac{e^2 c_0}{\varepsilon_0 \varepsilon_r}(n_1 + n_g), \qquad (1.13)$$

where $c_0 = 0.3$ nm is the distance between graphene layers and $n_1$ is the electron density of the top graphene layer. The dielectric constant of BLG is not known but it is supposed to be in the range between 1 and 2.4 (the value for bulk graphite) [15]. As an approximation for the unknown value of the dielectric constant we use $\varepsilon_r = 1.5$, which doesn't affect any qualitative results of this thesis.

Due to the external electric field the electron density $n$ of BLG is distributed
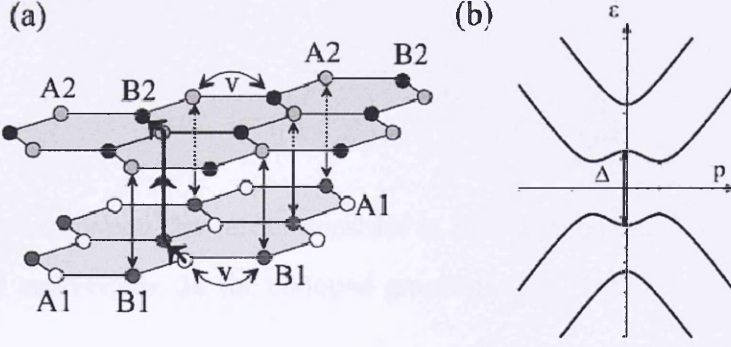
Figure 1.3: The crystal lattice (a) and electron spectrum (b) of bilayer graphene. Adapted from [15, 17].

asymmetrically between the top ($n_1$) and bottom ($n_2$) layers ($n = n_1 + n_2$)

$$n_\alpha = \sum_\beta [f_{\alpha,\beta}(\epsilon_F, \Delta) + f_{\alpha+1,\beta}(\infty, \Delta) - f_{\alpha+1,\beta}(\infty, 0)], \qquad (1.14)$$

where $\alpha = 1, 2$ is the layer index,

$$f_{\alpha,\beta}(\epsilon, \Delta) = \int_0^{p_\beta(\epsilon,\Delta)} p\,dp\, \frac{\epsilon^{(\beta)} + (-1)^\alpha \frac{\Delta}{2}}{\pi\hbar^2\epsilon^{(\beta)}} \frac{(\epsilon^{(\beta)2} - \frac{\Delta^2}{4})^2 + (-1)^\alpha v^2 p^2 \epsilon^{(\beta)}\Delta - v^4 p^4}{(\epsilon^{(\beta)2} - \frac{\Delta^2}{4})^2 + v^2 p^2 \Delta^2 - v^4 p^4}$$

$$(1.15)$$

is the contribution of the energy band $\beta$ to the electron density, and $p_\beta(\epsilon, \Delta)$ is the momentum corresponding to the energy $\epsilon$ in the band with index $\beta$ or 0 for energies within the spectral gap.

At small carrier densities, when the Fermi level is far from the bottom of the high-energy band ($\Delta \ll \epsilon_1$, $n \ll \epsilon_1^2/2\pi\hbar^2 v^2 \approx 5.6 \cdot 10^{12}$ cm$^{-2}$), it is possible to neglect the effect of the high-energy band and use the approximated 2-band model [16] with a simpler Hamiltonian

$$\hat{H}_{2-band} = -\frac{1}{2m} \begin{pmatrix} 0 & (\pi^\dagger)^2 \\ \pi^2 & 0 \end{pmatrix} - \frac{\xi\Delta}{2} \begin{pmatrix} 1 & 0 \\ 0 & -1 \end{pmatrix}, \qquad (1.16)$$

and the spectrum

$$\epsilon(p) = \pm\sqrt{\left(\frac{p^2}{2m}\right)^2 + \frac{\Delta^2}{4}}; \quad m = \frac{\epsilon_1}{2v^2}. \tag{1.17}$$

In this approximation the carrier densities in BLG layers (Eq. (1.14, 1.15)) can be calculated analytically. In the undoped graphene ($|\epsilon_F| \leq |\Delta|/2$)

$$n_\alpha = -\frac{(-1)^\alpha m\Delta}{4\pi\hbar^2}\ln\left(\frac{2\epsilon_1}{|\Delta|}\right), \tag{1.18}$$

whereas, for $|\epsilon_F| > |\Delta|/2$,

$$n_\alpha = \frac{\text{sgn}(\epsilon_F)p_F^2}{4\pi\hbar^2} - \frac{(-1)^\alpha m\Delta}{4\pi\hbar^2}\ln\left(\frac{\epsilon_1}{|\epsilon_F| + \frac{p_F^2}{2m}}\right). \tag{1.19}$$

The results presented here will be applied in the problems investigated in the next chapters.

# Chapter 2

# Electronic properties of epitaxial graphene on Si-terminated surface of SiC

Among the several ways of fabricating graphene [18, 19, 20], one of the promising methods for the top-down manufacturing of electronic devices consists in the graphitization of Si-terminated surface of silicon carbide. It has been found that the epitaxial graphene grown onto cm-size wafers of the Si-terminated face of SiC [6, 21, 22, 23, 24, 25, 26, 27] maintains structural integrity over a large area and demonstrates a relatively high mobility of carriers [7, 28, 29]. This makes graphene synthesized on SiC (G/SiC) a promising platform to build integrated electronic circuits, assuming one can control the carrier density in it. For transistor applications, bilayer graphene in G/SiC is a particularly interesting material, since interlayer asymmetry (e.g., induced by a transverse electric field) opens a minigap in its spectrum [16, 30, 31, 32, 33].

At the same time, the structure of SiC surface is modified during the epitaxial growth which results in a high electron density $\sim 1 \cdot 10^{13}$ cm$^{-2}$ in graphene. This fact makes it harder to utilize G/SiC in electronic devices such as field-effect transistors (FET). To understand such systems we developed a theoretical model

describing the electrostatic and transport properties of G/SiC in different environments.

In this chapter we describe the electronic properties of epitaxial monolayer and bilayer graphene in zero magnetic field. Section 2.1 explains the reconstruction of the SiC surface due to graphitization, which results in the formation of epitaxial graphene. We also discuss the effect of hydrogen intercalation and spontaneous polarization of SiC on graphene structures. In section 2.2 we present the theory of the charge transfer between donors in SiC and the monolayer graphene (MLG) and apply this theory to calculate the doping of graphene. We also discuss whether G/SiC can be used as a basis for the fabrication of field-effect transistors. Then we apply our quantitative model to describe the electronic effects of SiC ferroelectricity and hydrogen intercalation. In section 2.3 we apply the charge transfer theory to epitaxial bilayer graphene (BLG/SiC) and use it to calculate the modification of the band structure. The special gap opened due to the charge transfer makes it possible to observe the carrier density pinch-off effect in BLG/SiC and the variable-range hopping (VRH) transport regime. Finally, we perform the similar calculations for quasi-free standing bilayer graphene.

## 2.1  Electronic structure of SiC surface

### 2.1.1  Buffer layer

Epitaxial growth of graphene is based on the graphitization of SiC surface at high temperatures $> 1000°C$. A number of variants of this method performed in different environments produce graphene samples of various thickness and quality. One of the most important factors for graphene growth is the crystallographic direction of SiC surface – SiC(0001) (Si-face) or SiC(000$\bar{1}$) (C-face). It appears to be much harder to control the number of graphene layers during the growth on the C-face [34]. The reaction kinetics on the Si-face is slower than on the C-face because of the higher surface energy, which helps homogeneous and well-controlled graphene

formation [21, 23] and explains the wide use of this method in manufacturing electronic devices. In this thesis we study the properties of graphene grown on the Si-terminated face of SiC. Below we describe the structure of the SiC surface and how it affects the electronic properties of graphene grown on top of it.

Fig. 2.1(a) shows the structural model of epitaxial monolayer graphene. During the epitaxial growth the surface of SiC(0001) undergoes transitions between different structural phase states. The annealing of the surface leads to the formation of a $(\sqrt{3} \times \sqrt{3})R30°$ phase at 950°C and a well ordered $(6\sqrt{3} \times 6\sqrt{3})R30°$ phase at 1100°C. The carbon layer partially connected with the top Si layer is called 'dead layer' or 'buffer layer'. Even though it has a graphene-like crystal structure - $(6\sqrt{3} \times 6\sqrt{3})R30°$ superlattice illustrated in Fig. 2.1(b), this structure leads to heavily suppressed electron transport properties of this layer, which cannot be considered as graphene. The unit cell of the superlattice contains 108 Si and 108 C atoms per SiC bilayer and covers 338 atoms in graphene layer. This structure was detected by a number of experimental methods including low energy electron diffraction (LEED) [35, 36] and STM measurements under certain tip conditions [36]. The subsequent layers grown on top of the buffer layer reveal many properties of graphene, though they are still affected by $(6\sqrt{3} \times 6\sqrt{3})R30°$ reconstruction.
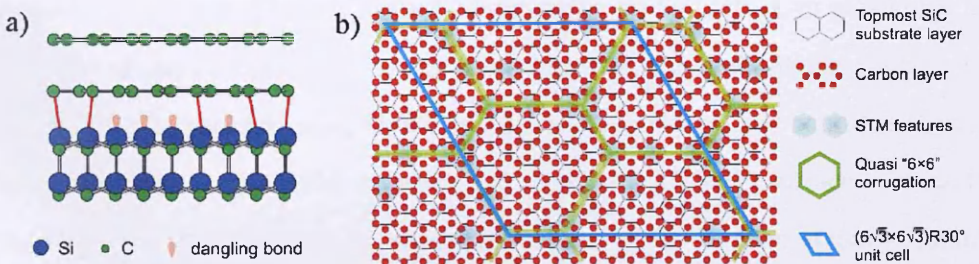


Figure 2.1: a) Structural model of MLG/SiC grown on the Si-face of SiC. b) Structural model of $(6\sqrt{3} \times 6\sqrt{3})R30°$ reconstruction in top view, showing the relation between lattice structures of Si-C bilayers, buffer layer and graphene. Adapted from [12].

The reconstruction of the SiC(0001) surface during the growth results in a break of Si-C bonds between buffer layer and Si atoms in the surface. The spectral

analysis of the bonds in the buffer layer [12] revealed that almost 1/3 of these Si-C bonds survive the reconstruction. Angle-resolved photoemission spectroscopy (ARPES) measurements [37] confirm that the buffer layer has no linear spectrum near $K$ points. Substituted carbon atoms and bonds with the SiC substrate in various positions of a big supercell in the buffer layer create localized surface states with a broad distribution of energies within the bandgap of SiC ($\approx 2.4$ eV) [36, 38, 39, 40, 41, 42].

Without special growth protocols, these surface donors lead to a large electron density in graphene. MLG/SiC grown at low temperatures ($1200 - 1600$ °C) appears to be doped to $n \sim 10^{13}$ cm$^{-2}$ [43, 44], which is difficult to change [45]. Also, charged surface donors induce Coulomb scattering, which limits the mobility of electrons in such a material. On the other hand, graphene growth at higher temperatures, $T \approx 2000$ °C, and in a highly pressurised atmosphere of Ar seems to improve the integrity of the reconstructed buffer layer, leading to a lower density of donors on the surface and, therefore, a much lower initial doping of graphene [28, 46].

## 2.1.2 Hydrogen intercalation

Despite the benefits of graphene epitaxially grown on SiC(0001), in particular, the large size of samples and the control of its thickness, the high intrinsic doping can become an obstacle for using G/SiC in electronic devices. The coupling between 30% of C atoms in the buffer layer with Si atoms of SiC(0001) surface leads to the $(6\sqrt{3} \times 6\sqrt{3})R30°$ reconstruction of the surface, which in turn strongly reduces graphene mobility compared to exfoliated graphene. One of the most effective ways to break the residual Si-C bonds of the buffer layer and improve the transport characteristics of G/SiC is hydrogen intercalation [37]. Hydrogenation eliminates occasional coupling between carbon and Si atoms in the buffer layer turning the buffer layer into a quasi-free standing monolayer graphene (QFMLG), which is usually positively doped [12, 47] due to electron transfer from graphene to acceptor

states in the H-terminated surface of SiC (Fig. 2.2). Hydrogen intercalation applied to MLG/SiC produces quasi-free standing bilayer graphene (QFBLG), which is usually highly p-doped ($n_h^{(0)} \sim 10^{13}$ cm$^{-2}$) [37, 48, 49].
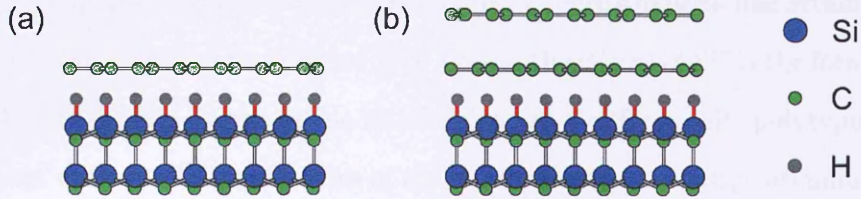


Figure 2.2: The saturation of Si bonds by hydrogen after hydrogen intercalation of (a) the $(6\sqrt{3} \times 6\sqrt{3})R30°$ reconstructed buffer layer (QFMLG) and (b) an epitaxial monolayer graphene (QFBLG). Adapted from [12].

The mechanism of hydrogen intercalation described above was confirmed by a number of experimental studies. Low energy electron diffraction (LEED) images demonstrate the suppression of the $(6\sqrt{3} \times 6\sqrt{3})R30°$ superlattice structure signal and the amplification of the graphene diffraction pattern after hydrogen intercalation is performed [12]. Another confirmation comes from ARPES measurements that reveal the recovery of the linear dispersing $\pi$-bands in the buffer layer after intercalation [37]. This process appears to be completely reversible as Si-H bonds break at temperatures between 700-900°C.

### 2.1.3    Spontaneous electrical polarization of silicon carbide

The crystal structure of SiC represents a stack of Si-C bilayers placed on top of each other according to a specific pattern. These patterns that differ by orientation and shift of the layers are called polytypes. The most commonly used polytypes are cubic (3C) and hexagonal (2H, 4H, 6H) [50], some of which are shown in Fig. 2.3. As a result of different stacking of bilayers many properties of SiC depend on the polytype, e.g., band gap, dielectric constant and spontaneous electrical polarization.

Spontaneous polarization (SP) of SiC is a bulk effect resulting from a charge polarization within the unit cell and a particular symmetry of the crystal lattice.

In 3C polytype the SP is not observed, while it has different non-zero values in hexagonal polytypes. The SP is hard to determine both theoretically and experimentally. Its absolute value cannot be measured directly and only the modulation of the spontaneous polarization due to external perturbations like strain or temperature variation can be detected [51]. One of the effects of SP is the formation of an effective surface charge at the interface between different SiC polytypes, where different values of SP on two sides of the interface lead to a charge accumulation in a two dimensional electron gas (2DEG) [52]. This property was used in a number of theoretical methods to calculate the SP in SiC [51, 53, 54, 55]. Its value $P_0$ depends on the polytype and is in the range of $(1 - 5) \cdot 10^{-2}$ C/m$^2$.
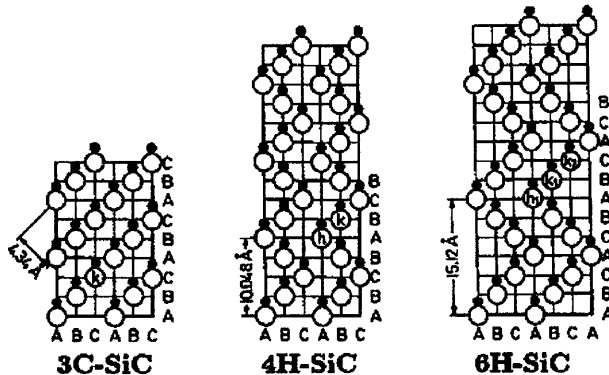


Figure 2.3: Stacking of Si-C bilayers in different polytypes of SiC. Open and closed circles denote Si and C atoms respectively. Adapted from [50].

To understand the effect of the SP on the electric properties of SiC let's consider a flat SiC sample (Fig. 2.4). Since this system has no surfaces with a finite surface change density, the electric displacement field $\mathbf{D} = \varepsilon_0 \mathbf{E} + \mathbf{P}_0$ equals 0 in the bulk of SiC. As a result the electric field $\mathbf{E} = -\mathbf{P}_0/\varepsilon_0$ appears and redistributes the charge of donors in the bulk towards the surfaces. Thus, a depletion layer of donors is formed near the Si-terminated surface. The capacitor formed by the two charged layers near the SiC surfaces charges until it compensates the electric field due to the SP, so that the electric field in the bulk of SiC is 0. The hole density of the depletion layer near the Si-terminated surface is $n_p = P_0/e$. This result is used later in this chapter to understand the effect of the SP on the carrier density in

G/SiC.
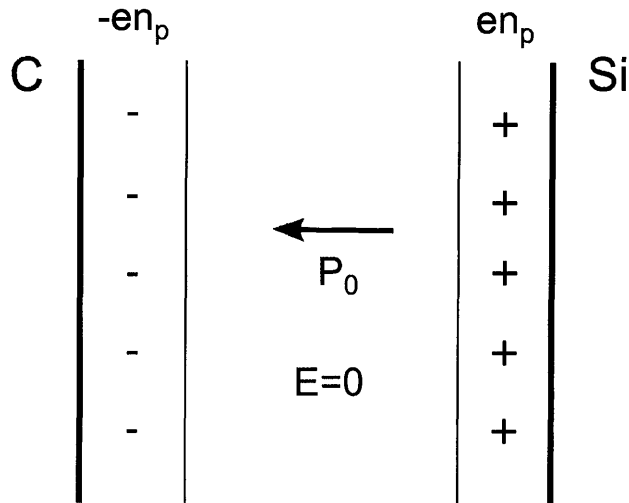


Figure 2.4: The redistribution of the charge in SiC due to the spontaneous polarization.

### 2.1.4 Field-effect transistor based on epitaxial graphene

In recent years fundamental graphene studies turned towards practical implementation of this atomically thin material in electronics. Such studies are, partially, focused on the development of field-effect transistors based on epitaxial graphene [6, 27, 29, 56], which seems to be one of the possible ways to develop a top-down technology of scalable graphene-based wafer-scale circuitry. The effective operation of transistors based on G/SiC requires control of conductivity through the variation of the carrier density in graphene, which is governed by charge transfer between epitaxial graphene and donors in SiC [45].

Methods for precise control of the carrier density in electronic materials are the cornerstones of the modern semiconductor technology. Chemical methods ranging from direct doping to modulation doping have been developed to absolute perfection for semiconductors over the last half-century. Graphene can also be effectively doped for example by adsorption of gas molecules [57]. In addition to permanent doping, the electronic properties of semiconductor materials and graphene can be changed by the electric field produced by a charged gate, as in

26

a transistor, but this requires an external voltage source permanently connected to maintain the stored charge. Semiconductor programmable nonvolatile memory devices give us an inspirational example of how the carrier density of materials can be changed, latched and then erased. These devices are essentially transistors with one extra floating, isolated gate sandwiched between the control gate and the semiconductor channel. Charge can be transferred to the floating gate by an electric pulse on the control gate and stored there isolated almost indefinitely, until intentionally leaked through the dielectric, e.g. activated by UV light. In other implementations of nonvolatile memory devices UV light is used for writing [46] in which case thermal activation can be used for erasing.
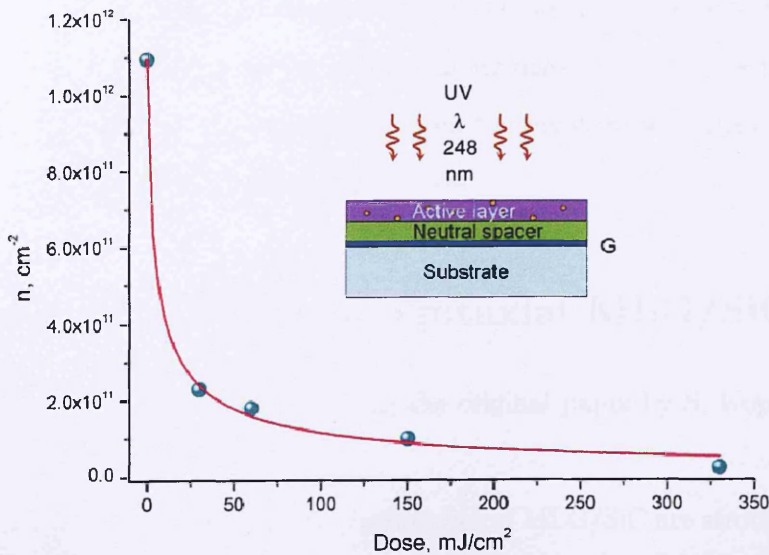


Figure 2.5: Photochemical gating of graphene. Adapted from [58].

Though, unsurprisingly, the relatively low density in the epitaxial graphene grown with the technology [24] briefly summarised above could be further reduced by applying a voltage between a metallic gate and graphene across a PMMA/MMA copolymer spacer, methods of non-invasive, nonvolatile and reversible charge carrier control would be particularly important for the engineering of devices for metrology, where it is preferable to avoid an additional electrically controlled parameter, which brings additional noise.

To achieve the nonvolatile control of the carrier density the metal gate can be replaced by a polymer layer with the ability to provide potent acceptors under deep UV light. The photochemical gating of graphene was demonstrated in [46] using ZEP520A polymer. In a sample with the initial carrier density $n \approx 1.1 \cdot 10^{12}$ cm$^2$, subsequent exposures to UV at 248 nm wavelength up to the dose of 330 mJ/cm$^2$ decreased the low-temperature electron density 50 times down to $2 \cdot 10^{10}$ cm$^2$ (Fig. 2.5). The irradiated devices remained latched in their high-resistivity state over many months. The on/off ratio of 10 for the resistivity in the photochemically-gated devices is similar to the best large-area single-layer graphene transistors demonstrated to date [59]. Very significantly, annealing the samples at 170°C – just above the glass transition temperature of the polymers – reversed the effects of light and returned the graphene charge carrier density to its value prior to UV exposure. The behaviour measured at room temperature was qualitatively the same as the one observed at low temperatures.

## 2.2 Charge transfer in epitaxial MLG/SiC

The material in this section is based on the original paper by S. Kopylov, *et al.* [45].

As discussed above, the electronic properties of MLG/SiC are strongly affected by the proximity of the underlying buffer layer. The local defects in the buffer layer created by unsaturated Si bonds serve as electron donors for graphene. Combined with donors from the bulk of SiC they result in high n-doping of graphene $n \sim 10^{13}$ cm$^{-2}$. The high carrier density and a low responsivity to gate voltage creates an obstacle for using G/SiC in transistors and other electronic devices [27, 43, 44, 60]. This underlines the importance of investigating the transfer of charge from surface and bulk donor states in SiC to graphene. In this section we develop a theoretical model which describes the charge transfer in field-effect transistors (FET) based on both MLG/SiC and quasi-free standing MLG (QFMLG).

The schematic structure of a FET device is shown in Fig. 2.6(a). The distance

between graphene and the SiC surface is $d \approx 0.2$ nm. Our model takes into account the two types of donors in SiC, which donate electrons to graphene in order to achieve electrostatic balance:

a) surface donors with surface density of states $\gamma$. These donors originate during graphitization process, where the surface of SiC undergoes $(6\sqrt{3}{\times}6\sqrt{3})R30°$ reconstruction and creates unsaturated Si bonds.

b) bulk donors with density $\rho$ that are characterized by $\tilde{A}$ - the work function between graphene and distant bulk donors.

Fig. 2.6(b) shows the energy diagram of G/SiC. The saturation layer of thickness $l$ near the surface of SiC with the homogeneous donor density $\rho$ creates the parabolic energy profile in the bulk of SiC. The electric field between the SiC surface and the graphene layer results in a shift of the Dirac point $e^2 d(n+n_g)/\varepsilon_0$.

The charge balance in this top-gated field-effect transistor is described by a system of two coupled equations:

$$\gamma \left[ A - \frac{e^2 d(n+n_g)}{\varepsilon_0} - \epsilon_F \right] + \rho l = n + n_g, \qquad (2.1)$$

$$\tilde{A} = \epsilon_F + U + \frac{e^2 d(n+n_g)}{\varepsilon_0}. \qquad (2.2)$$

Equation (2.1) states the charge conservation in the system, with $n_g = CV_g/e$ ($e > 0$) being the areal density of electrons transferred to the gate. Here, $\tilde{A}$ ($A$) is the difference between the work function of graphene and the work function of electrons in the bulk (surface) donors in SiC, and $\epsilon_F$ is the Fermi energy in doped graphene relative to the Dirac point. Eq. (2.2) describes the equilibrium between electrons in graphene and bulk donors, with $l$ standing for the depletion layer width in SiC, $U = e^2 \rho l^2/(2\chi\varepsilon_0)$ being the height of the Schottky barrier ($\chi$ is the dielectric constant of SiC), and $d$ - the distance between the SiC surface and graphene layer.
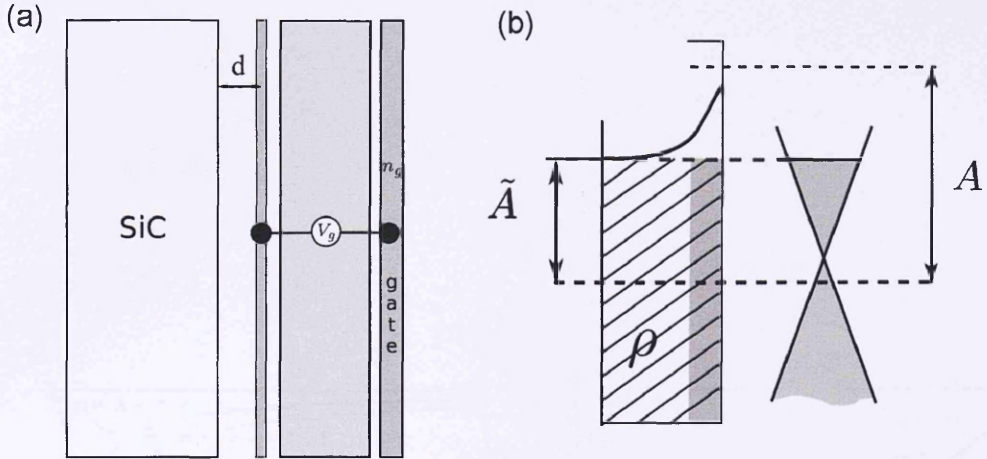
Figure 2.6: a) The structure of a G/SiC-based field-effect transistor. b) The band structure of G/SiC. The striped area shows the depletion layer of bulk donor states in SiC. The shaded bar under the surface of SiC shows the occupied surface donor states.

## 2.2.1 The role of quantum capacitance of G/SiC surface in graphene doping

In the following, we calculate the density $n$ of electrons in two limits: graphene doping dominated by the charge transfer from

(a) surface donors, which corresponds to solving Eq. (2.1) with $\rho l \longrightarrow 0$;

(b) bulk donors (e.g. nitrogen), which corresponds to solving Eqs. (2.1, 2.2) with $\gamma = 0$.

Charge transfer in a more generic situation, with arbitrary $\rho$ and $\gamma$, can be assessed by taking the largest of the two estimates.

Monolayer graphene has the linear spectrum $\epsilon_{\pm}(p) = \pm vp$, in the two valleys, corresponding to the non-equivalent corners $K$ and $K'$ of the hexagonal Brillouin zone, so that $\epsilon_F(n) = \mathrm{sng}(n)\hbar v\sqrt{\pi|n|}$ (we take into account both valley and spin degeneracy of the electron states).

In the limit (a) $\rho l \longrightarrow 0$ we find that the carrier density is

$$
n = \frac{A\gamma^2 \left[ \sqrt{1 + \frac{\gamma_A}{\gamma^2}\left(\gamma - \frac{n_g}{A}\frac{\gamma_d + \gamma}{\gamma_d}\right)\frac{\gamma_d + \gamma}{\gamma_d}} - 1 \right]^2}{\gamma_A \left(1 + \frac{\gamma}{\gamma_d}\right)^2}, \tag{2.3}
$$

30
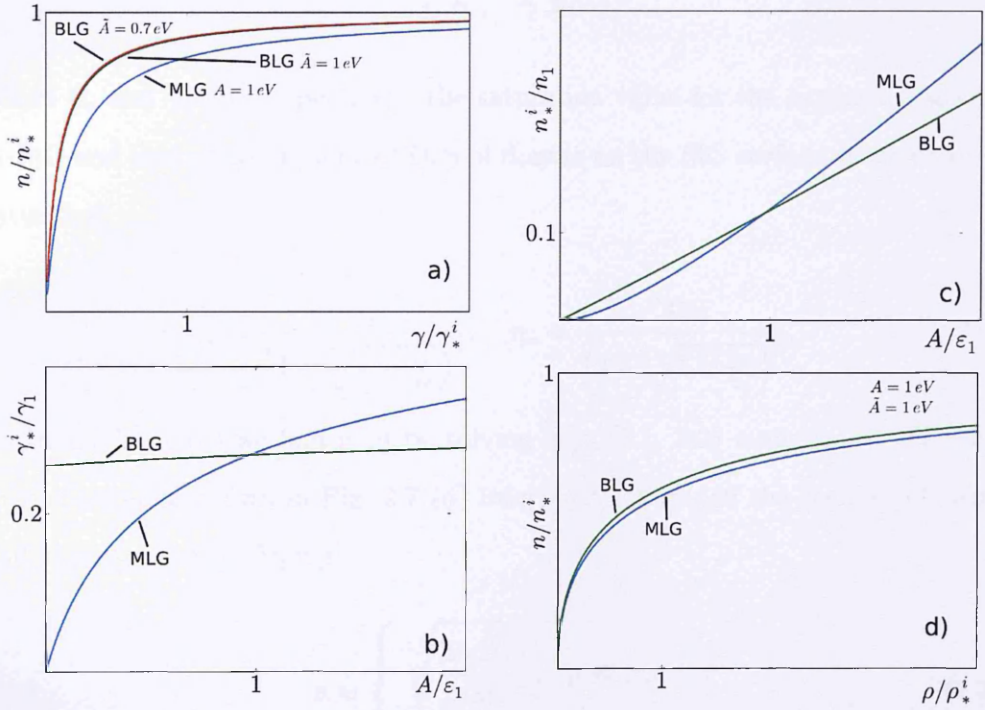
Figure 2.7: Comparison between charge transfer from SiC to MLG and BLG, with $A$ measured in units of split-band energy in BLG, $\epsilon_1 = 0.4\,\text{eV}$, $d = 0.3\,\text{nm}$ for MLG and $d = 0.5\,\text{nm}$ for BLG. (a) Electron concentration in graphene $n$ dominated by charge transfer from surface states. (b) Values $\gamma_*$ of the surface DoS at which $n(\gamma)$ saturates ($\gamma_1 = \epsilon_1/\pi\hbar^2 v^2$). (c) Saturation density value as a function of $n_*$, in units of $n_1$. (d) Electron bulk donors density $\rho$ for $\gamma = 0$.

$$\gamma_d = \frac{\varepsilon_0}{de^2}, \qquad \gamma_A = \frac{4A}{\pi\hbar^2 v^2}. \tag{2.4}$$

The initial density of electrons in graphene is described by Eq. (2.3) ($n_g = 0$) with two characteristic regimes,

$$n \approx \begin{cases} A\gamma, & \gamma \ll \gamma_*; \\ n_*, & \gamma \gg \gamma_*, \end{cases} \tag{2.5}$$

where $n_*$ and $\gamma_*$ are, respectively, the saturation value for the carrier density in G/SiC and the crossover value of DoS of donors on the SiC surface at which $n(\gamma)$ saturates:

$$\gamma_* = \frac{\gamma_A}{\left(1 + \sqrt{1 + \frac{\gamma_A}{\gamma_d}}\right)^2}, \quad n_* = \frac{A\gamma_A}{\left(1 + \sqrt{1 + \frac{\gamma_A}{\gamma_d}}\right)^2}. \tag{2.6}$$

In the limit (b) we find $n(\rho)$ by solving Eqs. (2.1, 2.2) numerically. The numerical solution shown in Fig. 2.7 (d) interpolates between the regimes of weak and strong graphene doping:

$$n \approx \begin{cases} \sqrt{\dfrac{2\varepsilon_0 \tilde{A}\chi\rho}{e^2}}, & \rho \ll \rho_*; \\ \tilde{n}_*, & \rho \gg \rho_*; \end{cases} \tag{2.7}$$

$$\tilde{n}_* = \frac{\tilde{A}\tilde{\gamma}_A}{\left(1 + \sqrt{1 + \frac{\tilde{\gamma}_A}{\gamma_d}}\right)^2}, \quad \rho_* = \frac{e^2 \tilde{A}\tilde{\gamma}_A^2}{2\varepsilon_0\chi \left(1 + \sqrt{1 + \frac{\tilde{\gamma}_A}{\gamma_d}}\right)^4}, \tag{2.8}$$

where

$$\tilde{\gamma}_A = \frac{4\tilde{A}}{\pi\hbar^2 v^2}. \tag{2.9}$$

Independent of the number of layers, the gate voltage $V_g^*$ needed to reach the neutrality point in graphene controlled by the top gate with mutual capacitance

$C$ is

$$V_g^* \approx \frac{e}{C} \max \left( \frac{A}{\gamma^{-1} + \gamma_d^{-1}}, \frac{2\tilde{A}\gamma_d}{1 + \sqrt{1 + \frac{8\pi e^2 \tilde{A}\gamma_d^2}{\chi \rho}}} \right). \qquad (2.10)$$

As we can see both limits of the model have the same qualitative behaviour at high donor densities – the carrier density in graphene saturates at $n_*$ or $\tilde{n}_*$. A more detailed analysis shows that in most applications both limits provide the same qualitative and similar quantitative results. Thus in further calculations we will restrict our analysis to the limit $\rho l \to 0$ and use a simplified charge balance equation

$$\gamma \left[ A - \frac{e^2 d(n + n_g)}{\varepsilon_0} - \epsilon_F \right] = n + n_g. \qquad (2.11)$$

In the case when the charge transfer is dominated by donors on the surface of SiC (limit a) with $A \sim 1$ eV or donors in the bulk of SiC with $\tilde{A} \sim 1$ eV, [61], we estimate that the saturation density of n-type doping of MLG is $1 \cdot 10^{13}$ cm$^{-2}$, which corresponds to $\epsilon_F \approx 0.4$ eV (for $d \approx 0.3$nm). This value of carrier density occurs when the donor volume density is $\rho > \rho_* \sim 1 \cdot 10^{19}$ cm$^{-3}$ (we use $\chi \sim 10$ for 6H SiC [62]) or the surface states have DoS $\gamma > \gamma_* \sim 1 \cdot 10^{13}$ cm$^{-2}\cdot$eV$^{-1}$. For lesser doping of SiC, $\gamma < \gamma_*$ and $\rho < \rho_*$, one should use the larger of the estimates from Eqs. (2.5, 2.7). This can be compared to the data reported in the recent studies of epitaxial graphene indicating a substantial intrinsic level of n-type doping of G/SiC, very often [27] as high as $1 \cdot 10^{13}$ cm$^{-2}$. However, some particular growth processes produce G/SiC with a much lower doping level [28, 63], indicating that efficient annealing of donors on and near the SiC surface is possible.

## 2.2.2 The effect of spontaneous polarization of SiC on charge transfer

In this section we incorporate the effect of charge redistribution between donors in SiC due to the SP (see section 2.1.3) in our charge transfer model (2.1, 2.2). The main effect of the SP on the charge transfer is the increased thickness of the depletion layer near the Si-terminated surface of SiC, which is characterized by the

additional hole density $n_p = P_0/e$. This density must be included in the Eq. (2.1) to ensure the charge neutrality of the system:

$$\gamma \left[ A - \frac{e^2 d(n + n_g)}{\varepsilon_0} - \epsilon_F \right] + \rho l = n + n_g + P_0/e. \qquad (2.12)$$

The second equation (2.2) of the model remains unaffected by the SP. We can introduce a new parameter $A_{eff} = A - P_0/(e\gamma)$, so that

$$\gamma \left[ A_{eff} - \frac{e^2 d(n + n_g)}{\varepsilon_0} - \epsilon_F \right] + \rho l = n + n_g. \qquad (2.13)$$

Thus, the effect of the SP of SiC can be described by the same charge transfer Eqs. (2.1, 2.2) with the substitution $A \to A - P_0/(e\gamma)$. In the future calculations we implicitly assume that the effect of the SP is included in the definition of $A$.

## 2.2.3  Responsivity of G/SiC FET

Since the intrinsic doping of G/SiC is often too high for applications in electronic devices, it is important to be able to reduce the doping using external gates. Here we discuss the feasibility of controlling the carrier density of graphene using a metallic gate. We characterize the effectiveness of this control using the responsivity factor

$$r = -\frac{dn}{dn_g}. \qquad (2.14)$$

The values $r \approx 1$ correspond to an optimal transistor operation, when the change of the gate voltage results in transfer of all additional charge from gate to graphene. In the opposite regime, $r \ll 1$, the carrier density of graphene is nearly impossible to change using a gate voltage.

The responsivity of MLG in G/SiC in the limit (a) is

$$r|_{n_g=0} = 1 - \left(1 + \frac{\gamma_A}{\gamma_d} + \frac{\gamma_A}{\gamma}\right)^{-1/2} \approx$$

$$\approx \begin{cases} 1, & \gamma \ll \gamma_*; \\ 1 - \dfrac{1}{\sqrt{1 + \gamma_A/\gamma_d}}, & \gamma \gg \gamma_*. \end{cases} \tag{2.15}$$

The responsivity, $r|_{n_g=0}$ of MLG/SiC in the limit (b) can be described using Eq. (2.15), but with $\gamma_A$ replaced by $\tilde{\gamma}_A$ and the upper/lower limits corresponding to $\rho \ll \rho_*$ and $\rho \gg \rho_*$, respectively.

This result indicates that the responsivity of the MLG/SiC field-effect transistor depends on the density of donors in the buffer layer. At small densities, which correspond to low initial carrier density in graphene, the responsivity is close to 1 and the transistor operation can be controlled effectively. In contrast, at high donor density and high graphene doping the carrier density $n$ is hard to change. This result explains the motivation for reducing the carrier density in graphene by using metallic and polymer gates, described in section 2.1.4.

## 2.2.4 Intrinsic doping of quasi-free standing graphene (QFMLG) on H-intercalated SiC

Here we develop a phenomenological theory of charge transfer between graphene and SiC in hydrogen-intercalated epitaxial graphene and compare two limiting phenomenological models for that, which differ by the form of the density of states of surface acceptors, $\gamma(\epsilon)$. In the **model I** we assume that $\gamma(\epsilon)$ has the shape of a narrow peak,

$$\gamma(\epsilon) = \frac{n_v}{\sqrt{\pi}\Delta}\exp\left(-\frac{(\epsilon - E_I)^2}{\Delta^2}\right) \to n_v\delta(\epsilon - E_I), \tag{2.16}$$

where $n_v$ is the density of vacancies, $E_I$ is the average localized state energy, $\Delta \ll E_G - E_I$ is a variation of the energy level due to the imperfection of the

crystal structure, and $E_G$ is the work function of graphene. The **model II** assumes a uniform density of states

$$\gamma(\epsilon) = \gamma_0 \qquad (2.17)$$

broadly spread over the gap in SiC. To justify the model I we notice that acceptor states are likely to be due to occasional unsaturated Si bonds at the locations of "vacancies" in the hydrogen layer, which does not experience reconstruction. The occasional vacancies in simple hydrogen lattice have identical properties, including the energy of the created acceptor states, resulting in a peak-shape of their density. The reason to consider the model II is that other types of defects can dominate in the formation of localized states with energies spread over a broad region with the work function smaller than that of a free-standing undoped graphene. A model similar to the model II has already been used to describe the charge transfer in epitaxial graphene on SiC without hydrogenation[1] [45] with the difference that in that case the surface states had a work function larger than that in graphene.

Below, we apply both models to find the hole density in graphene and the responsivity factor describing the effectiveness of QFMLG carrier density control by a gate voltage in a field-effect transistor. For both models, we find that the quantum capacitance of graphene plays an important role in determining the charge transfer. The electron transfer from QFMLG to surface acceptor states is described by the following equation,

$$n - n_g = \int\limits_{E_{min}}^{\epsilon(n)} d\epsilon \, \gamma(\epsilon); \qquad (2.18)$$

$$\epsilon(n) = E_G - \frac{e^2 d}{\epsilon_0}(n - n_g) + \epsilon_F(n), \qquad (2.19)$$

where $n$ is the density of holes in graphene, $n_g = CV_g/e$ ($V_g$ is the gate voltage),

---

[1]In epitaxial graphene the buffer carbon layer, experiencing $(6\sqrt{3} \times 6\sqrt{3})$ R30° reconstruction, has large unit cells (216 atoms). Occasional defects in this layer have many possible inequivalent positions within the supercell, creating localized states with different energies. This results in a broadly distributed density of states, approximated by a uniform energy distribution.

$d$ is the distance between SiC and QFMLG, and $E_{min} = -\infty$ for the model I and $E_{min} = E_{II}$ for the model II ($E_{II}$ is the work function for surface acceptor in SiC). Note that the integral in Eq. (2.18) is taken over the electron (rather than hole) energy. Each of the models is characterized by one energy parameter: $A = E_G - E_I$ for model I and $A = E_G - E_{II}$ for model II. The susceptibility of the Fermi energy $\epsilon_F(n) = -\hbar v \sqrt{\pi n}$ (relative to the graphene Dirac point), to the carrier density $n$ is the reason for a strong effect of the quantum capacitance of graphene on the charge transfer [65, 66, 67, 68].

The value of the carrier density for non-gated structures can be obtained by solving Eq. (2.18) for $n_g = 0$. In Fig. 2.8(a) we illustrate the hole density dependence in graphene on the amount of acceptors on hydrogenated SiC. For the model I, it is

$$n_I = \min\left[n_v, n_b\right]; \quad n_b = \frac{4A^2}{\pi \hbar^2 v^2 \left(1 + \sqrt{1 + \frac{4e^2 dA}{\pi \varepsilon_0 \hbar^2 v^2}}\right)^2}. \tag{2.20}$$

At a small $n_v$, all acceptor levels are occupied and $n_I = n_v$. As acceptor density $n_v$ increases, graphene doping saturates at $n_I \approx 1 \cdot 10^{13}$ cm$^{-2}$. The model II also shows a saturation of the carrier density, but with a smoother crossover,

$$n_{II} = \frac{4A^2}{\pi \hbar^2 v^2 \left(1 + \sqrt{1 + \frac{4A}{\pi \hbar^2 v^2}\left(\frac{1}{\gamma_0} + \frac{e^2 d}{\varepsilon_0}\right)}\right)^2}. \tag{2.21}$$

The effectiveness of using QFMLG transistors can be characterized by the responsivity factor, $r = dn/dn_g$. The responsivity factors for the models I and II,

$$r_I = 1 - \frac{1 + \text{sign}(n_v - n_b)}{2\sqrt{1 + \frac{4e^2 dA}{\pi \hbar^2 v^2 \varepsilon_0}}}; \tag{2.22}$$

$$r_{II} = 1 - \frac{1}{\sqrt{1 + \frac{4A}{\pi \hbar^2 v^2}\left(\frac{1}{\gamma_0} + \frac{e^2 d}{\varepsilon_0}\right)}}, \tag{2.23}$$

are compared graphically in Fig. 2.8b.
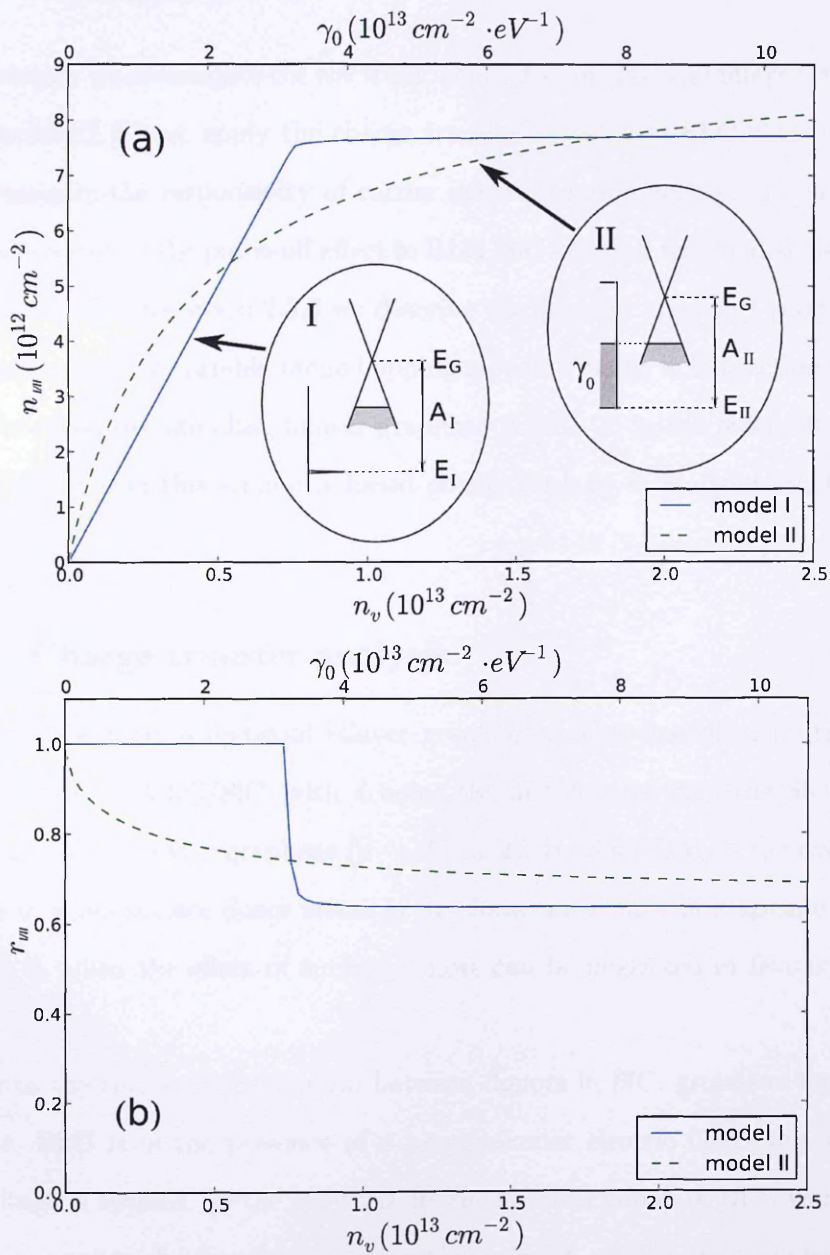
Figure 2.8: a) The dependence of the hole density $n$ in QFMLG on the acceptor density (see $n_v$ axis for the model I and $\gamma_0$ axis for the model II). The insets show charge distribution between graphene and acceptor states for both models. b) Responsivity factor $r$ dependence on $n_v$. The following parameters were used for both plots: $d = 0.3$ nm, $A_I = 0.6$ eV, $\Delta = 5$ meV, $A_{II} = 0.7$ eV.

38

## 2.3 Epitaxial bilayer graphene and BLG/SiC transistors

In this section we investigate the electronic properties of epitaxial bilayer graphene. In subsection 2.3.1 we apply the charge transfer model to a BLG/SiC transistor and investigate the responsivity of carrier density to gate voltage. In subsection 2.3.2 we investigate the pinch-off effect in BLG/SiC and find the conditions needed to achieve it. In subsection 2.3.3 we describe the electron transport properties of the system using the variable-range hopping model. Finally, in subsection 2.3.4 we study the quasi-free standing bilayer graphene (QFBLG) in the pinch-off regime.

The material in this section is based on the work by S. Kopylov, V. I. Fal'ko (2011).

### 2.3.1 Charge transfer analysis

The charge balance in epitaxial bilayer graphene can be described by the same Eqs. (2.1, 2.2) as MLG/SiC, with $d$ being the distance between the SiC surface and the middle of bilayer graphene $(d \to d + c_0/2)$. Here we analyze the two limits: (a) $\rho \to 0$, when surface donor states is the dominant source of graphene doping; (b) $\gamma \to 0$, when the effect of surface donors can be neglected in favour of bulk donors.

Due to the charge redistribution between donors in SiC, graphene layers and the gate, BLG is in the presence of a perpendicular electric field even when no gate voltage is applied. In the experiments the spectral gap $\Delta$ of BLG usually has a value in a range of a few dozen meV, which is much smaller than the bottom of the high-energy band in bilayer graphene $(\Delta \ll \epsilon_1)$. This allows us to neglect the gap $\Delta$ and use Eq. (1.12) to write

$$
\epsilon_F(n) = \begin{cases} \sqrt{\dfrac{\epsilon_1^2}{4} + \pi \hbar^2 v^2 n} - \dfrac{\epsilon_1}{2}, & n < n_1, \\ \hbar v \sqrt{\dfrac{\pi n}{2}}, & n > n_1, \end{cases} \tag{2.24}
$$

where $n_1 = 2\epsilon_1^2/(\pi\hbar^2 v^2) \approx 3 \cdot 10^{13}$ cm$^{-2}$.

In the limit (a), this gives

$$n = \frac{2A(A + \epsilon_1)/(\pi\hbar^2 v^2)}{1 + \frac{\tilde{\gamma}_1}{\gamma_d} + \frac{\tilde{\gamma}_1}{\gamma} + \sqrt{\left(1 + \frac{\gamma_1}{\gamma_d} + \frac{\gamma_1}{\gamma}\right)^2 + \frac{\gamma_A}{\gamma_d} + \frac{\gamma_A}{\gamma}}} \qquad (2.25)$$

for $n < n_1$ and $n_g = 0$. Here, $\gamma_1 = \epsilon_1/\pi\hbar^2 v^2$ and $\tilde{\gamma}_1 = \gamma_1 + \gamma_A/2$. For larger densities, $n > n_1$,

$$n = \frac{8A^2}{\pi\hbar^2 v^2} \frac{1}{\left(1 + \sqrt{1 + \frac{2\gamma_A}{\gamma} + \frac{2\gamma_A}{\gamma_d}}\right)^2}, \qquad (2.26)$$

which resembles Eq. (2.3) for MLG, but with $\gamma_A \to 2\gamma_A$.

Similarly to MLG, the density in BLG/SiC saturates upon the increase of the surface DoS of donors. The crossover to the saturated density, $n_*(A) = A\gamma_*(A)$, occurs at

$$\gamma_* = \begin{cases} \dfrac{2\gamma_A}{\left(1 + \sqrt{1 + \frac{2\gamma_A}{\gamma_d}}\right)^2}, & \dfrac{2\gamma_1}{\gamma_d} + 1 < \dfrac{\gamma_A}{4\gamma_1}; \\[4mm] \dfrac{\frac{\gamma_A}{2} + 2\gamma_1}{1 + \frac{\gamma_A}{2\gamma_d} + \frac{\gamma_1}{\gamma_d} + \sqrt{\left(1 + \frac{\gamma_1}{\gamma_d}\right)^2 + \frac{\gamma_A}{\gamma_d}}}, & \dfrac{2\gamma_1}{\gamma_d} + 1 > \dfrac{\gamma_A}{4\gamma_1}. \end{cases} \qquad (2.27)$$

The dependence of $n(\gamma)$, $\gamma_*(A)$ and $n_*(A)$ on the relative size of the band splitting $\epsilon_1$, and the graphene-surface donors work function $A$ is shown in Fig. 2.7 (a-c). The responsivity of the BLG to the gate voltage is high or low, depending on whether the saturation regime for the carrier density is reached, or not. For $\gamma \ll \gamma_*$, $r \approx 1$. For $\gamma \gg \gamma_*$,

$$r \approx \begin{cases} 1 - \dfrac{1}{\sqrt{1 + \frac{2\gamma_A}{\gamma_d}}}, & \dfrac{2\gamma_1}{\gamma_d} + 1 < \dfrac{\gamma_A}{4\gamma_1}; \\[4mm] 1 - \dfrac{1}{\sqrt{\left(1 + \frac{\gamma_1}{\gamma_d}\right)^2 + \frac{\gamma_A}{\gamma_d}}}, & \dfrac{2\gamma_1}{\gamma_d} + 1 > \dfrac{\gamma_A}{4\gamma_1}. \end{cases} \qquad (2.28)$$

In the limit (b), when $n$ is determined by charge transfer from bulk donors in

SiC,

$$n = \begin{cases} \sqrt{\dfrac{\tilde{A}\chi\rho}{2\pi e^2}}, & \rho \ll \rho_*; \\ \tilde{n}_*, & \rho \gg \rho_*; \end{cases} \qquad \rho_* = \dfrac{2\pi e^2 (\tilde{n}_*)^2}{\chi \tilde{A}},$$

with $\tilde{n}_* = n_*(\tilde{A})$, and the responsivity $r \approx 1$ of BLG requires that $\rho \ll \rho_*$, whereas for $\rho \gg \rho_*$ the responsivity is described by the same limits as in Eq. (2.28), with $\gamma_A$ replaced by $\tilde{\gamma}_A$.

The results obtained in both limits $\gamma \to 0$ and $\rho \to 0$ are qualitatively similar. A more detailed analysis shows that in most of the applications both sources of donors have similar effects on the parameters of the transistor. For the sake of simplicity we will perform the future calculations for BLG in the limit (a) $\rho \to 0$.

### 2.3.2 Pinch-off in BLG/SiC
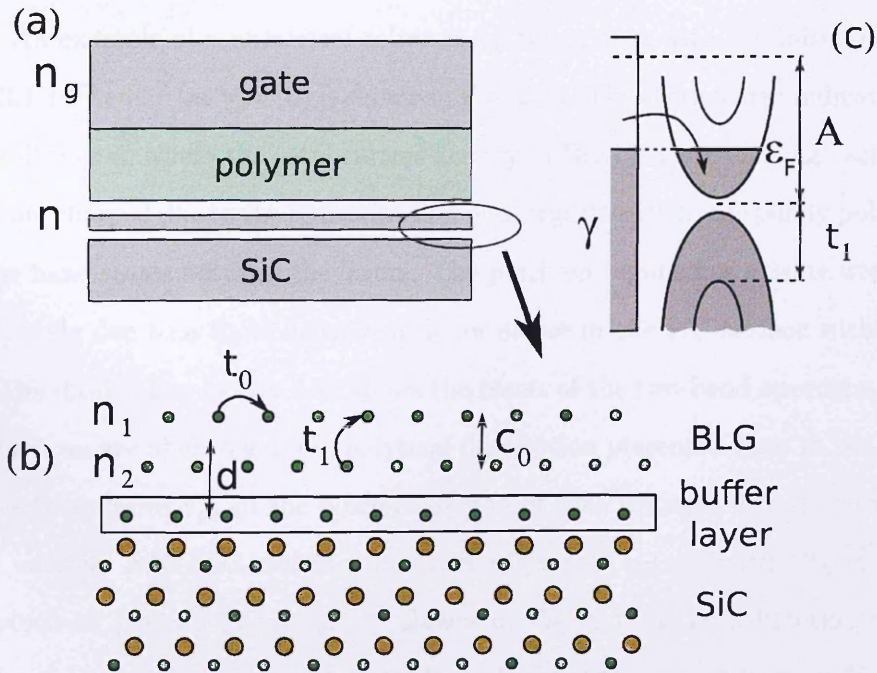


Figure 2.9: a) Epitaxial bilayer graphene/polymer heterostructure. b) The structure of the buffer layer. c) Bilayer graphene spectrum and charge redistribution between graphene and SiC.

The gap in the spectrum of BLG provides a possibility to observe the pinch-off effect - the total density of carriers in graphene vanishes when the Fermi level of

carriers in BLG/SiC lies within the graphene spectral gap. We investigate this effect in epitaxial bilayer graphene-polymer heterostructure at small temperatures $(T \ll \Delta)$ (Fig. 2.9(a)), aiming to determine the conditions when the pinch-off of electronic transport in BLG takes place. In this device the BLG carrier density is controlled by a gate voltage $V_g = -eln_g/\varepsilon_0 + \epsilon_F/e$. Here we perform a numerical study to find a range of gate voltages required to achieve the pinch-off. We use both the full four-band BLG spectrum in Eq. (1.11) and a simplified two-band model approximation for the BLG band structure to obtain analytical results.

Eqs. (1.11, 2.18, 1.13, 1.14) provide us with the complete description of the system. To solve equations (1.11, 2.18, 1.13, 1.14) for a given gate voltage $V_g$, we represent the densities $n$, $n_1$, and $n_2$ as functions of $\epsilon_F$ and $\Delta$. This leaves us with two non-linear equations (2.18, 1.13) to find the values of $\epsilon_F$ and $\Delta$, which can be solved numerically and, then, use them to compute the electron density $n$ in BLG. An example of a numerical solution for the system with the initial density $n_0 \approx 3.1 \cdot 10^{12}$ cm$^{-2}$ (at $V_g = 0$) is shown in Fig. 2.10. The shaded area indicates the pinch-off region, where the total carrier density in BLG is zero, although separate layers are charged due to the redistribution of charge density in the partly polarised valence band states between the layers. The pinch-off regime has a finite width on the $V_g$ scale due to a finite density of donor states in the SiC surface within the gap. The dashed line in Fig. 2.10 shows the result of the two-band approximation, for which we are able to get an analytical description presented later in the text.

The boundaries $V_{g\pm}$ of the pinch-off region of gate voltages correspond to the Fermi energies in G/SiC crossing the band edges, i.e., $\epsilon_F = \pm\epsilon_1|\Delta|/2\sqrt{\epsilon_1^2 + \Delta^2}$. The pinch-off plateau $(V_{g-}, V_{g+})$ is shown in Fig. 2.11(a) as a function of the density of donor states $\gamma$. The density dependence of the gate voltage, $n(V_g)$ near the edges of pinch-off $(V_g \approx V_{g\pm})$ is linear,

$$V_g > V_{g+}, n \propto V_g - V_{g+}; \quad V_g < V_{g-}, n \propto V_g - V_{g-}. \tag{2.29}$$

The pinch-off plateau can be characterized by its middle value $V_{g0} = (V_{g+} + V_{g-})/2$
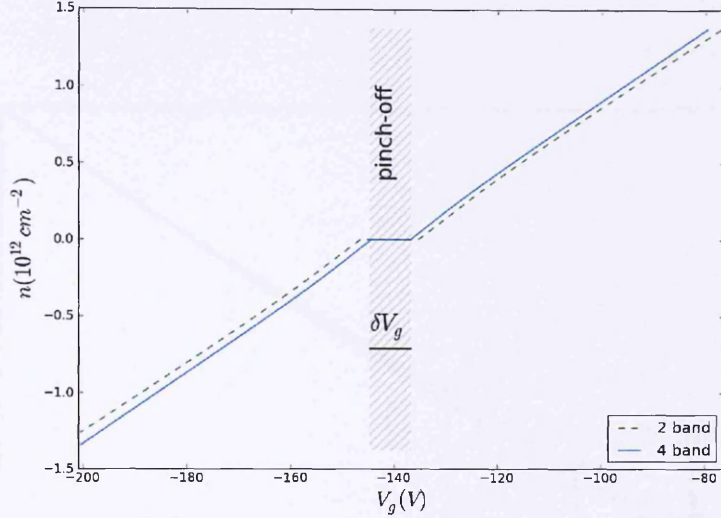
Figure 2.10: Carrier density $n$ as a function of gate voltage $V_g$ for epitaxial graphene for two-band and four-band models. The pinch-off area is dashed. The calculation was performed for $l = 200$ nm, $d = 0.2$ nm, $A = 1$ eV.

and by the width $\delta V_g = V_{g+} - V_{g-}$, which are shown in Fig. 2.11(b) as functions of the initial density $n_0$. For small initial doping of BLG, $n_0 \ll mA/\hbar^2$, we find that $V_{g0} \propto n_0$ and $\delta V_g \propto n_0^2$. The spectral gap $\Delta_{max}$ in the middle of the pinch-off plateau is shown in the inset in Fig. 2.11(b) and can reach the value $\Delta \approx 50$ meV (for $n_0 \approx 3 \cdot 10^{12}$ cm$^{-2}$).

To provide an analytical description of the pinch-off regime we use the 2-band approximation Eqs. (1.17-1.19), which is justified by the relation $\Delta \ll \epsilon_1$. For the practical use of results, we relate the density of donor states $\gamma$ to the initial carrier density $n_0$. For that we solve the system of Eqs. (2.18, 1.13, 1.17, 1.19) with $V_g = 0$, neglecting $\Delta^2/\epsilon_F^2$ terms (which is justified *a posteriori*),

$$\gamma \approx \frac{1}{A/n_0 - e^2 d/\varepsilon_0 - \pi\hbar^2/m}. \tag{2.30}$$

The boundaries of the pinch-off region (see Fig. 2.11(a)) are given by

$$V_{g\pm} \approx -\frac{elA/\varepsilon_0}{1/\gamma_f \mp 1/(2\gamma_l)}; \quad \gamma_l \approx \gamma_c + \frac{m}{4\pi\hbar^2} \ln\left(\frac{2\epsilon_1\gamma_c}{A\gamma_f}\right), \tag{2.31}$$
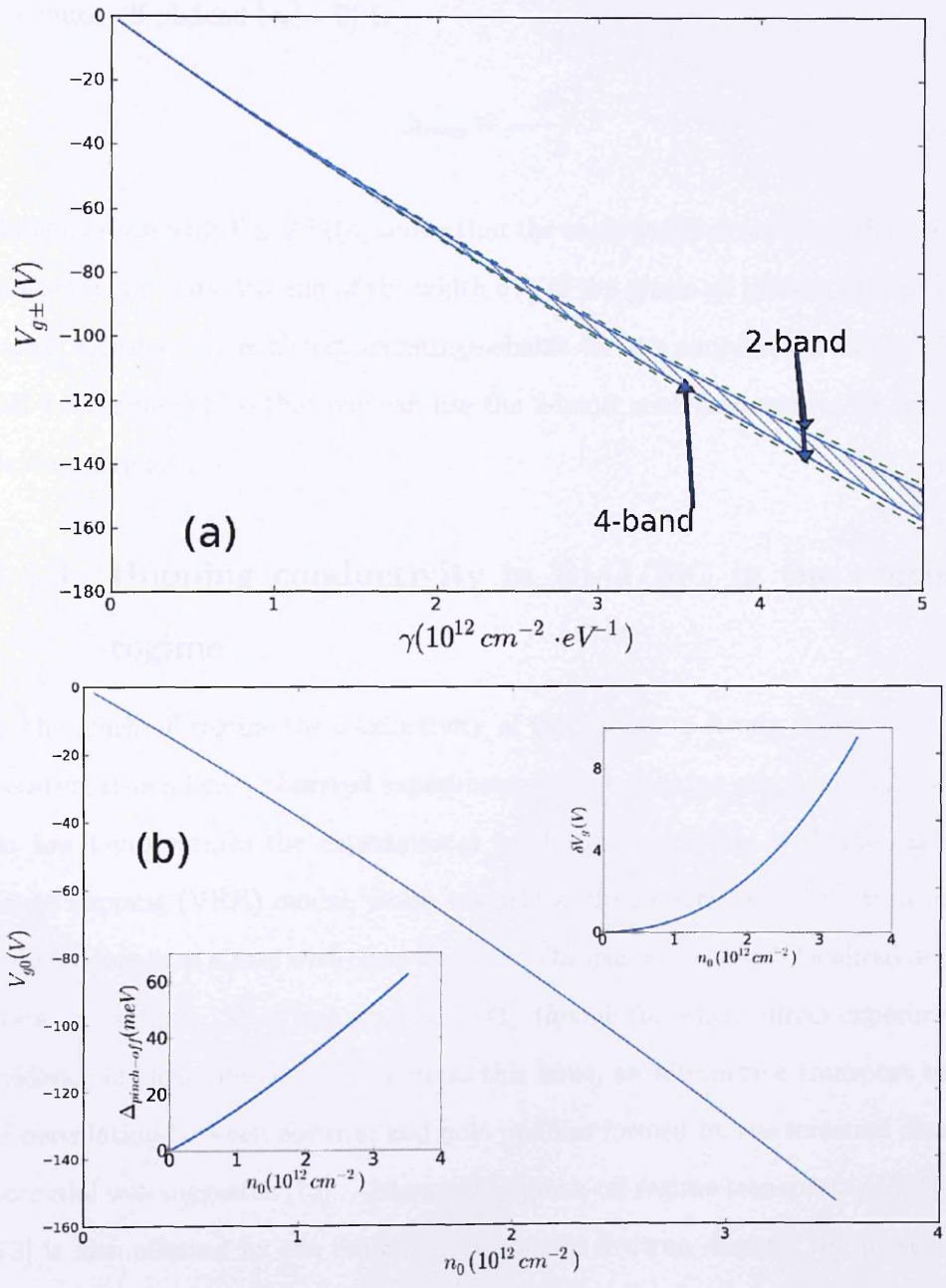
Figure 2.11: a) The pinch-off region of gate voltages $(V_{g-}, V_{g+})$ as a function of the density of surface donor states $\gamma$. b) The middle of the pinch-off plateau $V_{g0}$, the width of the plateau $\delta V_g$ and the spectrum gap $\Delta_{max}$ as functions of the initial carrier density $n_0$ in epitaxial graphene.

where $1/\gamma_f = A/n_0 - \pi\hbar^2/m$, $\gamma_c = \varepsilon_0\varepsilon_r/e^2c_0$, correspond to Fermi energies at the boundaries of the spectral gap $\epsilon_F = \pm|\Delta|/2$. The spectral gap in the middle of the pinch-off plateau ($\epsilon_F = 0$) is

$$\Delta_{max} \approx -\frac{A\gamma_f}{\gamma_l}. \qquad (2.32)$$

A comparison with Fig. 2.11(a) shows that the analytically determined dependence of the middle value $V_{g0}$ and of the width $\delta V_g$ of the pinch-off plateau on the initial carrier density, $n_0$, is almost indistinguishable for the simplified 2-band and the full 4-band model, so that one can use the 2-band analytical results for practical device modelling.

## 2.3.3 Hopping conductivity in BLG/SiC in the pinch-off regime

In the pinch-off regime the conductivity of BLG shows a strong exponential temperature dependence, observed experimentally in exfoliated graphene [33, 69, 70]. At low temperatures the experimental results are consistent with the variable-range hopping (VRH) model, which underlines the importance of electron jumps between localized states with close energies. The existence of such localized midgap states in exfoliated BLG was studied in [71], though there is no direct experimental evidence of their presence. To address this issue, an alternative transport model of percolation between electron and hole puddles formed by the screened disorder potential was suggested [72]. Although the pinch-off regime transport in BLG/SiC [73] is also affected by the inhomogenity of the electron density, the presence of localized surface states in a wide energy range justifies the use of the VRH model. Here we analyze the temperature dependence of the conductivity in both the Mott [74] and Efros-Shklovskii [75, 76] regimes and find the crossover temperature.

In the pinch-off regime the transport properties of BLG can be described by the variable-range hopping model. The electron hopping between acceptor sites in

SiC by means of phonon scattering into localized BLG states is characterized by the hopping rate

$$W_{ij} = \nu_0 \exp(-2\alpha R_{ij} - |E_{ij}|/T), \qquad (2.33)$$

where $R_{ij}$ is the distance between acceptor sites with indices $i$ and $j$, $E_{ij}$ - the energy difference between the corresponding levels, and $\alpha = \sqrt[4]{m^2(\Delta^2/4 - \epsilon_F^2)}/\hbar$. Here we utilise the technique for calculating the hopping conductivity in disordered systems developed in [77]. This technique is based on linearised master equations and provides the value of conductivity in the two-site effective medium approximation

$$\sigma(T) = \frac{e^2}{6T} n_e (1 - n_e/n_a) \langle R^2 \rangle \sigma_1(T), \qquad (2.34)$$

where $n_a = \gamma\Delta$ is the density of acceptors, $n_e$ - the density of occupied acceptor states, and

$$\langle R^2 \rangle = \int \int \frac{R^2}{\mathrm{e}} \frac{\rho(E) d\mathbf{R} dE}{1 + \sigma_1 W_{ij}^{-1}}, \qquad (2.35)$$

where $\langle \ldots \rangle$ is a configurational average, $\rho(E)$ is the density of localized states per unit area, and $\mathrm{e} \approx 2.71$. For each temperature $T$, the parameter $\sigma_1(T)$ is determined from the self-consistency equation

$$\mathrm{e} = \int \int \frac{\rho(E) d\mathbf{R} dE}{1 + \sigma_1 W_{ij}^{-1}}. \qquad (2.36)$$

We apply the described formalism to both the Mott and Efros-Shklovskii regimes, which differ by the shape of density of states $\rho(E)$ near the Fermi level. At higher temperatures, the Mott regime characterized by a constant density of states $\rho(E) = \gamma$ is relevant [74]. At lower temperatures, the Coulomb interaction between localized electrons creates a soft gap in the density of states near the Fermi level: within the gap $\rho(E) = A_2|E - \epsilon_F|(4\pi\varepsilon_0\varepsilon_r)^2/e^4$ is linear and it saturates at the value $\rho(E) = \gamma$ [75, 76]. The factor $A_2 = 2/\pi$ has been calculated in [78] and is thought to be universal for systems with disorder.

To solve Eq. (2.36), we first perform the integration over the distance $R$, by
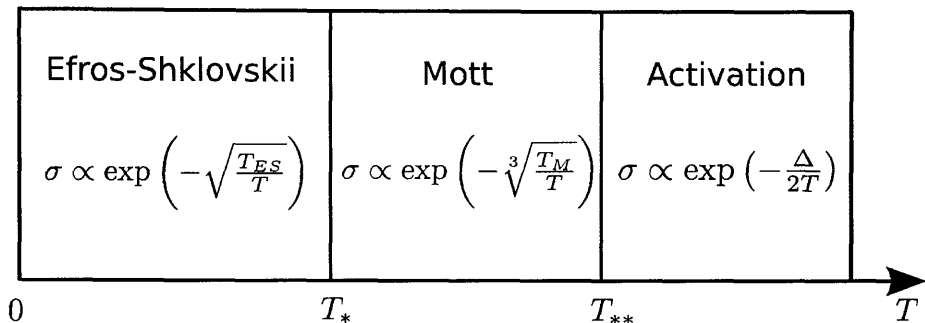
Figure 2.12: The transport regimes of BLG/SiC in the pinch-off regime at different temperatures. $T_*$ and $T_{**}$ represent the cross-over temperatures.

substituting $y = 2\alpha R$,

$$f(A) = \int\limits_{0}^{+\infty} \frac{y^d \, dy}{1 + A^{-1}e^y} \approx \begin{cases} \frac{\ln^{d+1}(A)}{d+1}, & A \gg 1; \\ d!A, & A \ll 1. \end{cases} \tag{2.37}$$

After this, we find that the dominant contribution to the integral over energy $E$ ($\nu_0 \gg \sigma_1$, $x = E/T$)

$$I_d = \int\limits_{0}^{+\infty} x^d dx \, f\left(\frac{\nu_0}{\sigma_1}e^{-x}\right), \tag{2.38}$$

comes from the region $x \in [0, \ln(\nu_0/\sigma_1)]$, where $A > 1$ in Eq. (2.37), and arrive at

$$I_d = \frac{\ln^{d+3}(\nu_0/\sigma_1)}{(d+1)(d+2)(d+3)}. \tag{2.39}$$

Then we take into account that the only factor in Eq. (2.34) which yeilds an exponential temperature dependence of $\sigma(T)$ is $\sigma_1$, and find, with exponential accuracy, that

$$\sigma_M \propto \exp\left(-\sqrt[3]{\frac{T_M}{T}}\right), \quad T_M = \frac{6em\Delta}{\pi\hbar^2\gamma} \tag{2.40}$$

in the VRH Mott regime for $T > T_*$, and

$$\sigma_{ES} \propto \exp\left(-\sqrt{\frac{T_{ES}}{T}}\right), \quad T_{ES} = \frac{\sqrt{3}e}{2\pi}\frac{e^2\sqrt{m\Delta}}{\hbar\varepsilon_r\varepsilon_0} \tag{2.41}$$

in the VRH Efros-Shklovskii regime for $T < T_*$, where the cross-over temperature

is given by

$$T_* = \frac{1}{32\pi\sqrt{3}\mathrm{e}} \frac{e^6\gamma^2\hbar}{\varepsilon_r^3\varepsilon_0^3\sqrt{m\Delta}}. \tag{2.42}$$

At higher temperatures the dominant regime of electron transport is the activation hopping from the middle of the gap to the bottom of the low-energy band. The conductivity in this regime,

$$\sigma_A \propto \exp\left(-\frac{\Delta}{2T}\right), \tag{2.43}$$

is achieved at temperatures above the second cross-over temperature

$$T_{**} = \frac{\pi^2\hbar^4\gamma^2\Delta}{288e^2m^2}. \tag{2.44}$$

### 2.3.4   Charge transfer in QFBLG

Similarly to the fabrication method of QFMLG, hydrogen intercalation can be applied to MLG/SiC to decouple the buffer layer from Si atoms and produce quasi-free standing bilayer graphene (QFBLG). This procedure improves the transport properties of graphene and reduces the high intrinsic carrier density. Here we find the gate voltages required to achieve the pinch-off regime in QFBLG.

In the case of QFBLG, unsaturated Si-bonds form a narrow peak in the density of acceptor states $\gamma(\epsilon) \approx n_a\delta(\epsilon - \epsilon_a)$ at the energy $\epsilon_a$, which is below the graphene Dirac point. We only consider the regime, where all acceptor states are occupied and the charge balance equation reads

$$n + n_g + n_a = 0. \tag{2.45}$$

The full description of QFBLG of the system is provided by Eqs. (1.11, 2.45, 1.13, 1.14), where $n = -n_h$ ($n_h$ is the density of holes in BLG). Solving these equations we find the dependence of the electron density $n$ on the gate voltage $V_g$ is shown in Fig. 2.13(a). Also, we calculate the gate voltage corresponding to the

middle of the pinch-off plateau $V_{g0}$, the width of the plateau $\delta V_g$ and the band gap $\Delta_{max}$, which are shown in Fig. 2.13(b)

$$V_{g0} \approx -\frac{eln_0}{\varepsilon_0}; \quad \delta V_g \approx \frac{n_a/e}{\gamma_c + \frac{m}{4\pi\hbar^2}\ln\left(\frac{2\epsilon_1\gamma_c}{n_a}\right)}; \quad (2.46)$$

$$\Delta_{max} \approx \frac{n_a}{\gamma_c + \frac{m}{4\pi\hbar^2}\ln\left(\frac{2\epsilon_1\gamma_c}{n_a}\right)}. \quad (2.47)$$

We find that the pinch-off plateau is much narrower than in the case of BLG/SiC with a uniform surface density of donor states $\gamma$. The width of the plateau $\delta V_g$ in the latter case is mainly determined by the change in electrostatic potential difference $-eln_g/\varepsilon_0$ due to charge transfer between donor states and the gate in the pinch-off regime. These values determine the parametric regime, where the pinch-off in QFBLG-based FET is achieved.
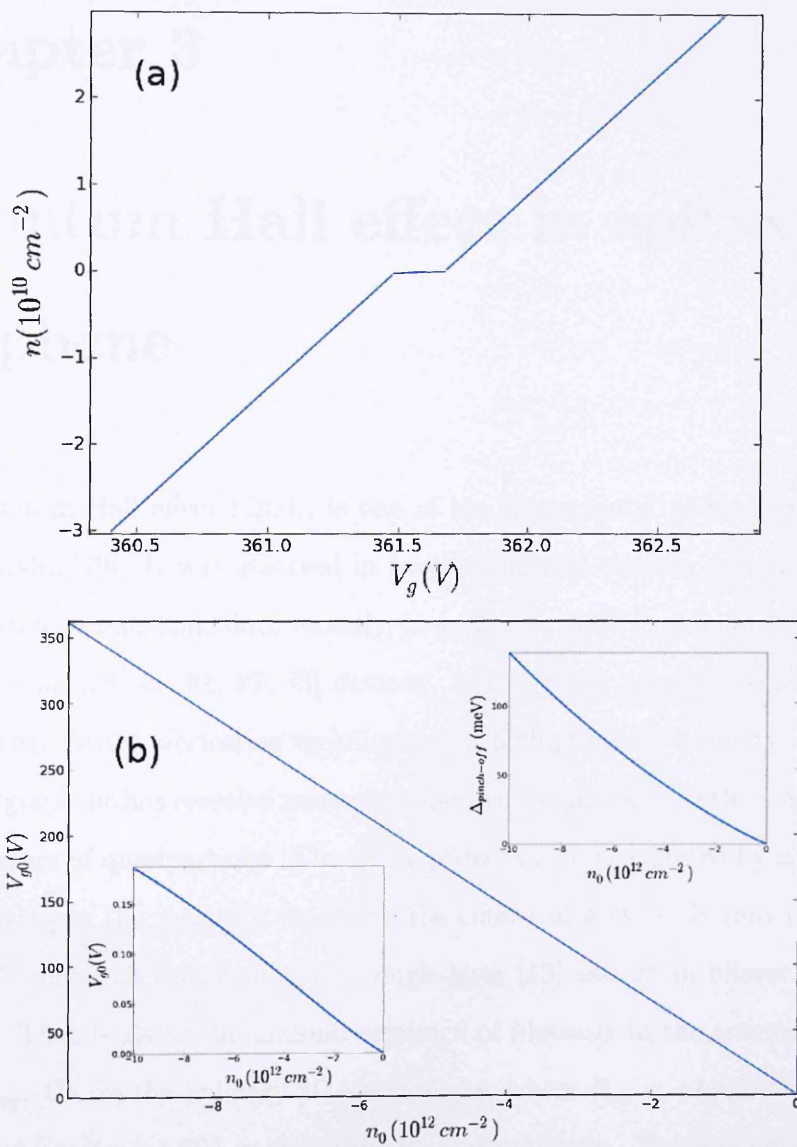
Figure 2.13: a) Carrier density $n$ as a function of gate voltage $V_g$ for QFBLG. b) The middle value of the pinch-off plateau $V_{g0}$, the width of the plateau $\delta V_g$ and the spectrum gap $\Delta_{max}$ as functions of the initial carrier density $n_h^{(0)}$ in QFBLG.

# Chapter 3

# Quantum Hall effect in epitaxial graphene

The quantum Hall effect (QHE) is one of the fundamental phenomena in solid state physics [79]. It was observed in two-dimensional electron systems in semi-conductor materials and, since recently, in graphene: both in exfoliated [3, 13, 80] and epitaxial [28, 43, 81, 82, 83] devices. It was made possible because of the high quality device fabrication techniques and high graphene mobility. However, QHE in graphene has revealed unusual properties stemming from the massless and chiral nature of quasiparticles. The Berry phase, which is acquired by a quasiparticle moving in the magnetic field over the course of a cycle, is zero in conventional 2D materials, but equals $\pi$ in single-layer [13] and $2\pi$ in bilayer graphene [16, 84]. That leads to the unusual sequence of plateaux in the transverse resistance $R_{xy}$. Unlike the ordinary 2D electron gas, where $R_{xy} = \pm h/(2ne^2)$ ($n \geq 1$), $R_{xy} = \pm h/(4e^2(n + 1/2))$, $n \geq 0$ in monolayer graphene. The resistance quantization is observed when the occupation of Landau levels, that is characterized by the filling factor $\nu$, is $\nu = 4(n + 1/2)$, which explains the name "half-integer QHE" due to the 1/2 shift.

The quantum Hall effect allows the international standard for resistance to be defined in terms of the electron charge and Planck's constant alone. The QHE

resistance standard is believed to be accurate (no corrections to the fraction of $R_K = h/e^2$), universal (material-independent) and robust (same resistance over a range of magnetic field, temperature, current). However, only a very small number of 2DEG structures – Si FET and group III-V heterostructures – satisfy these requirements. New materials are sought after and graphene should in principle be an ideal material for an implementation of a quantum resistance standard because of a very large spacing of the low-lying Landau levels compared to conventional 2DEGs [85]. A direct high-accuracy comparison of the conventional QHE in semiconductors with that observed in graphene constitutes a test of the universality of this effect. The affirmative result would strongly support the pending redefinition of the SI units based on the Planck constant $h$ and the electron charge $e$ [86] and provide an international resistance standard based upon quantum metrology [87].

In this chapter we investigate the QHE in epitaxial graphene and its applications in quantum metrology. In section 3.1 we describe the spectrum of Landau levels in monolayer and bilayer graphene. Section 3.2 discusses the perspectives of using epitaxial graphene in quantum resistance metrology. In section 3.3 we apply the charge transfer theory to investigate the pinning of filling factor in epitaxial graphene. These theoretical results are confirmed by the experimental tests described in the next section 3.4. In section 3.5 we use magneto-oscillations of carrier density in graphene as a tool for studying the properties of QFMLG. Finally, in section 3.6 we investigate the transport properties of MLG/SiC Hall bar with bilayer patches.

The material in this section is based on the original publications by S. Kopylov, *et al.* [58, 64].

## 3.1 Landau levels

As with other 2D systems, the electron spectrum in graphene gets quantized in the presence of a perpendicular magnetic field. However, the equidistant distribution of Landau levels (LLs) is modified by the Dirac-type nature of electrons. The LL

spectrum of monolayer graphene in a perpendicular magnetic field $B$ can be found by calculating the eigenvalues of the Hamiltonian

$$\hat{H} = v\boldsymbol{\sigma}(\hat{\mathbf{p}} + e\mathbf{A}) \tag{3.1}$$

with $\mathbf{A} = (-B; 0)$ in the Landau gauge. Using the eigenfunctions in the form $\psi(\mathbf{r}) = e^{ikx}\phi(y)$ the system resembles the 1-dimensional harmonic oscillator. Thus, we find the LLs in graphene [13]

$$E_N = \text{sgn}(N)\sqrt{2e\hbar v^2|N|B}, \tag{3.2}$$

where $N$ is an integer LL index. Each LL has a degeneracy $g = 4$, which takes into account spin and valley degeneracy. The capacity of each level is determined by its degeneracy and the number of flux quanta penetrating the sample

$$n_{LL} = g\frac{\Phi}{\Phi_0}\frac{1}{S} = g\frac{eB}{h}, \tag{3.3}$$

where $\Phi = BS$ is the total flux through the graphene sample with the area $S$ and $\Phi_0 = e/h$ is the magnetic flux quantum. At high magnetic fields Zeeman splitting comes into effect lifting the LL degeneracy. In this thesis we do not consider this effect since it only reveals itself in the close vicinity of LLs (at the magnetic fields of interest $B < 20$ T) and is irrelevant to the discussed problems.

The spectrum of the Landau levels in bilayer graphene was extensively studied in [15, 16, 88] and is shown on Fig. 3.1. Each LL of this spectrum is 4-fold degenerate. The gap between the 0th and 1st LLs appears due to a perpendicular electric field created by the gate and charged donors. It can be calculated self-consistently using electrostatics and BLG band structure Eqs. (1.13, 1.17, 1.18, 1.19). For a typical carrier density $n_0 \sim 1 \cdot 10^{12}$ cm$^{-2}$ the gap $\Delta$ has values of a few dozen meV, which is smaller than the typical distance between LLs $\sim \hbar\omega_c$ at

$B \sim 10$ T. Thus the LLs of bilayer graphene can be calculated as [16]

$$E_N = \text{sgn}(N)\sqrt{N(N-1)\hbar^2\omega_c^2 + \Delta^2/4}, \quad \omega_c = eB/m. \qquad (3.4)$$

The energies of LLs in BLG will be used in the further analysis to study the effect of BLG patches on the QHE in MLG.



**bilayer**
$\varepsilon/\hbar\omega_c$

$\sqrt{12}$ — (4,+);(4,-)

$\sqrt{6}$ — (3,+);(3,-)

$\sqrt{2}$ — (2,+);(2,-)

$\varepsilon=0$ — (0,+);(1,+)
(0,-);(1,-)

$-\sqrt{2}$ — (2,+);(2,-)

$-\sqrt{6}$ — (3,+);(3,-)

$-\sqrt{12}$ — (4,+);(4,-)
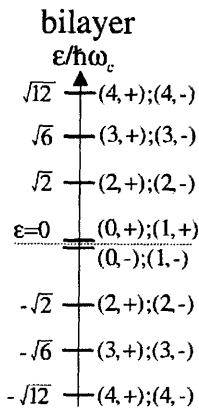
Figure 3.1: Landau level spectrum in bilayer graphene. Adapted from [16].

## 3.2  Precision resistance metrology on graphene

Graphene is believed to offer an excellent platform for QHE metrology due to the large energy separation between Landau levels (LL) resulting from the Dirac-type "massless" electrons specific for its band structure. The Hall resistance quantization with an accuracy of 3 parts in $10^9$ has been established [28] in Hall-bar devices manufactured from epitaxial graphene grown on the Si-terminated face of SiC. However, for graphene to be practically employed as a quantum resistance standard, it needs to satisfy further stringent requirements [87] in particular with respect to robustness over a range of temperatures, magnetic fields and measurement currents. A large measurement current, which a device can sustain at a given temperature without dissipation, is particularly important for precision metrology as it defines the maximum attainable signal-to-noise ratio.

The width of the QHE plateaux in magnetic fields in conventional 2D electron

systems is, usually, set by disorder and temperature. Disorder pins the Fermi energy in the mobility gap of the 2D system, and suppresses dissipative transport at low temperatures over a finite range of filling factors around the values corresponding to exactly filled LLs. These filling factors can be calculated from the carrier density $n$ determined from the low-field Hall resistivity measurements and coincide with the maximum non-dissipative current, the breakdown current. Thus, the breakdown current in conventional two-dimensional semicondutors peaks very close to the field values where the filling factor $\nu$ is an even integer [87]. Though less studied experimentally, the behaviour of the breakdown current on the plateaux for the exfoliated graphene, including the $\nu = 2$ plateau corresponding to the topologically protected $N = 0$ LL, looks quite similar [89].

Quantum Hall plateaux have been observed in graphene flakes mechanically exfoliated from bulk graphite even at room temperature, albeit with an accuracy of 0.2% (at 45 T) [5]. The highest experimentally achieved accuracy in exfoliated graphene flakes – 15 parts per million (ppm) at 300 mK [90] – is still modest by metrological standards. The main constraint appears to be the small area of the flakes, which limits the maximum non-dissipative current the system can sustain in the quantum Hall state. This is related both to high electrical resistance of the contacts and high thermal resistance of the graphene-substrate interface.

An alternative 'top-down' approach to produce graphene consists of growing it epitaxially. Epitaxial growth on SiC produces large area few-[91] or monolayer [27] graphene, however, initial attempts to observe QHE in such samples were unsuccessful. The difficulty was related to the lack of atomically accurate thickness control during the film growth on the C-terminated face of SiC, and most probably to a strong variation of carrier density across the layers grown on the Si-terminated face [92]. A breakthrough came in 2009, when several groups within days of each other managed to produce epitaxial material of sufficient quality to demonstrate the QHE features typical of monolayer graphene [28, 43, 81, 82, 83]. Here we review the progress in engineering and precise magnetotransport measurements
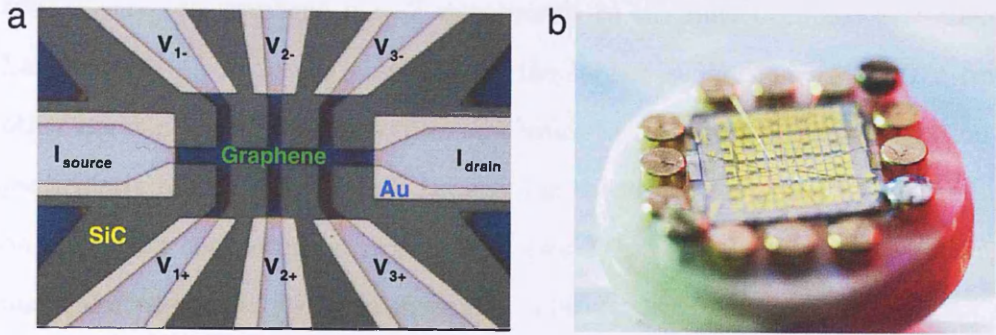
Figure 3.2: (a) Optical micrograph of a Hall bar used in the experiments. (b) Layout of a $7 \times 7$ mm$^2$ wafer with 20 Hall bars. Adapted from [58].

on epitaxial graphene devices that followed.

The first metrologically precise measurements of the quantum Hall effect in a large high-quality epitaxial sample were reported in [28]. Twenty Hall bar devices of different sizes, from 160 $\mu$m $\times$ 35 $\mu$m down to 11.6 $\mu$m $\times$ 2 $\mu$m were produced on 0.5 cm$^2$ wafer using standard electron beam lithography and oxygen plasma etching (Fig. 3.2). Atomic force microscopy (AFM) images revealed that the graphene layer covers the substrate steps like a carpet, preserving its structural integrity. Contacts to graphene were produced by straightforward deposition of 3 nm of Ti and 100 nm of Au through a lithographically defined mask followed by lift-off, with the typical area of the graphene-metal interface of $10^4$ $\mu$m$^2$ for each contact. This process favourably compares with a laborious contact preparation to a two-dimensional electron gas in conventional semiconductor technology. Using low magnetic field measurements, it was established that the manufactured material was n-doped, with the measured electron concentration in the range of $(5-8) \cdot 10^{11}$ cm$^2$, mobility about 2400 cm$^2$/V·s at room temperature and between 4000 and 7500 cm$^2$/V·s at 4.2 K, almost independent of device dimensions and orientation with respect to the substrate terraces.

Fig. 3.3 shows the longitudinal (dissipative) $R_{xx}$ and the transverse (Hall) $R_{xy}$ resistance of a 2 $\mu$m wide Hall bar at 4.2 K and magnetic fields up to 14 T. At high magnetic field there are two QHE plateaux, at $R_{xy}^{(0)} = R_K/2$ $(n = 0)$ and $R_{xy}^{(1)} = R_K/6$ $(n = 1)$ corresponding to the filling factors $\nu = 2$ and $\nu = 6$

respectively. In graphene $\nu = 2$ corresponds to the fully occupied zero-energy Landau level (n = 0) characterised by the largest separation $v\sqrt{2\hbar eB/c}$ from other Landau levels in the spectrum and hence the Hall resistance quantization is particularly robust. This plateau appeared in the field range of 9–12 T, depending on the carrier concentration (which was beyond the control in those experiments) and was accompanied by a vanishing $R_{xx}$. The $n = 1$ plateau, at $\nu = 6$, was not so flat, and $R_{xx}$ developed only a weak minimum. There was also a trace of a structure corresponding to $\nu = 10$. The observed sequence of Hall plateaux confirmed that the studied material was indeed monolayer graphene. At low magnetic fields Shubnikov-de Haas oscillations were observed as well as a weak localisation peak characteristic of the phase coherence of electrons in a disordered conductor.

The magneto-transport measurements on a much bigger, 160 $\mu$m × 35 $\mu$m Hall bar device are also presented in Fig. 3.3. A substantial positive magnetoresistance at low fields, which was absent in the smaller sample, indicated that the carrier concentration varied along the larger sample. Because of that, the $\nu = 6$ feature in $R_{xx}$ in the bigger sample was less prominent. Nevertheless, despite the inhomogeneity of the carrier density, the Hall resistance plateau at $R_{xy}^{(0)} = R_K/2$ ($n = 0$) was accompanied by vanishing longitudinal resistance $R_{xx}$. Importantly, the large-area device had a low resistance $R_c \approx 1.5$ $\Omega$ of contacts to the graphene layer and, as compared to smaller devices, could sustain a much higher current before QHE breaks down. Contacts made with Pd yielded even lower contact resistance down to 0.6 $\Omega$. Since larger breakdown current affords higher precision measurements in the QHE regime, the measurements were performed in the larger sample. The choice of the field, 14 T, where the most accurate measurements were performed was determined simply by the limitation of the superconducting magnet. This limit is below $B = 17.5$ T where the filling factor would be exactly $\nu = 2$ for this sample (with $n = 8.5 \cdot 10^{11}$ cm$^{-2}$ calculated from Shubnikov-de Haas oscillations).

The accuracy of the the Hall resistance quantization in graphene was established in measurements traceable to the GaAs quantum Hall resistance standard
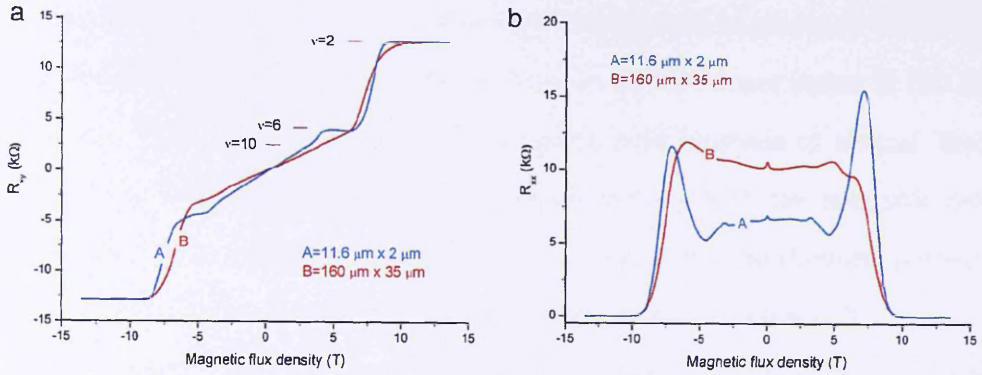
Figure 3.3: Transverse (a) and longitudinal (b) resistance of a small and a large device measured at $T = 4.2$ K with $1\mu$A current. Adapted from [58].

using a calibrated 100 $\Omega$ resistor. The optimal conditions at 300 mK were obtained for a source-drain current of 11.6 $\mu$A, 15% below the breakdown current established in the measurements of $R_{xx}$. The quantization accuracy $+0.4\pm3$ parts in $10^9$ inferred from the measurements was a four orders of magnitude improvement on the previous best result in exfoliated graphene. Graphene was still accurately quantized at 4.2 K, however, at this temperature the measurement current had to be reduced to 2.3 $\mu$A, which increased the uncertainty of the data accumulated over a comparable time interval.

The result readily put epitaxial graphene quantum Hall devices in the same league as their semiconductor counterparts. Note that it was obtained on a sample, although large by graphene standards, substantially smaller than the semiconductor devices used for calibration and without any optimisation. The precision measurements were made as far inside the resistance plateau as the magnet could reach, but still a long way from $\nu = 2$.

## 3.3 Quantum capacitance and filling factor pinning

Unlike the QHE in conventional 2D systems, where the carrier density is independent of magnetic field and the filling factor is determined by magnetic field,

here specifically to G/SiC, we find that the carrier density in graphene varies with magnetic field due to the charge transfer between surface donor states in SiC and graphene. Most importantly, we find magnetic field intervals of several Tesla, where the carrier density in graphene increases linearly with the magnetic field, resulting in the pinning of $\nu = 2$ state with electrons at the the chemical potential occupying SiC surface donor states half-way between the $N = 0$ and $N = 1$ LLs in graphene. Interestingly, at magnetic fields above the $\nu = 2$ filling factor pinning interval, the carrier density saturates at a value up to 30% higher than the zero-field carrier density. The pinned filling factor manifests itself in a continuously increasing breakdown current towards the upper magnetic field end of the $\nu = 2$ state far beyond the nominal value of $B_{\nu=2}$ calculated from the low-field carrier density. Facilitated by the high breakdown current in excess of 500 $\mu$A at 14 T a precision of 3 parts in $10^{10}$ have been achieved in the Hall resistance quantization measurements .

The anomalous pinning of $\nu = 4N + 2$ filling factors in G/SiC is determined by the dominance of the quantum capacitance [93] over the classical capacitance per unit area ($c_q \gg c_c$, where $c_q = e^2 \gamma_e$, $c_c = \varepsilon_0/d$ and $\gamma_e$ is the density of states of electrons at the Fermi level) in the charge transfer between graphene and surface donor states of G/SiC, that reside in the buffer layer of carbon atoms, just underneath graphene.

The quantum capacitance of a two-dimensional electron system is the result of a low compressibility of the electron liquid determined by the steps in $\gamma_e$. For electrons in high-mobility GaAs/AlGaAS heterostructures, it manifests itself in weak magneto-oscillations of the electron density [94, 95] which reflects the suppressed density of states inside the inter-Landau level gaps for the electrons in a magnetic field. A similarly weak effect has been observed in graphene exfoliated onto n-Si/SiO$_2$ substrate [96], where the influence of a larger (than in usual semiconductors) inter-LL gaps is hindered by a strong charging effect determined by a relatively large thickness of the SiO$_2$ layer. For epitaxial graphene on SiC,
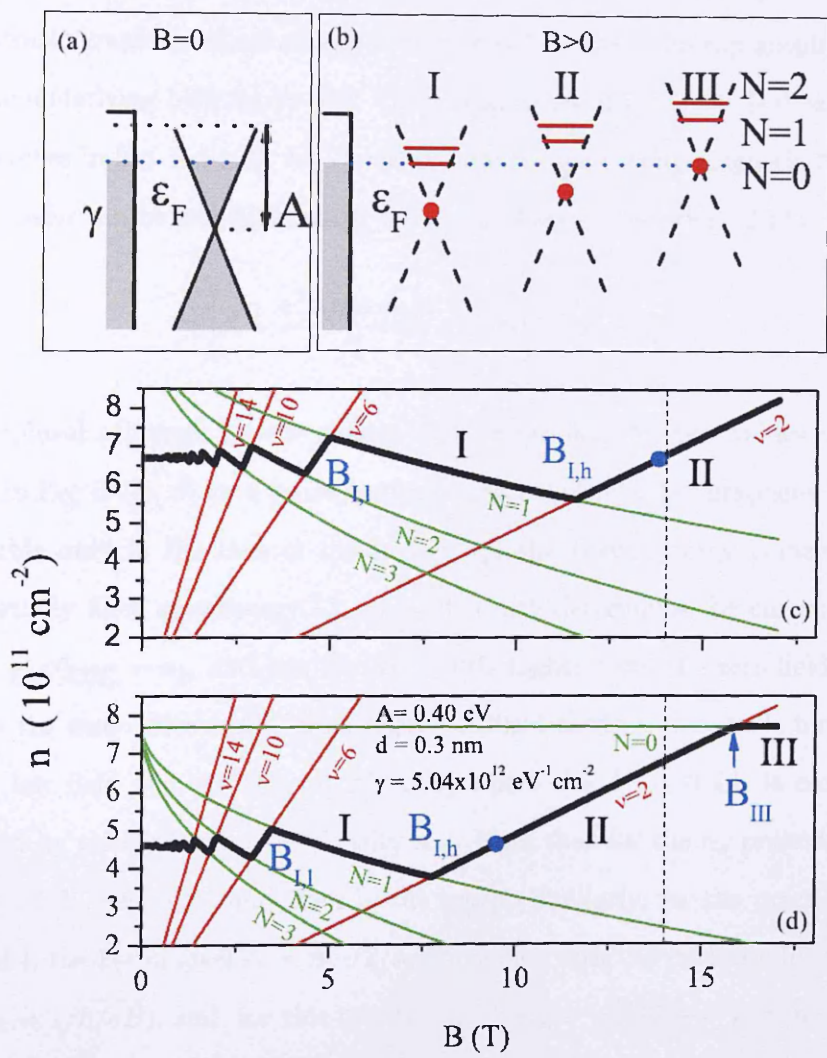
Figure 3.4: (a) Schematic band-structure for graphene on SiC in zero field; (b) The filling of LLs at different magnetic fields. Graphical solution for carrier density as a function of magnetic field, $n(B)$, of the charge-transfer model given by Eq. 3.5 (black line) together with lines of constant filling factor (red lines) and $n(B = \infty) - \gamma E(B, N)$ (green lines) for (c) $n_g = 5.36 \cdot 10^{11}$ cm$^{-2}$ and (d) $n_g = 8.11 \cdot 10^{11}$ cm$^{-2}$.

due to the short distance, $d \approx 0.3 - 0.4$ nm, between the buffer layer hosting the donors and graphene, the effect of quantum capacitance is much stronger, and the oscillations of the electron density take the form of the robust pinning of the electron filling factor. A similar behaviour was observed in STM spectroscopy of turbostratic graphite, where charge is transferred between the top graphene layer and the underlying bulk layers [97]. The charge transfer in G/SiC is illustrated in the sketches in Fig. 3.4(a,b), for $B = 0$ (a) and for quantizing magnetic fields (b). The transfer can be described using the charge balance equation (2.11)

$$\gamma \left[ A - \frac{e^2 d (n + n_g)}{\varepsilon_0} - \epsilon_F(n) \right] = n + n_g. \tag{3.5}$$

Graphical solutions for the charge transfer problem for two values of $n_g$ are shown in Fig. 3.4(c, d) for a broad range of magnetic fields. For graphene (interval III visible only in the case of the higher $n_g$) the Fermi energy coincides with the partially filled zero-energy LL, $\epsilon_F = 0$, which determines the carrier density $n_\infty = \frac{A}{1/\gamma + e^2 d/\varepsilon_0} - n_g$, and can be up to 30% higher than the zero-field density $n(0)$ in the same device [45]. This regime of fixed electron density is terminated at the low field end, at $B_{III} = \pi \hbar n_\infty / e$, where the $N = 0$ LL is completely occupied by electrons with the density $n_\infty$. Note that for the $n_g$ presented here, $B_{III} > 14$ T - the maximum field in the setup. Similarly, for the magnetic field interval I, the Fermi level $\epsilon_F = \hbar v \sqrt{2}/\lambda_B$ coincides with the partially filled $N = 1$ LL ($\lambda_B = \sqrt{\hbar/eB}$), and, for this interval, $n^I = n_\infty - \frac{\hbar v \sqrt{2}/\lambda_B}{1/\gamma + e^2 d/\varepsilon_0}$. The interval I is limited by the field values for which the $N = 1$ LL in the electron gas with the density $n^I$ is emptied at the higher field end,

$$B_{I,h} = \frac{h}{2e} \left[ \sqrt{n_\infty + \frac{\pi}{2} \frac{v^2 \hbar^2}{(1/\gamma + e^2 d/\varepsilon_0)^2}} - \sqrt{\frac{\pi}{2} \frac{v \hbar}{1/\gamma + e^2 d/\varepsilon_0}} \right]^2, \tag{3.6}$$

and is full at the lower end,

$$B_{I,l} = \frac{h}{6e} \left[ \sqrt{n_\infty + \frac{\pi}{6} \frac{v^2 \hbar^2}{(1/\gamma + e^2 d/\varepsilon_0)^2}} - \sqrt{\frac{\pi}{6}} \frac{v\hbar}{1/\gamma + e^2 d/\varepsilon_0} \right]^2 . \qquad (3.7)$$

In the magnetic field interval II the chemical potential in the system lies inside the gap between $N = 0$ and $N = 1$ LL in graphene. As a result, over this entire interval the $N = 0$ LL in graphene is full and $N = 1$ empty, so that the filling factor in graphene is fixed at the value $\nu = 2$, and the carrier density increases linearly with the magnetic field, $n = 2eB/h$, due to the charge transfer from the SiC surface.

According to Eq. (3.5), lowering the carrier density using an electrostatic gate is equivalent to effectively reducing the work function difference between graphene and donor states by $n_g(1/\gamma + e^2 d/\varepsilon_0)$, which shifts the range of the magnetic fields where the pinning of the $\nu = 2$ state takes place. For instance, reducing the zero-field carrier density from $n = 6.7 \cdot 10^{11}$ cm$^{-2}$ (Fig. 3.4(c)) to $n = 4.6 \cdot 10^{11}$ cm$^{-2}$ (Fig. 3.4(d)) moves the interval II from 11.5 T$< B_{II} <$ 21.6 T down to 7.7 T$< B_{II} <$ 15.9 T almost entirely within the experimental range.

## 3.4   Experimental study of filling factor pinning

In order to verify the predictions of the theory regarding the pinning of the $\nu = 2$ filling factor and to investigate the effect of the breakdown current on the precision of resistance measurements, the QHE was studied in a polymer-gated epitaxial graphene sample with Hall bar geometry of width $W = 35$ $\mu$m and length $L = 160$ $\mu$m. Graphene was grown at 2000 °C and 1 atm Ar gas pressure on the Si-terminated face of a semi-insulating 4H-SiC(0001) substrate. The as-grown sample had the low-field carrier density $n = 1.1 \cdot 10^{12}$ cm$^{-2}$. Graphene was encapsulated in a polymer bilayer, a spacer polymer followed by an active polymer able to generate acceptor levels under UV light. At room temperature electrons diffuse from graphene through the spacer polymer layer and fill the acceptor levels in

the top polymer layer. Such a photo-chemical gate allowed non-volatile control over the charge carrier density in graphene. More fabrication details can be found elsewhere [28, 46].

Fig. 3.5(a) shows magneto-transport measurements on the encapsulated sample tuned to a zero-field carrier density of $n = 6.7 \cdot 10^{11}$ cm$^{-2}$ - corresponding to the case in Fig. 3.4(c). From the carrier density we estimate that the magnetic field $B_{\nu=2}$ needed for reaching the exact filling factor $\nu = 2$ in this device is $\sim 13.8$ T. A well-quantized Hall plateau in $\rho_{xy}$ can be seen at $\nu = \pm 2$ for both magnetic field directions which is more than 5 T wide, whereas the longitudinal resistivity, $\rho_{xx}$, drops to zero signifying a non-dissipative state. In addition, a less precisely quantized plateau is present at $\nu = \pm 6$, for which $\rho_{xx}$ remains finite.

Accurate quantum Hall resistance measurements require that the longitudinal voltage remains zero (in practice, below the noise level of the nanovolt meter) to ensure the device is in the non-dissipative state, which can be violated by the breakdown of the QHE at high current. Fig. 3.5(b) shows the determination of the breakdown current $I_c$ at $B = 14$ T on the $\nu = 2$ plateau. Here we define $I_c$ as the source-drain current, $I_{sd}$, at which $V_{xx} \geq 10$ nV. We find for three different combinations of source-drain current contacts that the breakdown current for this value of $n$ is approximately 50 $\mu$A. The contact resistance, determined via a three-terminal measurement in the non-dissipative state, is smaller than 1.5 $\Omega$.

Fig. 3.5(c) shows a precision measurement of $\rho_{xy}$ and $\rho_{xx}$ for different magnetic fields along the $\nu = 2$ plateau. Note that this plateau appears much shorter in the magnetic field range than that shown in Fig. 3.4(a) because of the $\sim$200 times larger measurement current used in precision measurements. From this figure we determine that the mean of $\Delta\rho_{xy}/\rho_{xy}$ is $-0.06 \pm 0.3 \cdot 10^{-9}$ for the data between 11.75 and 14.0 T, while at the same time $\rho_{xx} < 1$ $m\Omega$. This result represents an order of magnitude improvement of QHE precision measurements in graphene, as compared to the earlier record [28]. Not only is QHE accurate, but it is also extremely robust in this epitaxial graphene device easily meeting the stringent
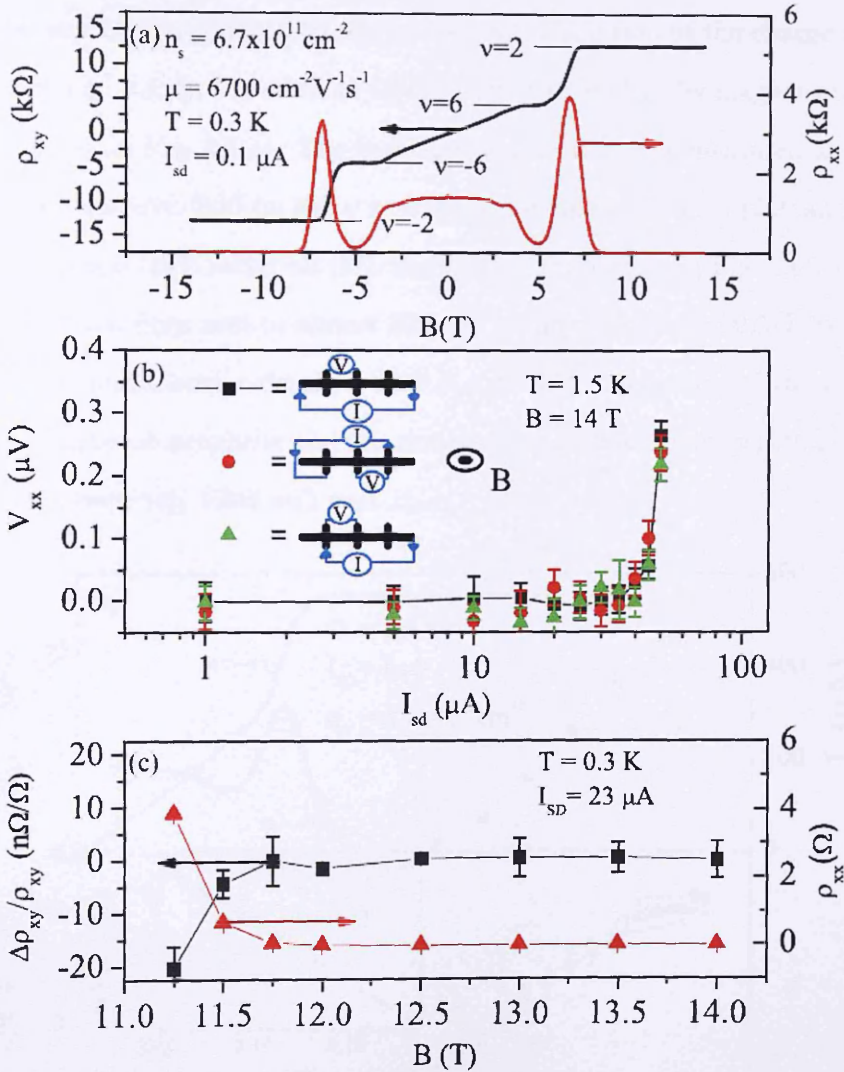
Figure 3.5: (a) Transverse ($\rho_{xy}$) and longitudinal ($\rho_{xx}$) resistivity measurement. The horizontal lines indicate the exact quantum Hall resistivity values for filling factors $\nu = \pm 2$ and $\pm 6$. (b) Determination of the breakdown current, $I_c$, for 3 different measurement configurations explained in legend. (c) High-precision measurement of $\rho_{xy}$ and $\rho_{xx}$ as a function of magnetic field. $\Delta\rho_{xy}/\rho_{xy}$ is defined as $(\rho_{xy}(B) - \rho_{xy}(14T))/\rho_{xy}(14T)$ and $\rho_{xy}(B)$ is measured relative to a 100 $\Omega$ standard resistor previously calibrated against a GaAs quantum Hall sample [28]. All error bars are $1\sigma$.

criteria for accurate quantum Hall resistance measurements normally applied to semiconductor systems.

Using the polymer gating method [46], the zero-field electron density in graphene was further reduced to correspond to the solution of the charge transfer problem in Fig. 3.4(d), i.e., down to $4.6 \cdot 10^{11}$ cm$^{-2}$ as evident by magnetotransport measurements in Fig. 3.6(a). The breakdown current $I_c$ was measured as a function of the magnetic field on the $\nu = 2$ quantum Hall resistance plateau. Unlike the conventional QHE materials [87], the breakdown current in Fig. 3.6(a) continuously increases from zero to almost 500 $\mu$A far beyond $B_{\nu=2} \sim 9.5$ T calculated from the zero-field carrier density. This is a direct consequence of the exchange of carriers between graphene and the donors in the buffer layer, which keeps the $N = 0$ LL completely filled well past $B_{\nu=2}$.
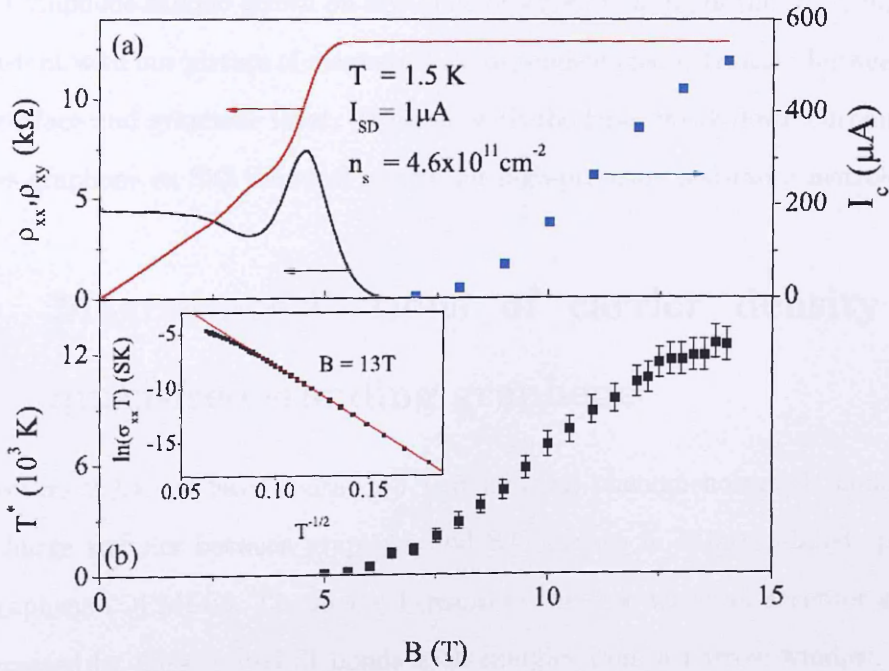


Figure 3.6: (a) Experimental $\rho_{xx}$ (black line) and $\rho_{xy}$ (red line) together with the measured break-down current, $I_c$ (blue squares). (b) Hopping temperature, $T^*$ as a function of magnetic field. Inset: $\ln(\sigma_{xx}T)$ versus $T^{-1/2}$ at 13 T. Red line is linear fit for $100 > T > 5$ K giving $T^* \approx 12000$ K.

The magnetic field range where the Fermi energy in G/SiC lies half-way between the $N = 0$ and 1 LLs determines the activation energy $\hbar\sqrt{1/2}v/\lambda_B \sim 1000$ K

(at $B \sim 30$ T) for the dissipative transport. For such a high activation energy, the low-temperature dissipative transport is most likely to proceed through the variable range hopping (VRH) between surface donors in SiC involving virtual occupancy of the LL states in graphene to which they are weakly coupled. Indeed, as shown in the inset of Fig. 3.6(b) the temperature dependence of the conductivity $\sigma_{xx}$ measured at $B = 13$ T obeys an $\exp(-\sqrt{T^*/T})$ dependence typical of the VRH mechanism. The $T^*$ values determined from the measurements at different magnetic fields are plotted in the main panel of Fig. 3.6(b). The breakdown current rising with field to very large values in Fig. 3.6(a) corresponds to $T^*$ reaching extremely large values up in excess of $10^4$ K - at least an order of magnitude larger than that observed in GaAs [98] and more recently in exfoliated graphene [89, 99].

Thus, we have studied the robust Hall resistance quantization in a large epitaxial graphene sample grown on SiC. The observed pinning of the $\nu = 2$ state is consistent with our picture of magnetic field dependent charge transfer between the SiC surface and graphene layer. Together with the large break-down current this makes graphene on SiC the ideal system for high-precision resistance metrology.

# 3.5 Magneto-oscillations of carrier density in quasi-free standing graphene

In section 2.2.4 we have considered two limiting phenomenological models of the charge transfer between graphene and SiC surface in H-intercalated epitaxial graphene (QFMLG). The model I describes the case when all acceptor states are created by unsaturated Si bonds with energies from a narrow window. The opposite limit of a wide acceptor energy distribution is covered by the model II. Here we analyse the carrier density dependence on a magnetic field in QFMLG, which as we show provides a way to distinguish experimentally between the two limiting doping models. We find that for the structures with a low acceptor density ($n_v \lesssim 10^{12}$ cm$^{-2}$, $\gamma_0 \lesssim 10^{13}$ cm$^{-2} \cdot$eV$^{-1}$) the magneto-oscillations of the hole

density in the model II result in a wide $\nu = 2$ quantum Hall effect (QHE) plateau, in contrast to the model I which shows no such oscillations[1] (Fig. 3.7). For the model I the carrier density $n$ does not depend on magnetic field (solid line), since all acceptor states are occupied (Fig. 3.7, inset D). On the contrary, the model II reveals magneto-oscillations (dashed line), occuring due to the charge transfer between graphene and acceptors as the Fermi level crosses the Landau levels (LL) (Fig. 3.7, insets A-C). The crucial feature of this dependence is the pinning of the $\nu = 2$ filling factor taking place over a magnetic field interval of several Tesla. The widening of the $\nu = 2$ QHE plateau has recently been observed in epitaxial graphene without any hydrogenation, where the charge transfer model similar to the model II was applied [64].

To evaluate the $n(B)$ dependence, such as shown in Fig. 3.7, we take into account the discreteness of the spectrum of Landau levels for relativistic charge carriers in graphene [100],

$$E_N = -\sqrt{2e\hbar v^2 B N}. \tag{3.8}$$

For a discrete electron spectrum in graphene, one can expect two thermodynamic regimes for the whole system including surface states:

a) The Fermi level is pinned to one of the Landau levels. In this case we solve Eq. (2.18) with $\epsilon_F = E_N$ to find the $n(B)$ dependence.

b) The Fermi level in the system lies in the acceptor band, between Landau levels. In this regime the carrier density is determined by the pinning of filling factor $\nu = nh/(eB) = 4N+2$, and Eq. (2.18) can be used to find the Fermi energy. These regimes are illustrated in the insets A-C in Fig. 3.7. At low magnetic fields $B < B_1$ (region A), where

$$B < B_1 = \frac{2A^2}{e\hbar v^2 \left(1 + \sqrt{1 + \frac{2A}{\pi \hbar^2 v^2}\left(\frac{1}{\gamma_0} + \frac{e^2 d}{\varepsilon_0}\right)}\right)^2}, \tag{3.9}$$

---

[1]For high acceptor densities ($n_v \gtrsim 10^{12}$ cm$^{-2}$, $\gamma_0 \gtrsim 10^{13}$ cm$^{-2}$·eV$^{-1}$), the expected pinning of the filling factor $\nu = 2$ can only be observed at difficultly accessible magnetic fields $B > 20$ T.

the Fermi level is pinned to the 1st LL $E_1$. At higher magnetic fields (region B),

$$B_1 < B < B_2 = \frac{hA}{2e\left(\frac{1}{\gamma_0} + \frac{e^2 d}{\varepsilon_0}\right)}, \tag{3.10}$$

the 1st LL becomes completely occupied and the Fermi level sticks to acceptor levels between the 0th and 1st LLs, providing the pinning of the filling factor $\nu = 2$. We also identify an extreme region C, corresponding to high magnetic fields $B > B_2$, where the carrier density remains constant, since the 0th LL is partially occupied and the Fermi level in graphene is pinned to the Dirac point energy.
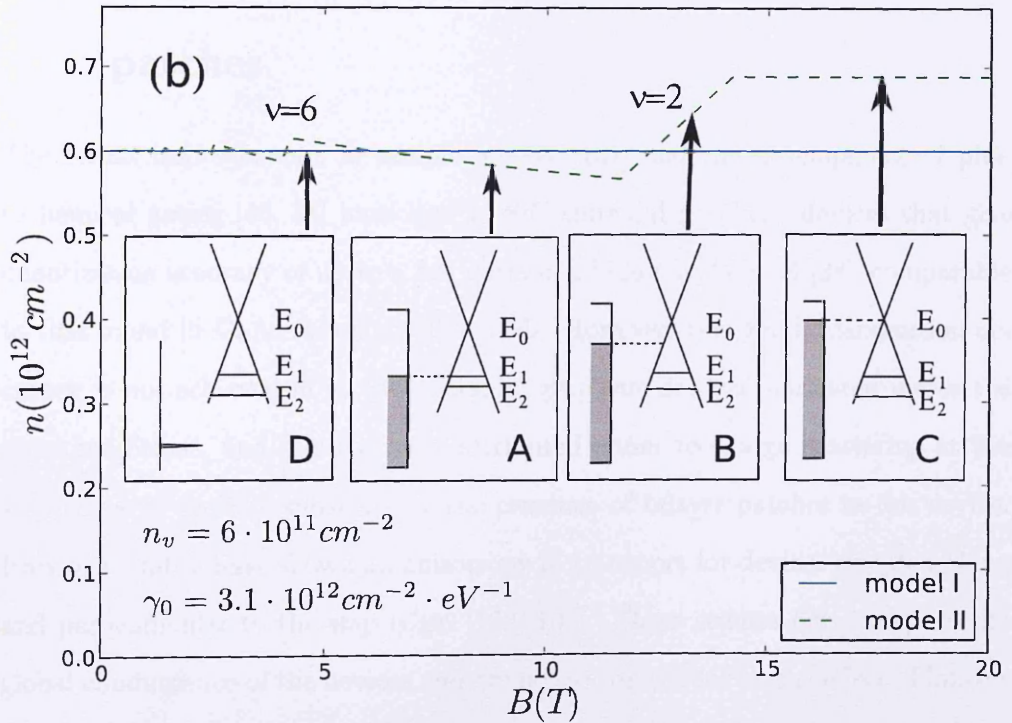


Figure 3.7: The magneto-oscillations of the hole density $n$ in QFMLG in the regimes of small acceptor density for both models. The energy structure in different regimes is shown in the insets A-C (model II) and inset D (model I). The parameters used here were chosen for illustration purposes only.

The magnetic field dependence of the carrier density in graphene in both models is very different, especially in structures with a low initial p-doping, $n \lesssim 10^{12}$ cm$^{-2}$. As shown in Fig. 3.7, the model II features a wide $\nu = 2$ QHE plateau, spread over

several Tesla of magnetic field, while the model I produces no $n(B)$ dependence. One of the ways to detect the pinning of filling factor $\nu = 2$ is to measure the activation energy $T_*$ and/or breakdown current of QHE [64]. The width of the peak in the dependence of $T_*$ and of the breakdown current on the magnetic field in the vicinity of $\nu = 2$ QHE plateau determines the region of filling factor pinning. Alternatively, one can determine the filling factor by looking at the Landau level occupancy using scanning tunneling spectroscopy as was done in a top graphene flake of a multilayer stack [97].

## 3.6 Quantum Hall transport in MLG with BLG patches

The recent improvements in sample quality [101] and the development of photochemical gating [46, 58] have lead to SiC epitaxial graphene devices that give quantization accuracy of up to a few parts in a billion at 300mK [28], comparable to that found in GaAs resistance standards. However, this good quantization accuracy is not achieved in all SiC epitaxial graphene devices fabricated under the same conditions, and this has been attributed either to charge scattering at the step edges of the SiC substrate or the presence of bilayer patches in the device. Previous studies have shown an anisotropy in transport for devices oriented along and perpendicular to the step edges [102, 103]. These studies only compare the global conductance of the devices and are not set up to look at the effect of bilayer inclusions in the device. Here we present a local study of SiC epitaxial graphene devices in the quantum Hall regime. A combination of Scanning Gate Microscopy (SGM), Kelvin Probe Microscopy (KPM) and global magnetoresistance measurements was used to link the effect of morphology, in particular, the presence of bilayer inclusions, on transport in the quantum Hall regime. Moreover, we focus on the behaviour of the bilayer inclusions under two different doping conditions.

This section is based on the work C. J. Chua, M. R. Connolly, A. Lartsev, R.

Pearce, S. Kopylov, R. Yakimova, V. I. Falko, S. Kubatkin, T. J. B. M. Janssen, A. Ya. Tzalenchuk, C. G. Smith, "Effect of local morphology on charge scattering in the quantum Hall regime on silicon carbide epitaxial graphene" (in preparation for publication).
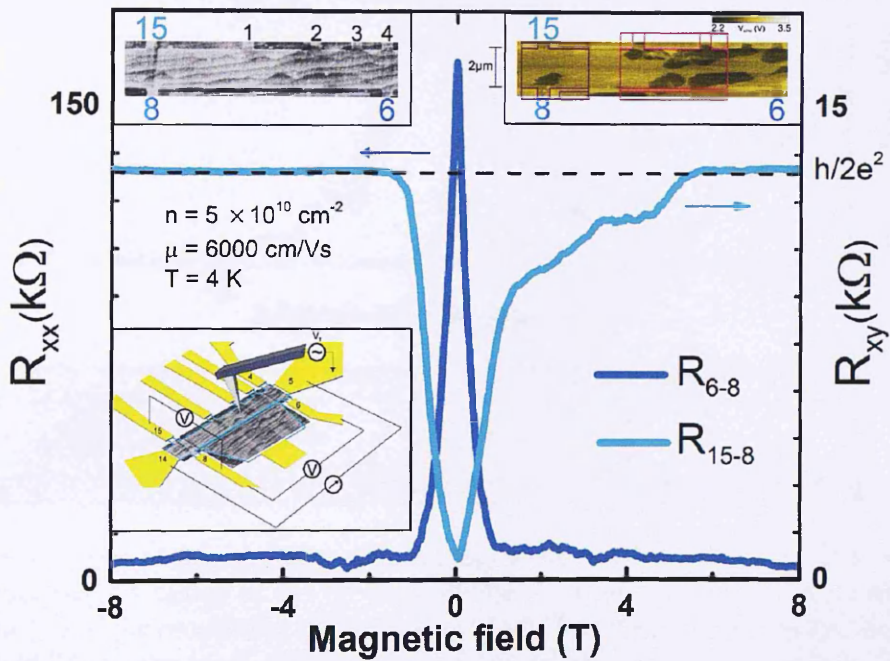


Figure 3.8: Magnetoresistance plot of the device shown in the atomic force microscopy image in the upper left inset with a gated carrier concentration of $n_1 = 5 \cdot 10^{10}$ cm$^{-2}$. The measurement set-up used is shown in the lower left inset. Upper right inset: Kelvin Probe Microscopy image of the device, showing regions of monolayer (light gray) and bilayer (dark gray) graphene. Regions scanned using SGM are also outlined and colour-coded with dark purple for the left side region, and light purple for the middle region.

Fig. 3.8 shows the magnetoresistance plot of the epitaxial graphene based device, shown in the top insets, with a low gated carrier concentration of $n_1 = 5 \cdot 10^{10}$ cm$^{-2}$ measured from the longitudinal contacts 8-6 and the transverse contacts 15-8 (see left inset atomic force microscope image). The magnetoresistance plot peaks around zero, indicating the presence of disorder in the system. The asymmetry of the transverse voltage with respect to magnetic field could be due
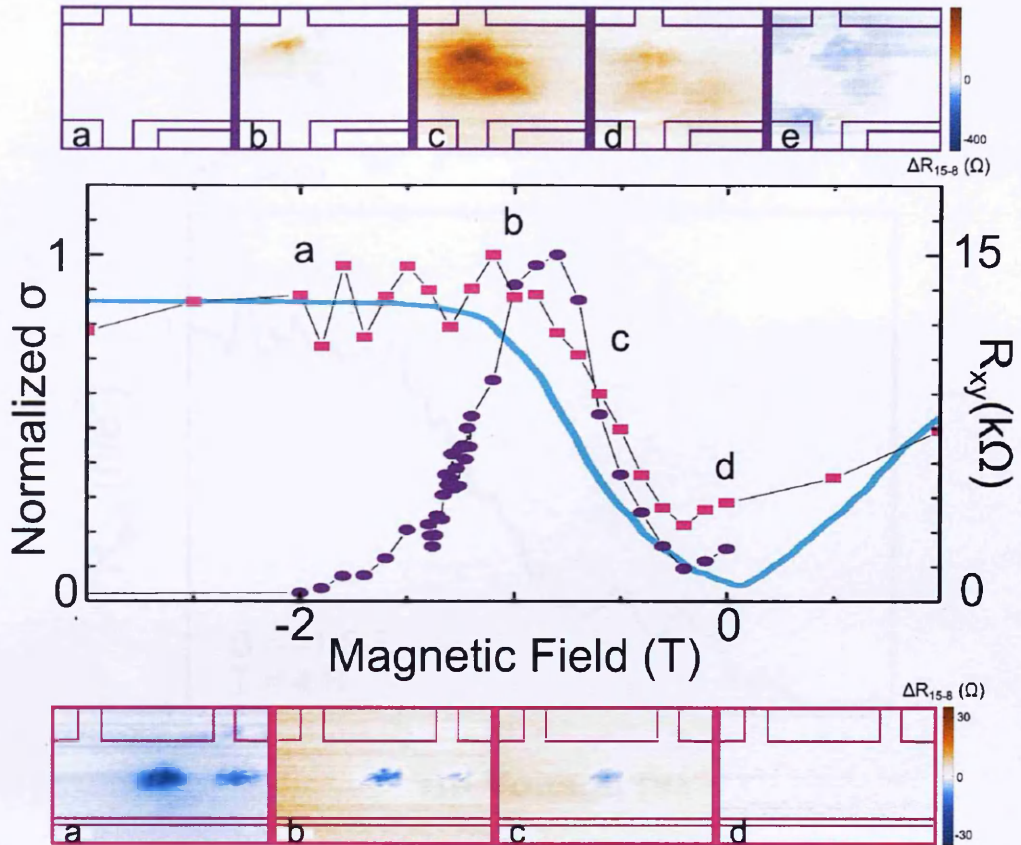
Figure 3.9: Top series: scanning gate images measured from contacts 15-8 while scanning the left region of the device. Middle: Plot of normalized standard deviation ($\sigma$) of the amplitude of fluctuation of all the pixels per image for the left region SGM images (dark purple plot) and the middle region SGM images (light purple plot). Bottom series: scanning gate images measured from contacts 15-8 while scanning the middle region of device.

to the proximity of some bilayers to the probing contacts. The $\nu = 2$ plateau is reached at approximately 1 Tesla, which suggests a low gated carrier concentration that can be extracted from the Hall voltage slope at low fields, and was found to be approximately $5 \cdot 10^{10}$ cm$^{-2}$. The corresponding zero field mobility is then found to be 6000 cm$^2$/V·s. It is observed that even deep in the $\nu = 2$ plateau, the longitudinal resistance does not drop to zero, which is indicative of backscattering of the edge states due to non-uniformity in the morphology of the device. The right inset shows the corresponding Kelvin Probe Microscopy image of the device, where light regions correspond to monolayer graphene and dark regions correspond to bilayer graphene. (Kelvin probe microscopy is a noncontact scanning method
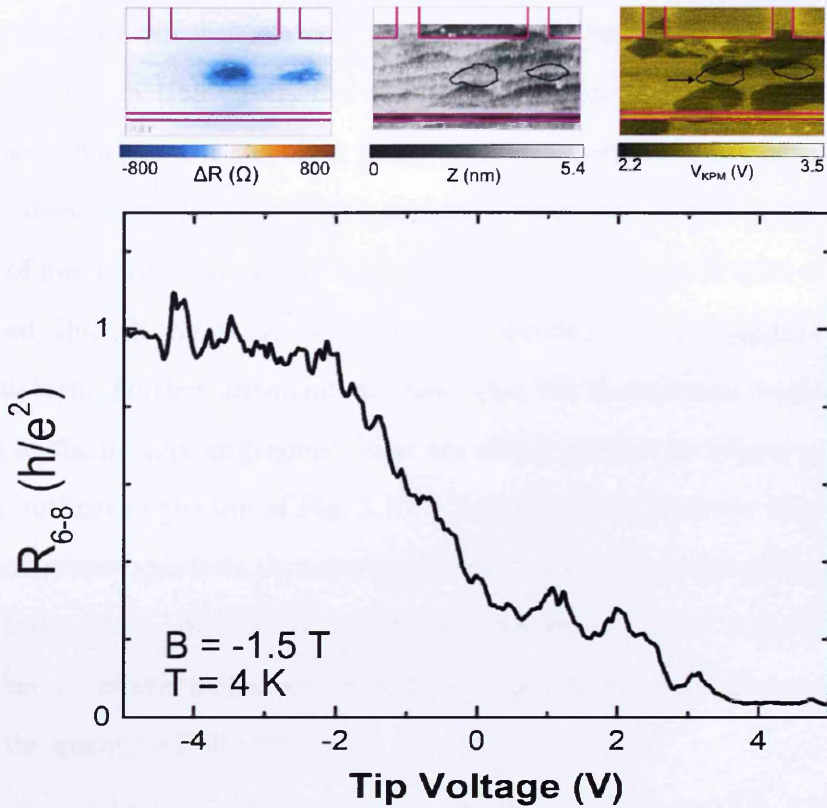
Figure 3.10: Top: Comparison of middle region of device SGM, AFM and KPM images, showing that regions of maximum response in the scanning gate images correspond to regions in the monolayer closely flanked by bilayer graphene. Bottom: Longitudinal resistance measured from contacts 6-8 as a function of tip voltage when sat above the monolayer constriction (see the narrow channel between the dark bilayer patches in the top right inset).

which allows to build a map of surface work function by measuring the oscillations of the tip.) Scanning gate images were taken from two main regions: the left hand side region, where there is mostly monolayer graphene, and the middle region of the device where bilayer graphene is predominant. (Scanning gate microscopy is a technique for measuring the effect of tip position and potential on the resistance of the sample.)

The top series of Scanning gate microscope images (see Fig. 3.9) were taken at varying magnetic fields and measured from contacts 15-8 while scanning the left-hand side region of the device with an AC tip voltage of 2 V. It is observed that the highest scanning gate response occurs at around $-0.8$ T, on the rise before the

$\nu = 2$ plateau, which is consistent with a non-interacting, single-particle picture of the quantum Hall effect, and is expected for the high source-drain bias used for these images. On the other hand, for scans performed at the middle region of the device with multiple bilayer inclusions (outlined in light purple) the amplitude of fluctuations was found to increase with magnetic field until a plateau was reached, then the amplitude was nearly independent of magnetic field throughout the plateau. Further investigation shows that the fluctuations originate from regions in the monolayer graphene that are closely flanked by bilayer graphene (see black outlines in the top of Fig. 3.10). The interaction between bilayer graphene and monolayer graphene then determines the behaviour of edge states in the quantum Hall regime. In order to understand this interaction, it is useful to identify whether the bilayer inclusions are metallic or insulating when the rest of the device is in the quantum Hall regime.

For the device with the low gated carrier concentration (see Fig. 3.8) the bilayer inclusions are in the insulating state, because sweeping the tip voltage above the narrow constriction formed by the bilayer inclusions leads to significant gating of the carrier concentration in the constriction. Fig. 3.10 shows the longitudinal resistance measured from contacts 6-8 as a function of tip voltage as the tip is sat above the monolayer constriction outlined and indicated by an arrow in Fig. 3.10 top. We find that as the tip bias is swept from positive bias to negative bias, we are able to tune the longitudinal resistance from nearly zero to almost exactly $h/e^2$. This suggests that at high positive bias, we are able to tune the carrier concentration of the spot $n_1'$ to nearly equal to $n_1$, so that scattering of edge states is suppressed when both areas are on the $\nu = 2$ plateau. On the other hand, a resistance value of $h/e^2$ indicates that we are measuring the longitudinal resistance along a series of n-p-n Hall bars. This suggests that at high negative tip bias, we are able to gate the monolayer constriction to p-type with a carrier concentration such that it reaches the $\nu = -2$ plateau at $-1.5$ T. The fact that we are able to gate the monolayer graphene suggests that this region must consist of a narrow

constriction of graphene flanked by insulting bilayer inclusions. By varying the tip bias, we are able to change the carrier concentration in the narrow constriction such that for a given magnetic field, the area under the spot can be brought in and out of the quantum Hall regime, and thus tuning the transmission of edge states/current through the narrow monolayer graphene constriction.

For the case where the gated carrier concentration is high, such as that found for the device shown in Fig. 3.11(a), which oriented perpendicular to the step edges, with a bilayer patch running directly across the device, the magnetoresistance plot in Fig. 3.11(b) shows a quantized Hall resistance (red plot) and a corresponding zero longitudinal resistance (green plot) for the same device measured between monolayer graphene. However, when measured across the bilayer patch, the quantum Hall effect is not observed due to shunting of the edge channels by the metallic bilayer patch. Instead of observing zeroes in the longitudinal resistance for high fields (blue plot), a value close to the quantized Hall resistance is measured.

Here we perform the electrostatic modelling of the behaviour of bilayer inclusions on SiC epitaxial graphene samples using the charge transfer model Eq. (2.11) and found a good agreement with the experimental data for different gated carrier concentrations. Given the ungated monolayer carrier concentration $n_0$ we can determine the density of surface donor states $\gamma$ and thus the carrier concentration $n$ in graphene. The filling factor pinning for both monolayer and bilayer graphene, shown in Fig. 3.12, happens in the following ranges of Fermi energy:

$$E_1 < \epsilon_F^{MLG}(\nu = 2) < E_2, \tag{3.11}$$

$$-\Delta/2 < \epsilon_F^{BLG}(\nu = 0) < \Delta/2, \tag{3.12}$$

$$\Delta/2 < \epsilon_F^{BLG}(\nu = 4) < \sqrt{2}\hbar\omega_c, \tag{3.13}$$

where $\Delta$ is the gap in the bilayer spectrum, determined self-consistently [15]. It is evident that filling factor pinning for monolayer graphene and bilayer graphene at a given gated carrier concentration do not overlap at any magnetic field at high

gated carrier concentration. However, at low carrier concentrations, calculations show that a gap opens for bilayer graphene with the gap size dependent on $n_0$. For the low gated carrier concentration ($n_1 = 5 \cdot 10^{10}$ cm$^{-2}$) found in the device in Fig. 3.8, an initial carrier concentration of $n_0 = 3 \cdot 10^{12}$ cm$^{-2}$ implies that the bilayer inclusions are within the insulating, gapped regime, while the monolayer graphene is in the quantum Hall regime. In contrast, for samples with a higher gated concentration $n_1$, such as that shown in Fig. 3.11, for magnetic fields where monolayer graphene is in the quantum Hall regime, the bilayer inclusions are in the metallic regime.

To further investigate the effect of the magnetic field on the scanning gate response, we examine the model in Fig. 3.12 for varying tip gated carrier concentration $n_1'$ with respect to the gated carrier concentration of the whole device $n_1$. For a fixed magnetic field $B^*$ (see Fig. 3.13), we find that as the local carrier concentration ($n_1'$) of the monolayer constriction underneath the tip is gradually increased towards $n_1$ for positive tip bias, eventually $n_1' = n_1$, such that the whole device is on the $\nu = 2$ plateau and backscattering is suppressed. The observed increase in scanning gate response with increasing magnetic field (see Fig. 3.9) can also be explained in terms of this phase diagram. If we now consider a situation where $n_1' < n_1$ as shown in Fig. 3.13, for a fixed magnetic field $B^*$, the area under the tip is just outside the $\nu = 2$ plateau while the rest of the device is in the quantum Hall regime, such that in this scenario, we expect to see some scanning gate response at the constriction. As we increase the magnetic field to $B'^*$ while keeping $n_1'$ constant, we then expect the scanning gate response at the constriction to also gradually increase because the area under the tip is being brought farther away from the $\nu = 2$ filling factor, while for this magnetic field range ($B'^*$ to $B^*$), the rest of the device remains on the $\nu = 2$ plateau.

In the following we analyse the transport properties of the device shown in top right inset of Fig. 3.8 between different contacts in quantum Hall regime, assuming the bilayer patches are in the insulating regime. In that case a narrow channel

of MLG in the center of the device determines the longitudinal resistance of the device. By varying the voltage of the tip placed above the pinch point we create a junction of graphene areas with different carrier densities and filling factors.

First we consider a n-p-n junction with filling factors $\nu$ and $-\nu'$ (Fig. 3.14). The edge currents within each area are characterized by a number of current channels $\nu/\nu'$. These currents mix up at p-n junctions and equilibrate, changing chemical potentials of current channels and contact potentials. The continuity of the electric current dictates

$$I = \frac{\nu e^2}{h}(V_1 - V_3) = \frac{\nu' e^2}{h}(V_3 - V_2) = \frac{\nu e^2}{h}(V_2 - V_4), \qquad (3.14)$$

and can be used to establish a relation between transverse, source-drain and longitudinal voltages:

$$V_{tr} = V_3 - V_1 = V_4 - V_2, \qquad (3.15)$$

$$V_{sd} = V_4 - V_1 = \frac{\nu + 2\nu'}{\nu'}V_{tr}, \qquad (3.16)$$

$$V_l = V_2 - V_1 = V_4 - V_3 = \frac{\nu + \nu'}{\nu'}V_{tr}. \qquad (3.17)$$

Using the transverse resistance $R_{tr} = R_{13} = h/(\nu e^2)$ we finally get the longitudinal and net resistance of n-p-n:

$$R_l^{(npn)} = R_{34} = \frac{\nu + \nu'}{\nu\nu'}\frac{h}{e^2}, \qquad R_{sd}^{(npn)} = R_{14} = \frac{\nu + 2\nu'}{\nu\nu'}\frac{h}{e^2}. \qquad (3.18)$$

A similar calculation for n-n-n juction gives

$$R_l^{(nnn)} = R_{34} = \frac{|\nu - \nu'|}{\nu\nu'}\frac{h}{e^2}, \qquad R_{sd}^{(nnn)} = R_{14} = \begin{cases} \frac{2\nu'-\nu}{\nu\nu'}\frac{h}{e^2}, & \nu' \geq \nu; \\ \frac{h}{\nu'e^2}, & \nu' < \nu. \end{cases} \qquad (3.19)$$

These results for n-p(n)-n junction are consistent with the previous work [104] and can be a good approximation for the contact resistances of the whole device. Applying this analysis to the data in Fig. 3.10 we can conclude that the device

operates in the n-p-n regime with $\nu = -\nu' = 2$ and $R_{6-8} = R_{34} = h/e^2$ at tip voltages $< -2$ V, and in the n-n-n regime with $\nu = \nu' = 2$ and $R_{6-8} = 0$ at tip voltages $> 3$ V.

In conclusion, we have demonstrated the important role that bilayer inclusions play on electron transport in a magnetic field. The effect of bilayer inclusions depend on their position within the device, as well as the initial and gated carrier concentration of the graphene sample. For high gated carrier concentration in graphene, bilayer inclusions running across the device, perpendicular to the direction of transport, are in the metallic regime and shunt the quantum Hall edge states. In contrast, for low gated carrier concentrations the bilayer inclusions behave as insulating regions that, when positioned accordingly, create a gateable narrow channel where electron transmission can be tuned while under an applied magnetic field. This behaviour is in agreement with the electrostatic modelling based on a charge transfer model between mono/bilayer graphene and the SiC substrate. In this way, we are able to gate the narrow region all the way from p-type to n-type such that on the the one hand an n-p-n junction is formed in the device and the resistance reads nearly $h/e^2$, and on the other hand the perfect transmission of edge states in the quantum Hall regime is nearly recovered. We conclude that it is best to minimize bilayer inclusion density in devices meant for quantum Hall resistance standards. On the other hand, the presence of bilayer inclusions in SiC epitaxial graphene samples make it an interesting system to study in terms of electron quantum optics.
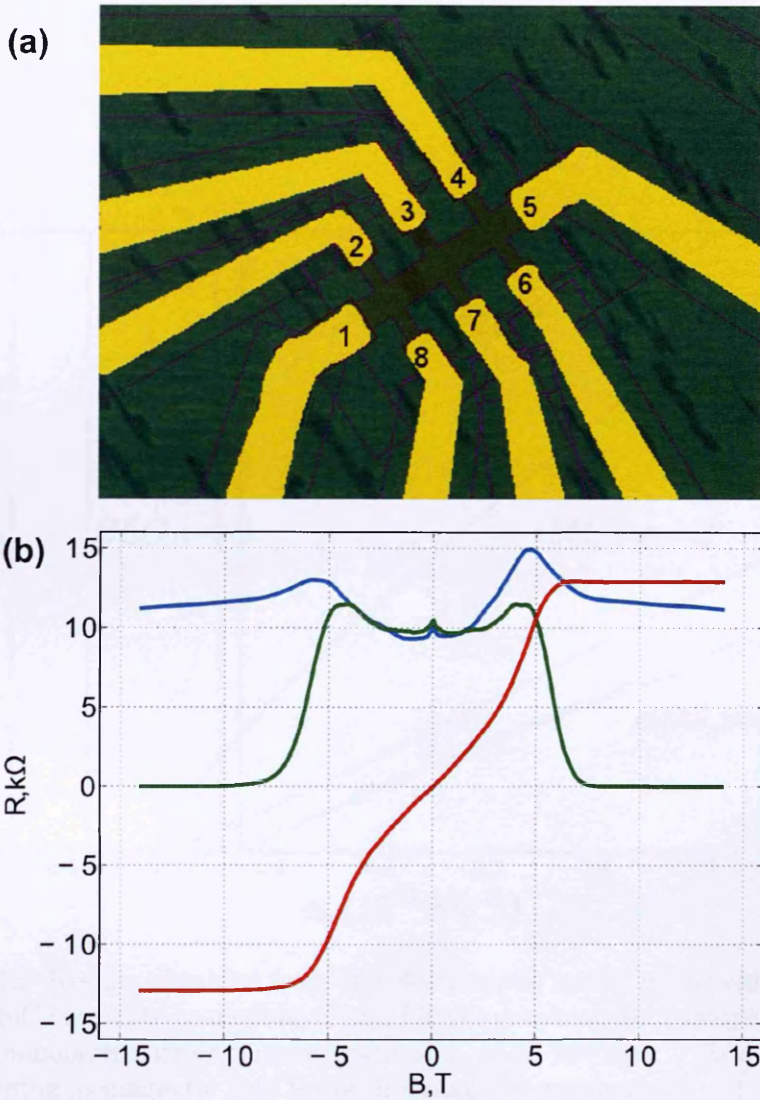
Figure 3.11: a) Optical micrograph of a SiC epitaxial graphene device with gated carrier concentration of $n_1 = 10^{11} \text{cm}^{-2}$. b) The corresponding transverse resistance (red) and longitudinal resistance (green) plots measured from contacts 4-6 and 6-7, respectively. The blue plot, measured from contacts 8-7, shows shunting of the Hall resistance in the measured longitudinal resistance.
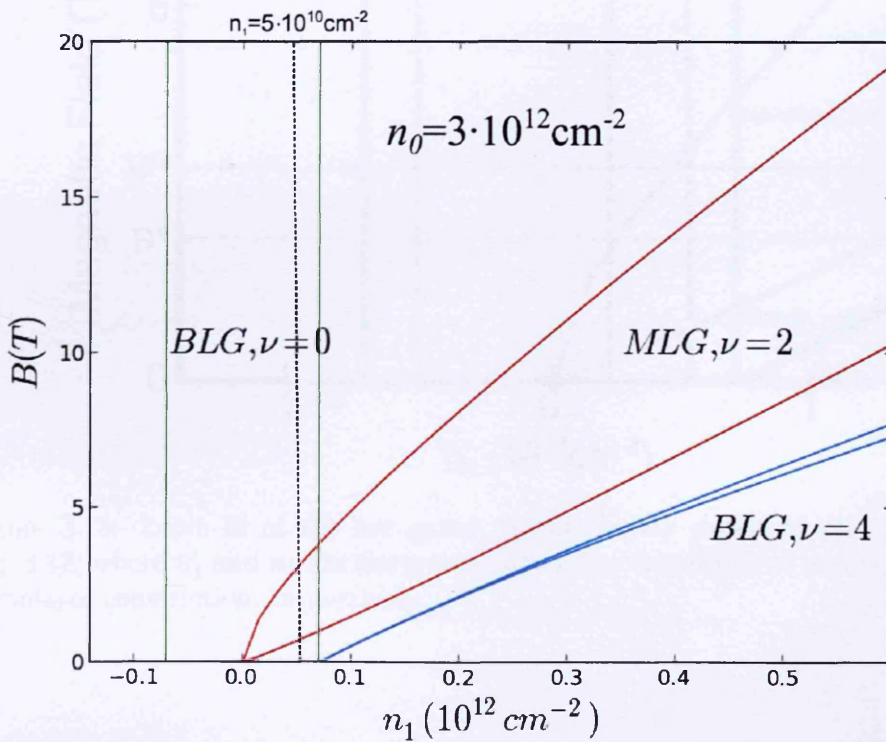
Figure 3.12: Results obtained from the electrostatic model of the charge transfer from the SiC substrate to monolayer and bilayer graphene for a sample with initial ungated monolayer carrier concentration of $n_0 = 3 \cdot 10^{12}$ cm$^{-2}$. Regions of filling factor pinning in magnetic field for both monolayer graphene ($\nu = 2$, between red lines) and bilayer graphene ($\nu = 4$, between blue lines and $\nu = 0$, between green lines) have been plotted as a function of the gated concentration $n_1$.
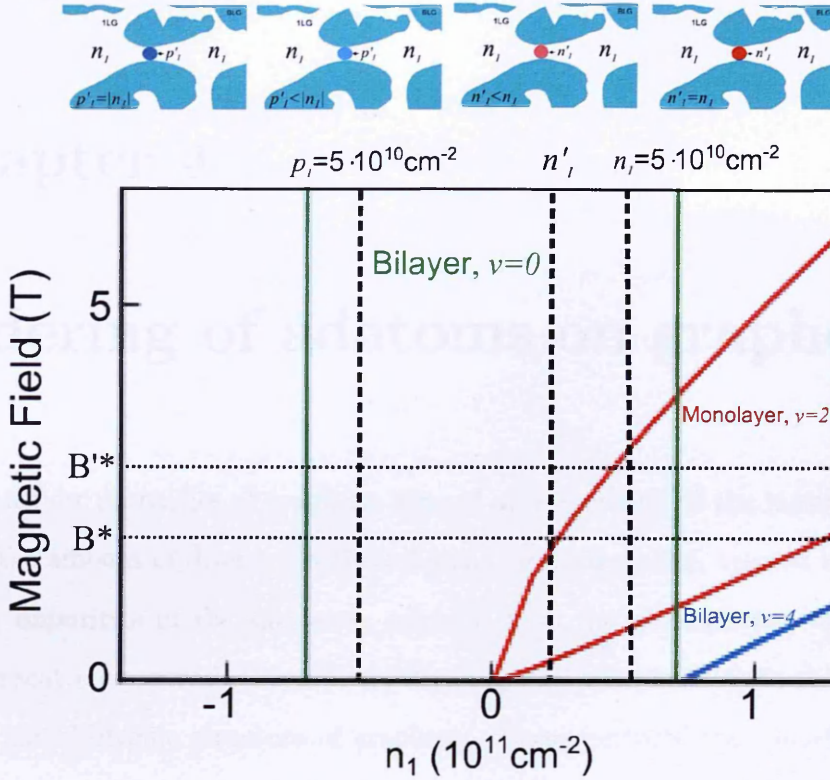
Figure 3.13: Zoom in of the low gated carrier density region of plot shown in Fig. 3.12, where $n_1'$ and $n_1$ are the gated carrier concentrations at and outside the monolayer constriction, respectively.
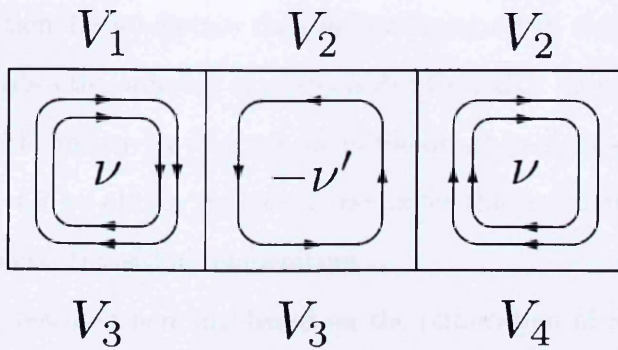


Figure 3.14: The edge currents in graphene p-n-p junction.

# Chapter 4

# Ordering of adatoms on graphene

The transport properties of graphene depend on the quality of the material itself and of the amount of disorder in the surrounding environment, created by lattice defects, impurities in the substrate, adatoms from the atmosphere, etc. These electron scatterers introduce symmetry-breaking perturbations into the lattice and modify the electronic structure of graphene. These perturbations interfere with each other creating an interaction between adatoms which can order them in a particular pattern. In this chapter we investigate the effect of ordered adatoms on the electronic structure and transport properties of mechanically exfoliated graphene on $SiO_2$ substrate.

In section 4.1 we overview the different types of disorder and present the framework for describing the interaction between electrons in graphene and alkali adatoms. In section 4.2 we discuss the electron transport in disordered graphene. Section 4.3 describes the ordering of adatoms due to RKKY interaction. In section 4.4 we calculate the resistivity of graphene in the presence of ordered adatoms. Finally, in section 4.5 we obtain analytical results for the resistivity in a very close vicinity of the phase transition temperature.

The results presented here are based on the publication of S. Kopylov, *et al.* [105].

# 4.1 Disordered graphene and symmetry breaking by adatoms

Even though the strong sigma-bonds between carbon atoms in graphene sustain a high quality of the honeycomb lattice, the electronic properties of graphene are affected by intrinsic and extrinsic disorder. Intrinsic disorder comes from surface ripples [106] and topological defects [107]. Extrinsic disorder stems from different sources: adatoms [108], substrate impurities [109], vacancies [110], edges [111]. These types of disorder can be categorized into two groups: long-range and short-range disorder. Surface ripples and charged substrate impurities are examples of a long-range disorder, which usually create an electron potential perturbation with a power law dependence $V \propto r^{-\alpha}$ and is insensitive to the location of the impurity within the unit cell. In contrast, the effect of short-range disorder is localized to a few carbon atoms around the impurity and is sensitive to its location within the unit cell. Here we only consider the short-range disorder created by adatoms on the surface of graphene.

Controlling the atmosphere around the graphene sample allows different types of adsorbent atoms to reside on graphene. The interaction between electrons in graphene and adatoms depends on the location of the latter within the unit cell. Alkali atoms reside over the centers of hexagons [112]. Oxygen, nitrogen and boron (e-type) adatoms are positioned in the middle of carbon-carbon bonds [113]. Halogens and atomic hydrogen (s-type) are attached on top of carbon atoms [114]. The electron potential created by these adatoms has a non-trivial structure in the valley $(KK')$ and sublattice $(AB)$ spaces:

$$\hat{V}(\mathbf{r}) = \hbar v a \sum_l \hat{W}_l \delta(\mathbf{r} - \mathbf{r}_l), \tag{4.1}$$

where $a$ is the length of a C-C bond, $\mathbf{r}_l$ are the coordinates of adatoms and $\hat{W}_l$ are $4 \times 4$ matrices in the $[\psi_{K,A}, \psi_{K,B}, \psi_{K',B}, \psi_{K',A}]$ basis.

For example, for e-type adatoms residing over the middle of C-C bonds, the matrix $\hat{W}_l$ has the following structure [108]:

$$\hat{W}_l = \lambda_{A_1} + \lambda_{E_1'}\Sigma_z(\mathbf{\Lambda} \cdot \mathbf{u}_l) + \lambda_{E_2}\Lambda_z(\mathbf{\Sigma} \cdot \mathbf{v}_l) + \lambda_G(\mathbf{\Lambda} \times \mathbf{u}_l)(\mathbf{\Sigma} \times \mathbf{v}_l), \qquad (4.2)$$

where $\mathbf{u}_l = (\cos(2\pi m_l/3), \sin(2\pi m_l/3))$ and $\mathbf{v}_l = (\cos(2\pi n_l/3), \sin(2\pi n_l/3))$ are unit vectors $(m_l, n_l = -1, 0, 1)$. $\lambda_{A_1}$, $\lambda_{E_1'}$, $\lambda_{E_2}$, $\lambda_G$ are the amplitudes of the potential contributions with different symmetries. Here we use the set of $4 \times 4$ "sublattice" and "valley" matrices $\Sigma_{x,y,z}$ and $\Lambda_{x,y,z}$ [115, 116, 118]

$$\Sigma_x = \Pi_z \otimes \sigma_x, \quad \Sigma_y = \Pi_z \otimes \sigma_y, \quad \Sigma_z = \Pi_0 \otimes \sigma_z, \qquad (4.3)$$

$$\Lambda_x = \Pi_x \otimes \sigma_z, \quad \Lambda_y = \Pi_y \otimes \sigma_z, \quad \Lambda_z = \Pi_z \otimes \sigma_0,$$

where $\sigma_i$ and $\Pi_j$ are Pauli matrices in the sublattice (AB) and valley $(KK')$ spaces. All operators $\Sigma_i$ and $\Lambda_j$ change signs upon time inversion, therefore the products $\Sigma_i \Lambda_j$ and the potential $\hat{V}$ are time-reversal.

In the following analysis we investigate the case of adatoms residing over the centers of hexagons. The Hamiltonian describing graphene covered by this type of adatoms has the form [115, 116, 117]

$$\hat{H} = \hbar v(\mathbf{p}\mathbf{\Sigma}) + \hat{U}(\mathbf{r}) + \hat{V}(\mathbf{r}); \qquad (4.4)$$

$$\hat{U} = \sum_l \hat{I}w(\mathbf{r} - \mathbf{r}_l); \quad \hat{V} = \hbar\lambda va\sum_l(\mathbf{u}_l\mathbf{\Pi})\delta(\mathbf{r} - \mathbf{r}_l).$$

The $\hat{U}$-term does not violate the AB sublattice symmetry and scatters electrons without changing their valley state. The electron-adatom interaction $\hat{V}$, whose form [108, 117, 118] is prescribed by the highly symmetric position of adatoms at the centers of hexagons, is responsible for the intervalley scattering of electrons. We assume that the dimensionless impurity potential $\lambda$ is small $(\lambda \lesssim 1)$ and will treat the electron-adatom interaction perturbatively.

## 4.2 Transport properties of graphene

The high mobility and effective control of exfoliated graphene conductivity using an external gate has made it a promising material for use in electronic devices. Fig. 4.1 demonstrates how the conductivity of monolayer graphene varies with the gate voltage. This behaviour has two interesting properties.

The first property is the linear dependence of the conductivity on the gate voltage (or carrier density). This goes in contradiction with the semiclassical Boltzmann transport theory for graphene covered with short-range scatterers, which predicts a conductivity independent of the carrier density [119]. According to this theory the conductivity of graphene is [120]

$$\sigma = \frac{e^2 v^2}{2} D(\epsilon_F)\tau(\epsilon_F), \tag{4.5}$$

where $D(\epsilon) = 2\epsilon/(\pi\hbar^2 v^2)$ is the density of states in graphene and the transport scattering time is given by

$$\frac{1}{\tau(\epsilon_{\mathbf{p}})} = \frac{2\pi n_i}{\hbar} \int \frac{d^2\mathbf{p}'}{(2\pi)^2} \overline{|V_{\mathbf{pp}'}|^2}(1 - \cos\varphi_{\mathbf{pp}'})\delta(\epsilon_{\mathbf{p}} - \epsilon_{\mathbf{p}'}), \tag{4.6}$$

where $n_i$ is the concentration of impurities, $\varphi_{\mathbf{pp}'}$ is the angle between the wavevectors $\mathbf{p}$ and $\mathbf{p}'$, $V_{\mathbf{pp}'}$ is the matrix element of disorder potential and $\overline{\phantom{x}}$ stands for disorder averaging. Applied to short-range disorder Eq. (4.5) gives a result independent of the Fermi energy and thus the carrier density. This contradiction was solved by attributing the source of electron scattering to the long-range Coulomb disorder in the substrate [109], which gives a dependence $\sigma(\epsilon_F)$ consistent with experiments.

Another unusual property is the finite minimal conductivity of undoped graphene. Originally this effect was considered to be an intrinsic property of graphene and a number of theoretical approaches were used to obtain the value of minimal conductivity yielding different results $\sim e^2/h$ [121, 122, 123, 124].

The problem is that the intrinsic minimal conductivity of an undoped MLG is an ill-defined property, which, being a limit of the conductivity $\sigma(T, \omega, \epsilon_F, L^{-1})$ at $T, \omega, \epsilon_F, L^{-1} \to 0$, depends on the order at which these limits are taken [120]. The actual minimal conductivity observed in experiments is a result of a highly inhomogeneous carrier density landscape broken up into electron-hole puddles [125]. This model was investigated in [126] using the random-phase approximation (RPA) and is consistent with experimental results.

In the following sections we apply the Boltzmann transport theory to calculate the conductivity of graphene covered with alkali adatoms ordered due to RKKY interactions.
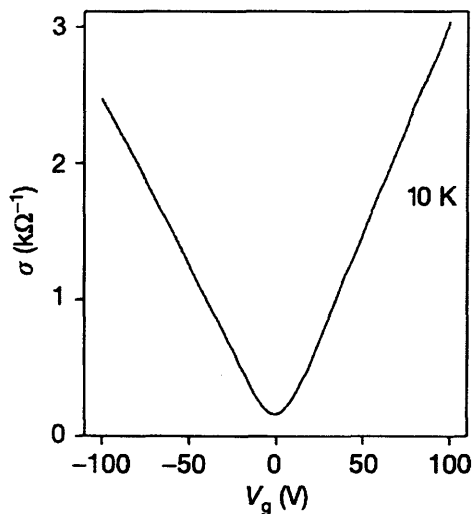


Figure 4.1: Dependence of the conductivity of exfoliated graphene on gate voltage $V_g$. Adapted from [3].

## 4.3  RKKY interaction of adatoms in graphene and adatoms sublattice ordering

Impurities in metals experience a long-range RKKY interaction due to the polarization of the electron Fermi sea (Friedel oscillations) [127]. For surface adsorbents such an interaction may result in their structural ordering, repeating the pattern

of the Friedel oscillations of the electron density [118, 128, 129, 130]. In particular, a dilute ensemble of adatoms on graphene may undergo a partial ordering transition [108, 117, 131, 132]. Unlike other materials, the RKKY interaction between adatoms on graphene exists even at zero carrier density, with a characteristic long-range $1/r^3$ dependence, and it exhibits Friedel oscillations, which are commensurate with the underlying honeycomb lattice.

The intervalley scattering of the electrons by adatoms residing above the centers of the honeycombs $\hat{V}$ (4.4) leads to Friedel oscillations that resemble a $\sqrt{3} \times \sqrt{3}$ charge-density wave superlattice. The positions of each individual adatom relative to such a superlattice can be characterized by one of three vectors, $\mathbf{u} = (\cos \frac{2\pi m}{3}, \sin \frac{2\pi m}{3})$, with $m = -1, 0, 1$. In the undoped graphene ($\epsilon_F = 0$) the interaction between adatoms has a long-range sign-changing behaviour $-\mathbf{u}_j \cdot \mathbf{u}_l / r_{jl}^3$. To minimize the interaction energy adatoms have to take the equivalent positions within the $\sqrt{3} \times \sqrt{3}$ superlattice unit cells, i.e. have the same "spin" values $\mathbf{u}$. This is illustrated in Fig. 4.2, which shows the hidden "Kekulé mosaic" ordering characterized by adatoms occupying the hexagons of the same color. The transition of an ensemble of adatoms into this Kekulé ordered state [117] falls in the symmetry class of 3-state Potts models with a long-range interaction [133].

A Monte Carlo simulation of the corresponding $1/r^3$ random-bond Potts model [117] has revealed the ordered phase below the transition temperature $T_c \approx 0.6\lambda^2 (n_i a^2)^{3/2} \hbar v / a$, where $n_i$ is the concentration of adatoms. Here we assume that the electron concentration $n = 4\pi / \lambda_F^2$ is not high, $n \ll n_i$, but the electron Fermi wavelength is shorter than its mean free path, $\lambda_F \ll l$. This assumption also implies that in the ordered phase $k_B T, \Delta \ll \epsilon_F$. The ordering of adatoms is only possible if the binding energy with graphene is smaller than the typical RKKY interaction energy between adatoms ($E_{bind} \lesssim \lambda^2 (n_i a^2)^{3/2} \hbar v / a$).
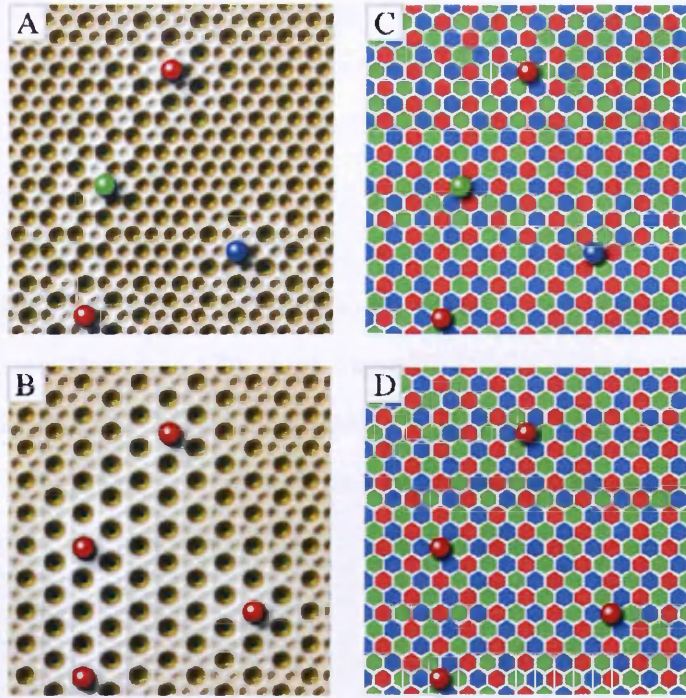
Figure 4.2: Kekulé mosaic ordering of alkali adatoms on the graphene lattice. Panels A and B show the potential landscape that an extra atom would see in the presence of four atoms already shown. In panels C and D the coloring of the atoms in introduced to reveal their position within the Kekulé superlattice. Adapted from [117].

## 4.4 Resistance anomaly in the vicinity of the ordering transition of adatoms

Here we analyze how partial Kekulé ordering of adatoms on graphene affects its resistivity, $\rho$, in the regime of low coverage $n_i a^2 \ll 1$ ($n_i$ is the concentration of adatoms, $a$ is the lattice constant). The behaviour of the temperature dependent resistivity correction $\delta\rho(T) = \rho(T) - \rho(\infty)$ is sketched in Fig. 4.3. At $T \ll T_c$ (region I) the temperature dependence of the resistivity is dominated by a non-vanishing order parameter $\bar{\mathbf{u}}$ causing the amplified intervalley mixing and opening a gap $\Delta \propto \bar{\mathbf{u}} \sim (T_c - T)^\beta$ at the corners of the Brillouin zone. As the temperature increases from $T = 0$ to $T = T_c$ the resistivity correction monotonically decreases as $(T_c - T)^{2\beta}$. At $T > T_c$, critical fluctuations of the order parameter, characterized by the correlation length $\xi \propto |T - T_c|^{-\nu}$, preceding the formation of the ordered

phase lead to a non-monotonic feature in $\delta\rho(T)$. At high temperatures $T \gtrsim T_c$ (region III), the constructive interference of electron waves, scattered by adatoms within ordered clusters of size $\xi$, enhances the resistivity. The effect, which becomes stronger upon approaching $T_c$, is similar to the critical opalescence [134] in materials undergoing structural phase transition or resistivity anomaly in bulk metals with magnetic impurities undergoing a ferromagnetic transition [135]. This enhancement saturates when $\xi$ becomes comparable to the electron wavelength $\lambda_F$, $\lambda_F \approx \xi$. In the region II of temperatures $T \to T_c + 0$, where $\xi \gg \lambda_F$, scattering of electrons is affected only by the gradient of the fluctuating order parameter $\bar{\mathbf{u}}$. The resistivity is thus reduced and a cusp-shape minimum at $T = T_c$ should be expected.
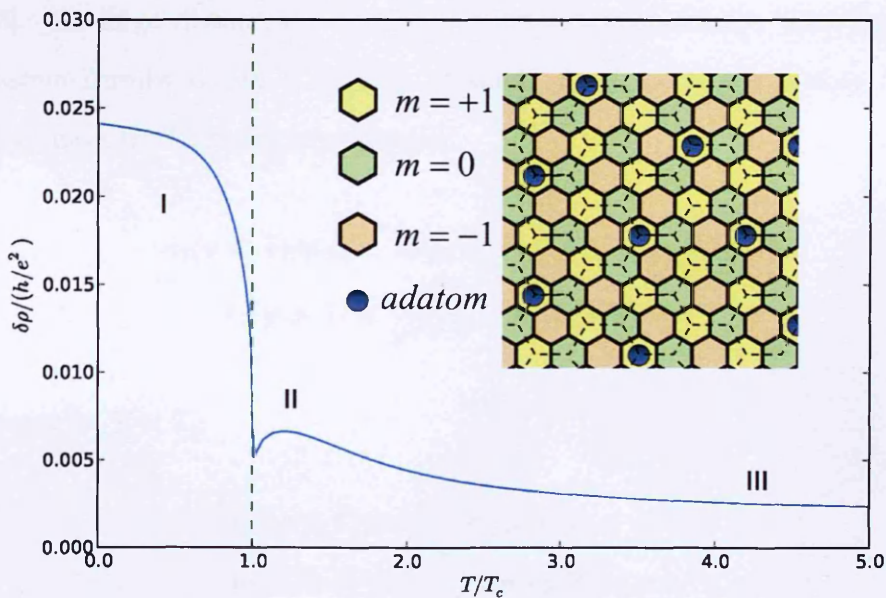


Figure 4.3: The predicted anomaly in the temperature-dependent resistivity of graphene decorated with adatoms in the vicinity of the Kekulé ordering transition. The inset illustrates the Kekulé mosaic ordered state and the assignment of Potts "spin" $m = -1, 0, 1$ to various hexagons in the $\sqrt{3} \times \sqrt{3}$ superlattice.

The effects of adatoms ordering on the electron transport are encoded in the correlation function,

$$\overline{u^\alpha(\mathbf{r})u^\beta(\mathbf{r}')} - \overline{u^\alpha(\mathbf{r})}\,\overline{u^\beta(\mathbf{r}')} = \delta_{\alpha\beta}g(|\mathbf{r} - \mathbf{r}'|), \qquad (4.7)$$

for which the theory of critical phenomena predicts the scaling form [136]

$$g(r) = \frac{\kappa(r/\xi)}{(\sqrt{n_i}r)^{\eta}}, \quad \kappa(y) = \kappa_1(y) + y^{\frac{1-\alpha}{\nu}}\kappa_2(y). \tag{4.8}$$

Here, $\xi \sim n_i^{-1/2}|(T-T_c)/T_c|^{-\nu}$ is the correlation length, and $\alpha$, $\eta$ and $\nu$ are critical exponents, satisfying the relations $2\nu = 2 - \alpha$, $2\beta = \nu\eta$. It has been shown [133] that for the three-state Potts model on a square lattice $\alpha = 1/3$, $\beta = 1/9$, $\nu = 5/6$, $\eta = 4/15$. The small universal corrections to these values due to weak disorder were derived by Dotsenko, *et al.* [137]. However, the value of $\eta$ for random-bond Potts models with a long-range interaction[1] is still unknown [137].

In the critical region $r \ll \xi$, the correlation function behaves essentially as $r^{-\eta}$, with a correction (second term) related to the specific heat anomaly $C \sim |T-T_c|^{-\alpha}$ [133]. At large distances, $r \gg \xi$, $g(r)$ decays exponentially, according to the Ornstein-Zernike theory [136, 138]. Overall, for $T > T_c$ the scaling functions $\kappa_{1,2}(y)$ have the following asymptotics:

$$\kappa_1(y \ll 1) \approx c_1, \quad \kappa_2(y \ll 1) \approx -c_2 \quad (c_1, c_2 \sim 1);$$
$$\kappa_1(y \gg 1) \propto \frac{e^{-y}}{y^{1/2-\eta}}, \quad \kappa_2(y \gg 1) \sim e^{-y}, \tag{4.9}$$

whereas for $T < T_c$,

$$\kappa_1(y \ll 1) \approx c_1, \quad \kappa_2(y \ll 1) \approx c_2;$$
$$\kappa_1(y \gg 1) \propto \frac{e^{-y}}{y^{2-\eta}}, \quad \kappa_2(y \gg 1) \sim e^{-y}. \tag{4.10}$$

At $T < T_c$, the order parameter also acquires a homogeneous average $\bar{u} \propto (T_c - T)^{\beta}$. As long as $\bar{u}$ exceeds the fluctuations of $\mathbf{u}$ (i.e. far enough from $T_c$), the electron states, whose wavelength is larger than the distance between adatoms

---

[1]To mention, 3-state Potts model with $1/r^3$ interaction in 2D without disorder features a first-order phase transition, however, disorder makes it a second order transition [139].

$n_i^{-1/2}$, are described by the effective mean-field Hamiltonian,

$$\overline{\hat{H}} = \hbar v \mathbf{p} \mathbf{\Sigma} + n_i \hbar \lambda v a \Sigma_z (\overline{\mathbf{u}} \Lambda). \qquad (4.11)$$

Accordingly the spectrum $\epsilon_{\mathbf{p}}^2 = (\hbar v p)^2 + \Delta^2$ acquires a gap,

$$\Delta(T) \approx n_i \hbar \lambda v a (1 - T/T_c)^\beta, \qquad (4.12)$$

such that $\Delta(0) \gg T_c$. The plane wave eigenstates of $\overline{\hat{H}}$ are mixed between the two valleys and take the form (for $\epsilon_{\mathbf{p}} > 0$)

$$|\pm 1, \mathbf{p}\rangle = \frac{e^{i\mathbf{p}\mathbf{r}}}{\sqrt{4S}} \begin{pmatrix} \sqrt{\frac{\epsilon_{\mathbf{p}} \pm \Delta}{\epsilon_{\mathbf{p}}}} \\ \sqrt{\frac{\epsilon_{\mathbf{p}} \mp \Delta}{\epsilon_{\mathbf{p}}}} e^{i\varphi_{\mathbf{p}}} \\ \pm \sqrt{\frac{\epsilon_{\mathbf{p}} \pm \Delta}{\epsilon_{\mathbf{p}}}} e^{i\theta} \\ \mp \sqrt{\frac{\epsilon_{\mathbf{p}} \mp \Delta}{\epsilon_{\mathbf{p}}}} e^{i(\varphi_{\mathbf{p}}+\theta)} \end{pmatrix}, \overline{u_x} + i \overline{u_y} = u e^{i\theta}. \qquad (4.13)$$

Intravalley and intervalley scattering determined by $\hat{U}(\mathbf{r})$ and $\hat{V}(\mathbf{r})$ in Eq. (4.4) respectively do not interfere with each other. Hence, the total momentum relaxation rate is the sum of the two electron scattering rates,

$$\tau^{-1} = \tau_0^{-1} + \tau_i^{-1}, \qquad (4.14)$$

where $\tau_0$ and $\tau_i$ stand for intravalley and intervalley momentum relaxation times. For the temperature-dependent Drude resistivity of the graphene sheet (recall that $k_B T, \Delta \ll \epsilon_F$) we thus have

$$\rho(T) = \frac{2}{e^2} \frac{1}{v_F^2 \tau \nu}, \qquad (4.15)$$

where $v_F = \hbar v^2 p_F / \epsilon_F$ is the Fermi velocity, $\nu = 2\epsilon_F/(\pi \hbar^2 v^2)$ is the density of states, and the Fermi energy and momentum are related to the electron density as $p_F = \sqrt{\pi n}$ and $\epsilon_F = \sqrt{\pi \hbar^2 v^2 n + \Delta^2}$.

The temperature dependence $\rho(T)$ at $T \lesssim T_c$ is dominated by the effect of the

order parameter $\bar{\mathbf{u}}$ on the chiral plane wave functions and thus on the scattering rates, in particular $\tau_0^{-1}$. In the Born approximation

$$\frac{1}{\tau_0} = \frac{n_i p_F^2}{\hbar \epsilon_F} \int_0^{2\pi} \frac{d\varphi}{2\pi} \tilde{w}^2 \left( 2p_F \sin \frac{\varphi}{2} \right) (1 - \cos \varphi) r_0(\varphi), \qquad (4.16)$$

$$r_0(\varphi) = \cos^2 \frac{\varphi}{2} + \frac{\Delta^2(T)}{(\hbar v p_F)^2},$$

where $\tilde{w}(k) = \int d\mathbf{r}\, e^{i\mathbf{k}\mathbf{r}} w(r)$ and $\varphi$ is the scattering angle. The form-factor $r_0(\varphi)$ arises from the overlap integral between plane wave states and reflects the absence of backscattering for $\Delta = 0$. Thus, for $T \lesssim T_c$, we find

$$\frac{\delta \rho(T)}{\rho(\infty)} \approx \frac{4\Delta^2(T)}{\pi n \hbar^2 v^2} \frac{\int_0^{2\pi} d\varphi\, \tilde{w}^2 \left( 2p_F \sin \frac{\varphi}{2} \right) \sin^2 \frac{\varphi}{2}}{\int_0^{2\pi} d\varphi\, \tilde{w}^2 \left( 2p_F \sin \frac{\varphi}{2} \right) \sin^2 \varphi}. \qquad (4.17)$$

The temperature dependence $\rho(T)$ at $T > T_c$ is determined by the effect of the ordering of adatoms on the intervalley scattering. Consider the scattering amplitude

$$\langle K' \mathbf{p}' | \hat{V} | K \mathbf{p} \rangle = \frac{\hbar \lambda v a}{2iS} \sin \frac{\varphi_{\mathbf{p}} + \varphi_{\mathbf{p}'}}{2} \sum_l e^{i\theta_l}, \qquad (4.18)$$

$$\theta_l = \frac{2\pi m_l}{3} + (\mathbf{p} - \mathbf{p}') \mathbf{r}_l.$$

At temperatures far from $T_c$, $T \gg T_c$, the positions of adatoms on the super-lattice are random so that $m_l$ takes values $-1, 0$ and $1$ with equal probabilities. As a result, the absolute value of the scattering amplitude can be estimated as $|\langle K' \mathbf{p}' | \hat{V} | K \mathbf{p} \rangle| \sim \sqrt{n_i \lambda_F^2}$. Upon approaching $T_c$ from above, clusters of ordered adatoms with a characteristic size $\xi \gg n_i^{-1/2}$ start appearing. In the sum (4.18) such a cluster generates constructive interference between terms with the same value of $m_l$ provided that $\xi \lesssim \lambda_F$. This increases the scattering amplitude, $|\langle K' \mathbf{p}' | \hat{V} | K \mathbf{p} \rangle| \sim n_i \xi \lambda_F$. A further increase of the correlation length, $\xi > \lambda_F$, has an opposite effect on scattering: electrons get scattered only by the gradients in the smoothly fluctuating field $\bar{\mathbf{u}}$.

91

The intervalley momentum relaxation rate (both at $T < T_c$ and $T > T_c$) $\tau_i^{-1}$ can be expressed in terms of the Fourier transform of the correlation function, $\tilde{g}(k) = \int d\mathbf{r} \, e^{i\mathbf{kr}} g(r)$,

$$\frac{1}{\tau_i} = \frac{\hbar v^2 p_F^2 n_i \lambda^2 a^2}{2\epsilon_F} \int\limits_0^{2\pi} \frac{d\varphi}{2\pi} (1 - \cos\varphi) r_i(\varphi), \tag{4.19}$$

$$r_i(\varphi) = \left[1 + n_i \tilde{g}\left(2p_F \sin\frac{\varphi}{2}\right)\right] \left[2\sin^2\frac{\varphi}{2} + \frac{\Delta^2(T)}{(\hbar v p_F)^2}\right].$$

At $T > T_c$ ($\Delta = 0$) the temperature dependence $\rho(T)$ comes from the correlation function $\tilde{g}(k)$ in Eq. (4.19). Far from the phase transition, $|T - T_c| \sim T_c$, where $\xi < \lambda_F$ (region III in Fig. 4.3), electrons are effectively scattered by small clusters of ordered adatoms. In this region we approximate $\tilde{g}(k) \approx \tilde{g}(0) \propto (\sqrt{n_i}\xi)^{2-\eta}$ and find that

$$\delta\rho(T) \approx C \frac{\Delta^2(0)}{e^2 v^2 \hbar n_i^{\eta/2}} \xi^{2-\eta} \propto \frac{n_i^{2-\eta/2}}{(T - T_c)^{(2-\eta)\nu}}, \tag{4.20}$$

where $C = (3\pi^2/2) \int_0^{+\infty} dy \, y^{1-\eta} \kappa(y)$ is a dimensionless constant.

The above calculation based on the Born approximation is applicable only if the electron energy is larger than the average spectrum gap at the length scale of $\lambda_F$, $\Delta(\lambda_F) < \hbar v p_F$, where

$$\Delta(L) = \hbar n_i \lambda v a \sqrt{\overline{\mathbf{u}(\mathbf{r})\mathbf{u}(\mathbf{r}')}_L} \sim$$
$$\frac{\hbar \sqrt{n_i} \lambda v a}{L} (\sqrt{n_i}\min\{\xi, L\})^{1-\eta}, \tag{4.21}$$

so that $\min\{\xi, \lambda_F\} < \frac{1}{\sqrt{n_i}}\left(\frac{4\pi^2}{n_i \lambda^2 a^2}\right)^{1/(2-\eta)}$, which coincides with the inequality $v p_F \tau_i \gg 1$, that is, if the resistivity of graphene is smaller than $h/e^2$.

## 4.5 The vicinity of the critical point

In the vicinity of the critical point, such that $\lambda_F < \xi$ (region II in Fig. 4.3), electrons experience multiple scatterings within one cluster with a small wave vector transfer, $\sim \xi^{-1}$. This makes $\rho(T)$ sensitive to the critical behaviour of the

correlation function at $r < \xi$. This region is easier to analyze by performing the angular integration in Eq. (4.19) and expressing $\tau_i^{-1}$ in terms of the function $\kappa(y)$ defined in Eq. (4.8):

$$\frac{1}{\tau_i} = \frac{\Delta^2(0)}{\hbar^2 v} \left[ \frac{3p_F}{4n_i} + \frac{2\xi}{(\sqrt{n_i}\xi)^\eta} \int\limits_0^{+\infty} dy \, \frac{\kappa(y)}{y^\eta} f(p_F \xi y) \right]. \qquad (4.22)$$

Here, $f$ can be expressed in terms of Bessel functions as

$$f(x) = \frac{\pi}{x} [x^2 J_0^2(x) - x^2 J_1^2(x) + J_1^2(x) - x J_0(x) J_1(x)]. \qquad (4.23)$$

To evaluate the integral in Eq. (4.22) we divide the integration interval $[0, \infty]$ into two parts, $[0, y_0]$ and $[y_0, \infty]$, where $1 \gg y_0 \gg 1/p_F\xi \to 0$. For the interval $[y_0, \infty]$, we use the fact that $f(p_F\xi y)$ is a fast oscillating function, $f(x \gg 1) \approx 2\sin(2x) + 3\cos(2x)/(2x)$, and that

$$\int\limits_{y_0}^{+\infty} F(y) \sin(Ay) dy = \frac{F(y_0)\cos(Ay_0)}{A} + O\left(\frac{1}{A^2}\right), \qquad (4.24)$$

for $A \gg 1$ and $F(\infty) = 0$. For the interval $[0, y_0]$ in the leading order in $1/p_F\xi$, the result is determined by the values of $\kappa_1(0)$ and $\kappa_2(0)$ in Eq. (4.9). For this, we expand $\kappa_1$ and $\kappa_2$ (which vary at the scale of $y \sim 1$) into Taylor series, evaluate the corresponding integrals in the leading orders in $y_0 \ll 1$, and combine with the contribution from the interval $[y_0, \infty]$. As a result, the term with $\kappa_1$ in Eq. (4.22) produces a finite contribution when $p_F\xi \to \infty$, and we find that

$$\rho(T_c) - \rho(\infty) = \frac{c_1 \pi^{\frac{3}{2}} \Delta^2(0)}{e^2 v^2 \hbar n_i} B(\eta) \left(\frac{n_i}{\pi n}\right)^{1-\eta/2}, \qquad (4.25)$$

where $B(x) = x\Gamma\left(\frac{3+x}{2}\right)\Gamma\left(1 - \frac{x}{2}\right) / \Gamma\left(1 + \frac{x}{2}\right)\Gamma\left(2 + \frac{x}{2}\right)$. If $(1 - \alpha)/\nu < 1$, the next term in the expansion $\kappa_1(y) = \kappa_1(0) + y\kappa_1'(0) + \dots$ generates a contribution $O(1/p_F\xi)$, which, for $T \to T_c$, is less relevant than the more singular $(T - T_c)$-dependent contribution from the $\kappa_2$ term in Eq. (4.22). Following the same steps,

93

we find that the latter term gives rise to the cusp in the $\rho(T)$ dependence in the region II near $T_c$ in Fig. 4.3,

$$\frac{\rho(T) - \rho(T_c)}{\rho(T_c) - \rho(\infty)} = -\frac{c_2 B(\eta - 2\gamma)}{c_1 B(\eta)(\pi n \xi^2)^\gamma} \propto (T - T_c)^{1-\alpha}, \qquad (4.26)$$

where $\gamma = (1 - \alpha)/2\nu$, which is assumed to be $\gamma < 1/2$ for Eq. (4.26) to be applicable. Otherwise (for $\gamma > 1/2$) one should use

$$\frac{\rho(T) - \rho(T_c)}{\rho(T_c) - \rho(\infty)} = -\frac{\kappa_1'(0) B(\eta - 1)}{c_1 B(\eta)(\pi n \xi^2)^{1/2}} \propto (T - T_c)^\nu. \qquad (4.27)$$

The sign of the result Eqs. (4.26, 4.27) is determined by the sign of $c_2$ (or $\kappa_1'(0) < 0$) and by the values of the critical exponents, where $c_2$ depends on the particular form of the correlation function $g(r)$ and is known to be positive for the exact solution of the 2D Ising model on a square lattice [136]. The factor $B(\eta - 2\gamma)/B(\eta)$ has the same sign as $(\eta - 2\gamma)$ and happens to be negative for the three-state Potts model on a square lattice. Notice that Eqs. (4.26, 4.27) are applicable only in a very close vicinity of $T_c$ ($\xi \gg \lambda_F$) and do not influence the overall tendency that resistance dips in the region II.

The behaviour of $\delta\rho(T)$ at $T < T_c$ (region I in Fig. 4.3) is determined by two contributions. One part, $\delta\rho_1/\rho \propto (T_c - T)^{\min\{1-\alpha,\nu\}}$, is related to the specific heat anomaly correction to the correlation function and can be obtained in the same way as Eq. (4.26). The other contribution, $\delta\rho_2/\rho \propto (T_c - T)^{2\beta}$, is due to the formation of a non-zero order parameter in the Kekulé-ordered phase. The second correction dominates when $2\beta < \min\{1 - \alpha, \nu\}$, which is the case for the expected values of the critical exponents. As a result, we attribute the rise of resistivity at $T < T_c$ near the cusp at $T = T_c$ to the formation of a spectral gap in graphene due to the Kekulé mosaic ordering. The qualitative behaviour of the resistivity correction as a function of temperature for all three regimes is plotted in Fig. 4.3 for $\epsilon_F = 0.4 v \sqrt{n_i}$, $n_i \lambda^2 a^2 = 0.005$, where we used the values $c_1 = 0.5$, $c_2 = 0.15$ (calculating the exact values of these coefficients is outside the scope of this work).

94

In conclusion, we investigated electron transport in graphene covered by a dilute ensemble of adatoms residing over the centers of hexagons. We calculated the temperature dependence of the resistivity $\rho(T)$, which appears to be non-monotonic and has a non-analytic cusp at $T = T_c$. Since the form of the cusp depends on the critical indices $\alpha$ and $\beta$ of the phase transition, the experimental observation of such an anomaly may facilitate their measurements.

The form of $\rho(T)$ shown in Fig. 4.3 appears to be generic for partially ordered dilute ensembles of adatoms with alternative positioning on the honeycomb lattice: (i) over the sites [131, 132] and (ii) over carbon-carbon bonds [108]. Since those also fall into the class of Potts models [(i) - 2 value Potts model and (ii) - 3 value Potts model], the anomalies in $\rho(T)$ can be described using Eqs. (4.17,4.26) with appropriate critical indices, $\alpha$ and $\beta$.

# Conclusions

In this thesis we covered a range of problems related to epitaxial graphene and mechanically exfoliated graphene. In chapter 1 we reviewed the fabrication methods of graphene and the electronic structure of monolayer and bilayer graphene. In chapter 2 we investigated the properties of epitaxial graphene grown on Si-terminated surface of SiC, which is successfully used to produce field-effect transistors. In section 2.2 we developed a theoretical model which describes the charge transfer between monolayer graphene and donors in SiC and takes into account the spontaneous polarization of SiC. This model is consistent with the experimental results and explains the high doping of epitaxial graphene, which provides a challenge for its applications in field-effect transistors. Hydrogen intercalation, that can be used to reduce graphene doping, is also described by our model. In section 2.3 we applied the charge transfer model to describe the pinch-off effect in bilayer graphene and the hopping conductivity in this regime. In chapter 3 we studied the quantum Hall effect in epitaxial graphene, which is successfully used in quantum resistance metrology. Using our model we discovered the pinning of $\nu = 2$ QHE plateau over a range of magnetic fields of several Tesla, which is consistent with the high precision of transverse resistance measurements in the system. The effect of bilayer graphene patches on the quality of QHE measurements was studied in section 3.6. Finally, in chapter 4 we investigated the transport properties of exfoliated monolayer graphene covered by adatoms. Certain types of adatoms tend to arrange in ordered patterns due to RKKY interactions, affecting the conductivity of graphene near the phase transition temperature. We calculated the conductivity

of graphene in the presence of such adatoms and linked it to the critical exponents of the transition.

# Bibliography

[1] A. K. Geim, Science **324**, 1530 (2009).

[2] P. R. Wallace, Phys. Rev. **71**, 622 (1947).

[3] K. S. Novoselov, A. K. Geim, S. V. Morozov, D. Jiang, M. I. Katsnelson, I. V. Grigorieva, S. V. Dubonos, A. A. Firsov, Nature **438**, 197 (2005).

[4] M. S. Dresselhaus, G. Dresselhaus, P. Avouris, "Carbon Nanotubes: Synthesis, Structure, Properties, and Applications", Springer (2001).

[5] K. S. Novoselov, Z. Jiang, Y. Zhang, S. V. Morozov, H. L. Stormer, U. Zeitler, J. C. Maan, G. S. Boebinger, P. Kim, A. K. Geim, Science **315**, 1379 (2007).

[6] J. Kedzierski, P. L. Hsu, P. Healey, P. Wyatt, C. Keast, M. Sprinkle, C. Berger, W. A. de Heer, IEEE Trans. Electron. Devices **55**, 2078 (2008).

[7] Y. M. Lin, K. A. Jenkins, A. Valdes-Garcia, J. P. Small, D. B. Farmer, P. Avouris, Nano Letters **9**, 422 (2009).

[8] M. I. Katsnelson, K. S. Novoselov, A. K. Geim, Nature Phys. **2**, 620 (2006).

[9] Y. Wu, Yu-ming Lin, A. A. Bol, K. A. Jenkins, F. Xia, D. B. Farmer, Yu Zhu, P. Avouris, Nature **472**, 74 (2011).

[10] L Liao, Yung-Chen Lin, M. Bao, R. Cheng, J. Bai, Y. Liu, Y. Qu, K. L. Wang, Yu Huang, X. Duan, Nature **467**, 305 (2010).

[11] K. S. Novoselov, A. K. Geim, S. V. Morozov, D. Jiang, Y. Zhang, S. V. Dubonos, I. V. Grigorieva, A. A. Firsov, Science **306**, 666 (2004).

[12] C. Riedl, C. Coletti, U. Starke, J. Phys. D, **43**, 374009 (2010).

[13] A. H. Castro Neto, F. Guinea, N. M. R. Peres, K. S. Novoselov, A. K. Geim, Rev. Mod. Phys. **81**, 109 (2009).

[14] J. W. McClure, Phys. Rev. **104**, 666 (1956).

[15] E. McCann, Phys. Rev. B, **74**, 161403 (2006).

[16] E. McCann, V. I. Fal'ko, Phys. Rev. Lett. **96**, 086805 (2006).

[17] E. McCann, D. S. L. Abergel, V. I. Fal'ko, Solid State Comm. **143**, 110 (2007).

[18] Xu Du, I. Skachko, A. Barker, E. Y. Andrei, Nature Nanotechnology **3**, 491 (2008).

[19] A. Reina, X. Jia, J. Ho, D. Nezich, H. Son, V. Bulovic, M. S. Dresselhaus, J. Kong, Nano Lett. **9**, 30 (2009).

[20] W. Gannett, W. Regan, K. Watanabe, T. Taniguchi, M. F. Crommie, A. Zettl, Appl. Phys. Lett. **98**, 242105 (2011).

[21] T. Ohta, A. Bostwick, T. Seyller, K. Horn, E. Rotenberg, Science **313**, 951 (2006).

[22] A. Bostwick, T. Ohta, T. Seyller, K. Horn, E. Rotenberg, Nat. Phys. **3**, 36 (2007).

[23] T. Ohta, A. Bostwick, J. L. McChesney, T. Seyller, K. Horn, E. Rotenberg, Phys. Rev. Lett. **98**, 206802 (2007).

[24] C. Virojanadara, M. Syvajarvi, R. Yakimova, L. I. Johansson, A. A. Zakharov, T. Balasubramanian, Phys. Rev. B **78**, 245403 (2008).

[25] Gong Gu, Shu Nie, R. M. Feenstra, R. P. Devaty, W. J. Choyke, W. K. Chan, M. G. Kane, Appl. Phys. Lett. **90**, 253507 (2007).

[26] Y. Q. Wu, P. D. Ye, M. A. Capano, Y. Xuan, Y. Sui, M. Qi, J. A. Cooper, T. Shen, D. Pandey, G. Prakash, R. Reifenberger, Appl. Phys. Lett. **92**, 092102 (2008).

[27] K. V. Emtsev, A. Bostwick, K. Horn, J. Jobst, G. L. Kellogg, L. Ley, J. L. McChesney, T. Ohta, S. A. Reshanov, J. Rohrl, E. Rotenberg, A. K. Schmid, D. Waldmann, H. B. Weber, T. Seyller, Nature Mater. **8**, 203 (2009).

[28] A. Tzalenchuk, S. Lara-Avila, A. Kalaboukhov, S. Paolillo, M. Syvajarvi, R. Yakimova, O. Kazakova, T. J. B. M. Janssen, V. Fal'ko, S. Kubatkin, Nature Nanotech. **5**, 186 (2010).

[29] P. N. First, W. A. de Heer, T. Seyller, C. Berger, J. A. Stroscio, J. S. Moon, MRS Bulletin **35**, 296 (2010).

[30] E. V. Castro, K. S. Novoselov, S. V. Morozov, N. M. R. Peres, J. M. B. Lopes dos Santos, J. Nilsson, F. Guinea, A. K. Geim, A. H. Castro Neto, Phys. Rev. Lett. **99**, 216802 (2007).

[31] Y. Zhang, T. T. Tang, C. Girit, Z. Hao, M. C. Martin, A. Zettl, M. F. Crommie, Y. Ron Shen, F. Wang, Nature **459**, 820 (2009).

[32] B. N. Szafranek, D. Schall, M. Otto, D. Neumaier, H. Kurz, Appl. Phys. Lett. **96**, 112103 (2010).

[33] J. B. Oostinga, H. B. Heersche, L. Liu, A. F. Morpurgo, L. M. K. Vandersypen, Nature Mater. **7**, 151 (2007).

[34] W. A. de Heer, C. Berger, X. Wu, P. N. First, E. H. Conrad, X. Li, T. Li, M. Sprinkle, J. Hass, M. L. Sadowski, M. Potemski M, G. Martinez, Solid State Commun. **143**, 92 (2007).

[35] U. Starke, C. Riedl, J. Phys.: CM **21**, 134016 (2009).

[36] C. Riedl, U. Starke, J. Bernhardt, M. Franke, K. Heinz, Phys. Rev. B **76**, 245406 (2007).

[37] C. Riedl, C. Coletti, T. Iwasaki, A. A. Zakharov, U. Starke, Phys. Rev. Lett. **103**, 246804 (2009).

[38] A. van Bommel, J. Crombeen, A. van Tooren, Surface Science **48**, 463 (1975).

[39] F. Varchon, R. Feng, J. Hass, X. Li, B. Ngoc Nguyen, C. Naud, P. Mallet, J. Y. Veuillen, C. Berger, E. H. Conrad, L. Magaud, Phys. Rev. Lett. **99**, 126805 (2007).

[40] A. Mattausch, O. Pankratov, Phys. Rev. Lett. **99**, 076802 (2007).

[41] K.V. Emtsev, F. Speck, Th. Seyller, L. Ley, J.D. Riley, Phys. Rev. B **77**, 155303 (2008).

[42] Y. Qi, S.H. Rhim, G.F. Sun, M. Weinert, L. Li, Phys. Rev. Lett. **105**, 085502 (2010).

[43] J. Jobst, D. Waldmann, F. Speck, R. Hirner, D. K. Maude, Th. Seyller, H. B. Weber, Phys. Rev. B **81**, 195434 (2010).

[44] C. Coletti, C. Riedl, D. S. Lee, B. Krauss, L. Patthey, K. von Klitzing, J. H. Smet, U. Starke, Phys. Rev. B **81**, 235401 (2010).

[45] S. Kopylov, A. Tzalenchuk, S. Kubatkin, V. I. Fal'ko, Appl. Phys. Lett. **97**, 112109 (2010).

[46] S. Lara-Avila, K. Moth-Poulsen, R. Yakimova, Th. Bjornholm, V. I. Fal'ko, A. Tzalenchuk, S. Kubatkin, Adv. Mater. **23**, 878 (2011).

[47] F. Speck, J. Jobst, F. Fromm, M. Ostler, D. Waldmann, M. Hundhausen, H. B. Weber, Th. Seyller, Appl. Phys. Lett. **99**, 122106 (2011).

[48] S. Watcharinyanon, C. Virojanadara, J. R. Osiecki, A. A. Zakharov, R. Yakimova, R. I. G. Uhrberg, L. I. Johansson, Surf. Sci. **605**, 1662 (2011).

[49] Luxmi, N. Srivastava, Guowei He, R. M. Feenstra, P. J. Fisher, Phys. Rev. B **82**, 235406 (2010).

[50] A. Fissel, Physics Reports **379**, 149 (2003).

[51] A. Qteish, V. Heine, R. J. Needs, Phys. Rev. B **45**, 6534 (1992).

[52] V. M. Polyakov, F. Schwierz, J. Appl. Phys. **98**, 023709 (2005).

[53] A. Qteish, V. Heine, R. J. Needs, Phys. Rev. B **45**, 6376 (1992).

[54] A. Qteish, V. Heine, R. J. Needs, Physica B **185**, 366 (1993).

[55] C. H. Park, Byoung-Ho Cheong, Keun-Ho Lee, K. J. Chang, Phys. Rev. B **49**, 4485 (1994).

[56] H. Hibino, H. Kageshima, M. Nagase, J. Phys. D **43**, 374005 (2010).

[57] T. O. Wehling, K. S. Novoselov, S. V. Morozov, E. E. Vdovin, M. I. Katsnelson, A. K. Geim, A. I. Lichtenstein, Nano. Lett. **8**, 173 (2008).

[58] A. Tzalenchuk, S. Lara-Avila, K. Cedergren, M. Syvjrvi, R. Yakimova, O. Kazakova, T.J.B.M. Janssen, K. Moth-Poulsen, Th. Bjrnholm, S. Kopylov, V. I. Fal'ko, S. Kubatkin, Solid State Comm. **151**, 1094 (2011).

[59] F. Schwierz, Nat. Nanotechnol. **5**, 487 (2010).

[60] J. S. Moon, D. Curtis, S. Bui, M. Hu, D. K. Gaskill, J. L. Tedesco, P. Asbeck, G. G. Jernigan, B. L. VanMil, R. L. Myers-Ward, C. R. Eddy, P. M. Campbell, X. Weng, IEEE Electron Device Lett. **31**, 260 (2010).

[61] S. Sonde, F. Giannazzo, V. Raineri, R. Yakimova, J. R. Huntzinger, A. Tiberj, J. Camassel, Phys. Rev. B **80**, 241406 (2009).

[62] L. Patrick, W. J. Choyke, Phys. Rev. B **6**, 2255 (1970).

[63] S. Weingart, C. Bock, U. Kunze, F. Speck, Th. Seyller, L. Ley, Appl. Phys. Lett. **95**, 262101 (2009).

[64] T. J. B. M. Janssen, A. Tzalenchuk, R. Yakimova, S. Kubatkin, S. Lara-Avila, S. Kopylov, V. I. Fal'ko, Phys. Rev. B **83**, 233402 (2010).

[65] J. Xia, F. Chen, J. Li, N. Tao, Nature Nanotechnology **4**, 505 (2009).

[66] T. Fang, A. Konar, H. Xing, D. Jena, Appl. Phys. Lett. **91**, 092109 (2007).

[67] S. Droscher, P. Roulleau, F. Molitor, P. Studerus, C. Stampfer, K. Ensslin, T. Ihn, Appl. Phys. Lett. **96**, 152104 (2010).

[68] J. Guo, Y. Yoon, Y. Ouyang, Nano Lett. **7**, 1935 (2007).

[69] T. Taychatanapat, P. Jarillo-Herrero, Phys. Rev. Lett. **105**, 166601 (2010).

[70] H. Miyazaki, K. Tsukagoshi, A. Kanda, M. Otani, S. Okada, Nano Lett. **10**, 3888 (2010).

[71] J. Nilsson, A. H. Castro Neto, Phys. Rev. Lett. **98**, 126801 (2007).

[72] E. Rossi, S. Das Sarma, Phys. Rev. Lett. **107**, 155502 (2011).

[73] S. Tanabe, Y. Sekine, H. Kageshima, M. Nagase, H. Hibino, Jpn. J. Appl. Phys. **50**, 04DN04 (2011).

[74] N. F. Mott, J. Non-Crystal. Solids **1**, 1 (1968).

[75] A. L. Efros, B. I. Shklovskii, J. Phys. C **8**, L49 (1975).

[76] B. I. Shklovskii, A. L. Efros, "Electronic properties of dopes semiconductors", Springer-Verlag (1984).

[77] B. Movaghar, W. Schirmacher, J. Phys. C **14**, 859 (1981).

[78] S. D. Baranovskii, A. L. Efros, B. L. Gelmont, B. I. Shklovskii, J. Phys. C: Solid State Phys., **12**, 1023 (1979).

[79] K. v. Klitzing, G. Dorda, M. Pepper, Phys. Rev. Lett. **45**, 494 (1980).

[80] Y. Zhang, Y. Tan, H .L. Stormer, P. Kim, Nature **438**, 201 (2005).

[81] T. Shen, J. J. Gu, M. Xu, Y. Q. Wu, M. L. Bolen, M. A. Capano, L. W. Engel, P. D. Ye, Appl. Phys. Lett. **95**, 172105 (2009).

[82] S. Tanabe, Y. Sekine, H. Kageshima, M. Nagase, H. Hibino, Appl. Phys. Express **3**, 075102 (2010).

[83] X. S. Wu, Y. K. Hu, M. Ruan, N. K. Madiomanana, J. Hankinson, M. Sprinkle, C. Berger, W. A. de Heer, Appl. Phys. Lett. **95**, 223108 (2009).

[84] K. S. Novoselov, E. McCann, S. V. Morozov, V. I. Fal'ko, M. I. Katsnelson, U. Zeitler, D. Jiang, F. Schedin, A. K. Geim, Nature Physics **2**, 177 (2006).

[85] W. Poirier, F. Schopfer, Eur. Phys. J. Spec. Top **172**, 207 (2009).

[86] I. M. Mills, P. J. Mohr, T. J. Quinn, B. N. Taylor, E. R. Williams, Metrologia **43**, 227 (2006).

[87] B. Jeckelmann, B. Jeanneret, Rep. Prog. Phys. **64**, 1603 (2001).

[88] M. Mucha-Kruczynski, E. McCann, V. I. Fal'ko, Solid State Comm. **149**, 1111 (2009).

[89] K. Bennaceur, P. Jacques, F. Portier, P. Roche, D. C. Glattli, Phys. Rev. B **86**, 085433 (2012).

[90] A.J.M. Giesbers, G. Rietveld, E. Houtzager, U. Zeitler, R. Yang, K. S. Novoselov, A. K. Geim, J. C. Maan, Appl. Phys. Lett. **93**, 222109 (2008).

[91] C. Berger, Z. M. Song, T. B. Li, X. B. Li, A. Y. Ogbazghi, R. Feng, Z. T. Dai, A. N. Marchenkov, E. H. Conrad, P. N. First, W. A. de Heer, J. Phys. Chem. B **108**, 19912 (2004).

[92] P. Darancet, N. Wipf, C. Berger, W. A. de Heer, D. Mayou, Phys. Rev. Lett. **101**, 116806 (2008).

[93] S. Luryi, Appl. Phys. Lett. **52**, 501 (1988).

[94] J. P. Eisenstein, L. N. Pfeiffer, K. W. West, Phys. Rev. B **50**, 1760 (1994).

[95] D. L. John, L. C. Castro, D. L. Pulfrey, J. Appl. Phys. **96**, 5180 (2004).

[96] L. A. Ponomarenko, R. Yang, R. V. Gorbachev, P. Blake, A. S. Mayorov, K. S. Novoselov, M. I. Katsnelson, A. K. Geim, Phys. Rev. Lett. **105**, 136801 (2010).

[97] Y. J. Song, A. F. Otte, Y. Kuk, Y. Hu, D. B. Torrance, P. N. First, W. A. de Heer, H. Min, S. Adam, M. D. Stiles, A. H. MacDonald, J. A. Stroscio, Nature **467**, 185 (2010).

[98] M. Furlan, Phys. Rev. B **57**, 14818 (1998).

[99] A. J. M. Giesbers, U. Zeitler, L. A. Ponomarenko, R. Yang, K. S. Novoselov, A. K. Geim, J. C. Maan, Phys. Rev. B **80**, 241411 (R) (2009).

[100] Y. Zheng, T. Ando, Phys. Rev. B **65**, 245420 (2002).

[101] C. Virojanadara, R. Yakimova, J. R. Osiecki, M. Syvajarvi, R.I.G. Uhrberg, L.I. Johansson, A.A. Zakharov, Surf. Sci. **603**, L87 (2009).

[102] M. K. Yakes, D. Gunlycke, J. L. Tedesco, P. M. Campbell, R. L. Myers-Ward, C. R. Eddy, D. K. Gaskill, P. E. Sheehan, A. R. Laracuente, Nano Lett. **10**, 1559 (2010).

[103] T. Schumann, K.-J. Friedland, M. H. Oliveira Jr., A. Tahraoui, J. M. J. Lopes, H. Riechert, Phys. Rev. B **85**, 235402 (2012).

[104] B. Ozyilmaz, P. Jarillo-Herrero, D. Efetov, D. A. Abanin, L. S. Levitov, P. Kim, Phys. Rev. Lett. **99**, 166804 (2007).

[105] S. Kopylov, V. Cheianov, B. L. Altshuler, V. I. Fal'ko, Phys. Rev. B **83**, 201401 (2011).

[106] A. Fasolino, J. H. Los, M. I. Katsnelson, Nature Mat. **6**, 858 (2007).

[107] A. Cortijo, M. A. H. Vozmediano, Nucl. Phys. B **763**, 293 (2007).

[108] V. V. Cheianov, O. Syljuasen, B. L. Altshuler, V. Fal'ko, Phys. Rev. B **80**, 233409 (2009).

[109] K. Nomura, A. H. MacDonald, Phys. Rev. Lett. **96**, 256602 (2006).

[110] V. M. Pereira, F. Guinea, J. M. B. Lopes dos Santos, N. M. R. Peres, A. H. Castro Neto, Phys. Rev. Lett. **96**, 036801 (2006).

[111] M. Evaldsson, I. V. Zozoulenko, Hengyi Xu, T. Heinzel, Phys. Rev. B **78**, 161407 (2008).

[112] D. Lamoen, B. N. J. Persson, J. Chem. Phys. **108**, 3332, (1998).

[113] K. Nordlund, J. Keinonen, T. Mattila, Phys. Rev. Lett. **77**, 699 (1996).

[114] L. Jeloaica, V. Sidis, Chem. Phys. Lett. **300**, 157 (1999).

[115] E. McCann, K. Kechedzhi, V. I. Fal'ko, H. Suzuura, T. Ando, B. L. Altshuler, Phys. Rev. Lett. **97**, 146805 (2006).

[116] K. Kechedzhi, E. McCann, V. I. Fal'ko, H. Suzuura, T. Ando, B. L. Altshuler, Eur. Phys. J. Special Topics **148**, 39 (2007).

[117] V. V. Cheianov, V. I. Fal'ko, O. Syljuasen, B. L. Altshuler, Solid State Comm. **149**, 1499 (2009).

[118] V. V. Cheianov, V. I. Fal'ko, Phys. Rev. Lett. **97**, 226801 (2006).

[119] N. H. Shon, T. Ando, J. Phys. Soc. Jpn. **67**, 2421 (1998).

[120] S. Das Sarma, S. Adam, E. H. Hwang, E. Rossi, Rev. Mod. Phys. **83**, 407 (2011).

[121] I. Aleiner, K. Efetov, Phys. Rev. Lett. **97**, 236801 (2006).

[122] A. Altland, Phys. Rev. Lett. **97**, 236802 (2006).

[123] N. M. R. Peres, F. Guinea, A. H. Castro Neto, Phys. Rev. B **73**, 125411 (2006).

[124] J. Tworzydlo, B. Trauzettel, M. Titov, A. Rycerz, C. W. J. Beenakker, Phys. Rev. Lett. **96**, 246802 (2006).

[125] J. Martin, N. Akerman, G. Ulbricht, T. Lohmann, J. H. Smet, K. von Klitzing, A. Yacobi, Nature Phys. **4**, 144 (2008).

[126] S. Adam, E. H. Hwang, V. M. Galitski, S. Das Sarma, Proc. Natl. Acad. Sci. U.S.A. **104**, 18 392 (2007).

[127] J. Friedel, Phil. Mag. **43**, 153 (1952).

[128] C. Bena, Phys. Rev. Lett. **100**, 076601 (2008).

[129] A. Bacsi, A. Virosztek, Phys. Rev. B **82**, 193405 (2010).

[130] N. M. R. Peres, L. Yang, S. W. Tsai, New J. Phys. **11**, 095007 (2009).

[131] V. V. Cheianov, O. Syljuasen, B. L. Altshuler, V. I. Fal'ko, Europhys. Lett. **89**, 56003 (2010).

[132] D. A. Abanin, A. V. Shytov, L. S. Levitov, Phys. Rev. Lett. **105**, 086802 (2010).

[133] R. J. Baxter "Exactly solved models in statistical mechanics", Academic Press (1982).

[134] V. L. Ginzburg, A. P. Levanyuk, J. Phys. Chem. Solids **6**, 51 (1958), Soviet Phys. JETP **12**, 138 (1961).

[135] M. E. Fisher, J. S. Langer, Phys. Rev. Lett. **20**, 665 (1968).

[136] M. E. Fisher, Rep. Prog. Phys. **30**, 615 (1967).

[137] Vl. Dotsenko, M. Picco, P. Pujol, Nucl. Phys. B **455** [FS], 701 (1995).

[138] L. D. Landau, E. M. Lifshitz, Statistical Physics I, Butterworth-Heinemann (1980).

[139] M. Aizenman, J. Wehr, Phys. Rev. Lett. **62**, 2503 (1989).